



University of Basilicata

Doctoral research (PhD) programme in
ENGINEERING FOR INNOVATION AND SUSTAINABLE DEVELOPMENT

A DEEP LEARNING APPROACH FOR MONITORING SEVERE RAINFALL IN URBAN CATCHMENTS USING CONSUMER CAMERAS.

MODELS DEVELOPMENT AND DEPLOYMENT ON A CASE STUDY IN MATERA (ITALY)

Industry 4.0 - Enhancing flood risk management, through near real-time
methods and technologies, for risk communication at local scale

Academic Discipline
ICAR/02

PhD Coordinator
Prof. Carmine Serio

Candidate
Eng. Ar. Nicla Maria Notarangelo

Supervisor
Prof. Aurelia Sole

Co-Supervisors
Dr. Kohin Hirano
Dr. Raffaele Albano
Mr. Vincenzo Lioy

XXXIII Cycle



University of Basilicata

Doctoral research (PhD) programme in
ENGINEERING FOR INNOVATION AND SUSTAINABLE DEVELOPMENT

**A DEEP LEARNING APPROACH FOR MONITORING
SEVERE RAINFALL IN URBAN CATCHMENTS
USING CONSUMER CAMERAS.**
MODELS DEVELOPMENT AND DEPLOYMENT ON A CASE STUDY IN MATERA (ITALY)

Industry 4.0 - Enhancing flood risk management, through near real-time methods and technologies, for risk communication at local scale

Academic Discipline
ICAR/02

PhD Coordinator

Prof. Carmine Serio

Handwritten signature of Prof. Carmine Serio in blue ink.

Supervisor

Prof. Aurelia Sole

Handwritten signature of Prof. Aurelia Sole in black ink.

Candidate

Eng. Ar. Nicla Maria Notarangelo

Handwritten signature of Eng. Ar. Nicla Maria Notarangelo in black ink.

Co-Supervisors

Dr. Kohin Hirano

Handwritten signature of Dr. Kohin Hirano in black ink.

Dr. Raffaele Albano

Handwritten signature of Dr. Raffaele Albano in black ink.

Mr. Vincenzo Liroy

Handwritten signature of Mr. Vincenzo Liroy in black ink.

XXXIII Cycle

*There is something to be learned from a rainstorm.
When meeting with a sudden shower, you try not
to get wet and run quickly along the road. But
doing such things as passing under the eaves of
houses, you still get wet. When you are resolved
from the beginning, you will not be perplexed,
though you still get the same soaking.
This understanding extends to all things.
— Yamamoto Tsunetomo, Hagakure*

「一、大雨の箴と云ふ事あり。途中にて俄雨にあひて、濡れじとて道を急ぎ
走り、軒下などを通りても、濡るゝ事は替らざる也。初めより思ひはまりて
濡るゝ時、心に苦しみなく濡るゝ事は同じ。これ萬づにわたる心得也。」
— 山本常朝

To those who have been here and those who are gone.

ABSTRACT

In the last 50 years, flooding has figured as the most frequent and widespread natural disaster globally. Extreme precipitation events stemming from climate change could alter the hydro-geological regime resulting in increased flood risk. Near real-time precipitation monitoring at local scale is essential for flood risk mitigation in urban and suburban areas, due to their high vulnerability. Presently, most of the rainfall data is obtained from ground-based measurements or remote sensing that provide limited information in terms of temporal or spatial resolution. Other problems may be due to the high costs. Furthermore, rain gauges are unevenly spread and usually placed away from urban centers. In this context, a big potential is represented by the use of innovative techniques to develop low-cost monitoring systems. Despite the diversity of purposes, methods and epistemological fields, the literature on the visual effects of the rain supports the idea of camera-based rain sensors but tends to be device-specific. The present thesis aims to investigate the use of easily available photographing devices as rain detectors-gauges to develop a dense network of low-cost rainfall sensors to support the traditional methods with an expeditious solution embeddable into smart devices. As opposed to existing works, the study focuses on maximizing the number of image sources (like smartphones, general-purpose surveillance cameras, dashboard cameras, webcams, digital cameras, etc.). This encompasses cases where it is not possible to adjust the camera parameters or obtain shots in timelines or videos. Using a Deep Learning approach, the rainfall characterization can be achieved through the analysis of the perceptual aspects that determine whether and how a photograph represents a rainy condition. The first scenario of interest for the supervised learning was a binary classification; the binary output (presence or absence of rain) allows the detection of the presence of precipitation: the cameras act as rain detectors. Similarly, the second scenario of interest was a multi-class classification; the multi-class output described a range of quasi-instantaneous rainfall intensity: the cameras act as rain estimators. Using Transfer Learning with Convolutional Neural Networks, the developed models were compiled, trained, validated, and tested. The preparation of the classifiers included the preparation of a suitable dataset encompassing unconstrained verisimilar settings: open data, several data owned by National Research Institute for Earth Science and Disaster Prevention - NIED (dashboard cameras in Japan coupled with high precision multi-parameter radar data), and experimental activities conducted in the NIED Large Scale Rainfall Simulator. The outcomes were applied to a real-world scenario, with the experimentation through a pre-existent

surveillance camera using 5G connectivity provided by Telecom Italia S.p.A. in the city of Matera (Italy). Analysis unfolded on several levels providing an overview of generic issues relating to the urban flood risk paradigm and specific territorial questions inherent with the case study. These include the context aspects, the important role of rainfall from driving the millennial urban evolution to determining present criticality, and components of a Web prototype for flood risk communication at local scale. The results and the model deployment raise the possibility that low-cost technologies and local capacities can help to retrieve rainfall information for flood early warning systems based on the identification of a significant meteorological state. The binary model reached accuracy and F1 score values of 85.28% and 0.86 for the test, and 83.35% and 0.82 for the deployment. The multi-class model reached test average accuracy and macro-averaged F1 score values of 77.71% and 0.73 for the 6-way classifier, and 78.05% and 0.81 for the 5-class. The best performances were obtained in heavy rainfall and no-rain conditions, whereas the mispredictions are related to less severe precipitation. The proposed method has limited operational requirements, can be easily and quickly implemented in real use cases, exploiting pre-existent devices with a parsimonious use of economic and computational resources. The classification can be performed on single photographs taken in disparate conditions by commonly used acquisition devices, i.e. by static or moving cameras without adjusted parameters. This approach is especially useful in urban areas where measurement methods such as rain gauges encounter installation difficulties or operational limitations or in contexts where there is no availability of remote sensing data. The system does not suit scenes that are also misleading for human visual perception. The approximations inherent in the output are acknowledged. Additional data may be gathered to address gaps that are apparent and improve the accuracy of the precipitation intensity prediction. Future research might explore the integration with further experiments and crowdsourced data, to promote communication, participation, and dialogue among stakeholders and to increase public awareness, emergency response, and civic engagement through the smart community idea.

Negli ultimi 50 anni, le alluvioni si sono confermate come il disastro naturale più frequente e diffuso a livello globale. Tra gli impatti degli eventi meteorologici estremi, conseguenti ai cambiamenti climatici, rientrano le alterazioni del regime idrogeologico con conseguente incremento del rischio alluvionale. Il monitoraggio delle precipitazioni in tempo quasi reale su scala locale è essenziale per la mitigazione del rischio di alluvione in ambito urbano e periurbano, aree connotate da un'elevata vulnerabilità. Attualmente, la maggior parte dei dati sulle precipitazioni è ottenuta da misurazioni a terra o telerilevamento che forniscono informazioni limitate in termini di risoluzione temporale o spaziale. Ulteriori problemi possono derivare dagli elevati costi. Inoltre i pluviometri sono distribuiti in modo non uniforme e spesso posizionati piuttosto lontano dai centri urbani, comportando criticità e discontinuità nel monitoraggio. In questo contesto, un grande potenziale è rappresentato dall'utilizzo di tecniche innovative per sviluppare sistemi inediti di monitoraggio a basso costo. Nonostante la diversità di scopi, metodi e campi epistemologici, la letteratura sugli effetti visivi della pioggia supporta l'idea di sensori di pioggia basati su telecamera, ma tende ad essere specifica per dispositivo scelto. La presente tesi punta a indagare l'uso di dispositivi fotografici facilmente reperibili come rilevatori-misuratori di pioggia, per sviluppare una fitta rete di sensori a basso costo a supporto dei metodi tradizionali con una soluzione rapida incorporabile in dispositivi intelligenti. A differenza dei lavori esistenti, lo studio si concentra sulla massimizzazione del numero di fonti di immagini (smartphone, telecamere di sorveglianza generiche, telecamere da cruscotto, webcam, telecamere digitali, ecc.). Ciò comprende casi in cui non sia possibile regolare i parametri fotografici o ottenere scatti in timeline o video. Utilizzando un approccio di Deep Learning, la caratterizzazione delle precipitazioni può essere ottenuta attraverso l'analisi degli aspetti percettivi che determinano se e come una fotografia rappresenti una condizione di pioggia. Il primo scenario di interesse per l'apprendimento supervisionato è una classificazione binaria; l'output binario (presenza o assenza di pioggia) consente la rilevazione della presenza di precipitazione: gli apparecchi fotografici fungono da rivela-

tori di pioggia. Analogamente, il secondo scenario di interesse è una classificazione multi-classe; l'output multi-classe descrive un intervallo di intensità delle precipitazioni quasi istantanee: le fotocamere fungono da misuratori di pioggia. Utilizzando tecniche di Transfer Learning con reti neurali convoluzionali, i modelli sviluppati sono stati compilati, addestrati, convalidati e testati. La preparazione dei classificatori ha incluso la preparazione di un set di dati adeguato con impostazioni verosimili e non vincolate: dati aperti, diversi dati di proprietà del National Research Institute for Earth Science and Disaster Prevention - NIED (telecamere dashboard in Giappone accoppiate con dati radar multi-parametrici ad alta precisione) e attività sperimentali condotte nel simulatore di pioggia su larga scala del NIED. I risultati sono stati applicati a uno scenario reale, con la sperimentazione attraverso una telecamera di sorveglianza preesistente che utilizza la connettività 5G fornita da Telecom Italia S.p.A. nella città di Matera (Italia). L'analisi si è svolta su più livelli, fornendo una panoramica sulle questioni relative al paradigma del rischio di alluvione in ambito urbano e questioni territoriali specifiche inerenti al caso di studio. Queste ultime includono diversi aspetti del contesto, l'importante ruolo delle piogge dal guidare l'evoluzione millenaria della morfologia urbana alla determinazione delle criticità attuali, oltre ad alcune componenti di un prototipo Web per la comunicazione del rischio alluvionale su scala locale. I risultati ottenuti e l'implementazione del modello corroborano la possibilità che le tecnologie a basso costo e le capacità locali possano aiutare a caratterizzare la forzante pluviometrica a supporto dei sistemi di allerta precoce basati sull'identificazione di uno stato meteorologico significativo. Il modello binario ha raggiunto un'accuratezza e un F1-score di 85,28% e 0,86 per il set di test e di 83,35% e 0,82 per l'implementazione nel caso di studio. Il modello multi-classe ha raggiunto un'accuratezza media e F1-score medio (*macro-average*) di 77,71% e 0,73 per il classificatore a 6 vie e 78,05% e 0,81 per quello a 5 classi. Le prestazioni migliori sono state ottenute nelle classi relative a forti precipitazioni e assenza di pioggia, mentre le previsioni errate sono legate a precipitazioni meno estreme. Il metodo proposto richiede requisiti operativi limitati, può essere implementato facilmente e rapidamente in casi d'uso reali, sfruttando dispositivi preesistenti con un uso parsimonioso di risorse economiche e computazionali. La classificazione può essere eseguita su singole fotografie scattate in condizioni disparate da dispositivi di acquisizione di uso comune, ovvero da telecamere statiche o in

movimento senza regolazione dei parametri. Questo approccio potrebbe essere particolarmente utile nelle aree urbane in cui i metodi di misurazione come i pluviometri incontrano difficoltà di installazione o limitazioni operative o in contesti in cui non sono disponibili dati di telerilevamento o radar. Il sistema non si adatta a scene che sono fuorvianti anche per la percezione visiva umana. I limiti attuali risiedono nelle approssimazioni intrinseche negli output. Per colmare le lacune evidenti e migliorare l'accuratezza della previsione dell'intensità di precipitazione, sarebbe possibile un'ulteriore raccolta di dati. Sviluppi futuri potrebbero riguardare l'integrazione con ulteriori esperimenti in campo e dati da *crowdsourcing*, per promuovere comunicazione, partecipazione e dialogo aumentando la resilienza attraverso consapevolezza pubblica e impegno civico in una concezione di comunità *smart*.

PUBLICATIONS

Some ideas and figures have appeared previously in the following works:

Notarangelo, Nicla M., Kohin Hirano, Aurelia Sole, and Raffaele Albano (June 2019a). "Enhancing flood risk management, through near real-time methods and technologies, for risk communication at local scale." NIED (National Research Institute for Earth Science and Disaster Resilience). Tuskuba, Japan.

Notarangelo, Nicla M., Kohin Hirano, Aurelia Sole, and Raffaele Albano (May 2019b). "Rainfall detection in single images with Convolutional Neural Networks." 6th Weather Disaster Mitigation Innovation Forum "Disaster Prevention × AI" -Toward Meteorological Disaster Mitigation with AI. Innovation Center for Meteorological Disaster Mitigation. Tokyo, Japan.

Notarangelo, Nicla M., Kohin Hirano, Aurelia Sole, and Raffaele Albano (2020). "Rilevamento delle precipitazioni piovose in immagini singole con reti neurali convoluzionali- Rainfall detection in single images through Convolutional Neural Networks." In: *Italian Conference on Integrated River Basin Management (ICIRBM-Guardia 2020)*. Vol. 41. Cosenza, Italy: EdiBios, pp. 69–82. ISBN: 978-88-97181-75-0.

Notarangelo, Nicla Maria, Kohin Hirano, Raffaele Albano, and Aurelia Sole (Feb. 2021). *Transfer Learning with Convolutional Neural Networks for Rainfall Detection in Single Images*. Vol. 13. 5. Publication Title: Water. MDPI AG. DOI: 10.3390/w13050588.

ACKNOWLEDGMENTS

This research was supported by Regione Basilicata, within the Engineering School of University of Basilicata PhD Program “Engineering For Innovation And Sustainable Development” (*Convenzione Dottorati Innovativi con specializzazione in tecnologie abilitanti in Industria 4.0*) - Industry 4.0, topic: *Enhancing flood risk management, through near real-time methods and technologies, for risk communication at local scale.*

First of all, I wish to express my sincere appreciation to my supervisor, Prof. Aurelia Sole for being an empowering woman, taking me into her fold and inspiring my interest in this challenging field.

I’m deeply indebted to Dr. Hirano Kohin from National Research Institute for Earth Science and Disaster Resilience (NIED), who guided and encouraged me even when the road got tough. Without her careful assistance and profound competence, this thesis would not have been realized.

Ingenious suggestions and clever comments given by Dr. Raffaele Albano were essential in formulating the research questions through each stage of the process.

I also had the great pleasure of working with Mr. Vincenzo Lioy of TIM S.p.A., who took keen interest on the research and supported me in a timely and professional way.

The assistance provided by the staff of the NIED, the Storm, Flood and Landslide Research Division, and the Large-scale Rainfall Simulator with the data sets and the experiments was greatly appreciated. Special thanks to Dr. Danjo Toru for sharing time and expertise about the Simulator. I’d like to extend my acknowledgment to Dr. Shakti P. C., Dr. Maesaka Takeshi, Dr. Shusse Yukari, Dr. Kato Ryohei, Nakajima Hiroko, MSc, and all the others for the advice offered, the friendship made, and the good times spent in Japan.

Many thanks to *my labmates*, the LabGis team at UniBas: Dr. Andrea Cantisani, Dr. Antonio Perrone, Vincenzo Scuccimarra, MSc, and -last but not least- Eng. Leonardo Mancusi from Ricerca sul Sistema Energetico who provided invaluable insight, knowledge, and affection. Thanks also to Prof. Ruggero Ermini and Prof. Salvatore Manfreda, your sagacious discussions pushed me to sharpen my thinking.

Special thanks to the staff of the TIM for providing access to data and scientific-technical expertise in digital innovation, in particular thanks to Eng. Clelia Ghibauda, Eng. Umberto Trincherò, and Eng. Andrea Bragagnini.

I owe my deepest gratitude to Prof. Ina Macaione and the late Prof. Armando Sichenze who have always been my guides, friends, and philosophers. Your belief in me has made this journey possible.

Thanks to Prof. Chiara Rizzi for the truthful and heartening conversations.

All the work would not have been possible without the great love and support of my family, my sister, Incoronata; my mother, Rosa; and my father, Michele. I wish also to show my gratitude to Vito, Mariangela, and Giuseppe for sharing with me useful suggestions about legislation and computer science, warm encouragement, and crazy kickboxing training sessions during the Covid-19 lockdown.

CONTENTS

0	INTRODUCTION	1
I	THEORETICAL FRAMEWORK	
I	URBAN FLOOD RISK MANAGEMENT AND COMMUNICATION	9
1.1	The risk paradigm	9
1.2	Legal framework	16
1.3	People-centered Early Warning Systems and risk communication at local scale	17
II	RAINFALL ESTIMATION THROUGH DEEP LEARNING	
2	BACKGROUND AND AIM	25
2.1	Rainfall and Computer Vision: State of Art	25
2.1.1	Rain removal techniques	26
2.1.2	Rain measurement techniques	28
2.1.3	Weather classification techniques	29
3	METHODOLOGY DESIGN	33
3.1	Deep Learning for Computer Vision: Convolutional Neural Networks	35
4	BINARY CLASSIFICATION	41
4.1	Dataset creation	41
4.1.1	Model architecture setup	46
4.2	Results and discussion	50
4.2.1	Training and validation	50
4.2.2	Testing and evaluation	52
5	MULTI-CLASS CLASSIFICATION	59
5.1	Rainfall intensity ranges	60
5.2	Data sources	64
5.3	Model architecture setup	70
5.3.1	Training and validation setup	73
5.4	6 Class Classification	75
5.4.1	Results and discussion	77
5.5	5 Class Classification	84
5.5.1	Results and discussion	86
III	MATERA CASE STUDY	
6	MATERA CASE STUDY	95
6.1	Diachronic evolution of the urban morphology	97
6.2	Statistics	112
6.3	Critical Points - Past Flood Events	121

6.4	Matera thermo-pluviometric data	129
6.5	Bari - Matera 5G project	131
6.6	Real-World Deployment of the Binary Model . . .	132
6.7	MATEERA: A web prototyping tool for flood risk communication at local scale	139
7	CONCLUSIONS AND FUTURE WORK	143
IV APPENDIX		
A	DIACHRONIC LEGAL FRAMEWORK	149
B	THE NIED LARGE-SCALE RAINFALL SIMULATOR	155
C	LANDSLIDES AND FLOODS: LIFE SAVING TIPS - RULES FOR SELF- PROTECTION IN THE EVENT OF AN ALARM	159

LIST OF FIGURES

Figure 1.1	Determinants of risk	9
Figure 1.2	Share of occurrence of natural disasters . .	11
Figure 1.3	Global reported natural disasters	12
Figure 1.4	Urbanization and the hydrological cycle .	14
Figure 1.5	Urban Flood Scenario	15
Figure 1.6	Risk management model	19
Figure 1.7	Extended risk assessment framework . . .	20
Figure 1.8	Representational - behavioral framework	21
Figure 3.1	Artificial Intelligence, Machine Learning, Deep Learning	33
Figure 3.2	AI System parts	34
Figure 4.1	Image2Weather examples	42
Figure 4.2	Geolocation of the dash-cam pictures . . .	43
Figure 4.3	NIED Large-scale Rainfall Simulator . . .	44
Figure 4.4	Rainfall simulator experiment examples .	44
Figure 4.5	Data Augmentation	46
Figure 4.6	Feature extraction with Convolutional Base	47
Figure 4.7	Training and Validation	51
Figure 5.1	Informative rainfall chart - JMA	63
Figure 5.2	Dash-cam geolocation - Tokyo Metropoli- tan Area	65
Figure 5.3	Dash-cam geolocation - Japan	66
Figure 5.4	Rainfall simulator experiments	67
Figure 5.5	Rain gauges	68
Figure 5.6	Data Augmentation	70
Figure 5.7	VGG16 model architecture	71
Figure 5.8	Training and Validation - 6 Class model .	78
Figure 5.9	Training and Validation - 5 Class model .	87
Figure 6.1	Area of interest	95
Figure 6.2	Sassi view	96
Figure 6.3	Sassi view	96
Figure 6.4	The Sassi hydromorphology	97
Figure 6.5	Cistern transformation	98
Figure 6.6	<i>Jazzo</i> and <i>vicinato</i>	99
Figure 6.7	The Sassi urban ecosystem	99
Figure 6.8	Sassi view	100
Figure 6.9	Contemporary urban morphology	101
Figure 6.10	Henri Cartier-Bresson: Matera	102

Figure 6.11	New districts of <i>Risanamento</i>	103
Figure 6.12	Old and new urban fabric view	104
Figure 6.13	Matera: Tales of a City	105
Figure 6.14	Istat Census sections	112
Figure 6.15	Municipal Structural Plan: Macro-areas . .	112
Figure 6.16	Demographic pyramid	114
Figure 6.17	Educational attainment	115
Figure 6.18	Resident foreigner	115
Figure 6.19	Commuter flow	116
Figure 6.20	Touristic flows	117
Figure 6.21	Utilized buildings	118
Figure 6.22	Buildings types of use	119
Figure 6.23	Residential buildings materials	119
Figure 6.24	Buildings period of construction	120
Figure 6.25	Residential buildings state	120
Figure 6.26	Residential buildings floors	120
Figure 6.27	Pluviometric data for past flood events .	121
Figure 6.28	Weather station location	129
Figure 6.29	Recorded thermo-pluviometric data . . .	130
Figure 6.30	Bari-Matera 5G	132
Figure 6.31	Real use case: Surveillance camera	133
Figure 6.32	Real use case: camera framing	133
Figure 6.33	Precipitation Data (26 March 2020)	134
Figure 6.34	Grad-CAM of a rainy frame	138
Figure 6.35	Algorithm profiling	139
Figure 6.36	MatEERA logo	140
Figure 6.37	Website screenshots	142
Figure B.1	Aerial view of the NIED	155
Figure B.2	NIED experimental facilities	156
Figure B.3	NIED Large-scale Rainfall Simulator . . .	157
Figure B.4	Experiments	158

LIST OF TABLES

Table 1.1	Flood types	13
Table 1.2	Map assessment criteria	22
Table 4.1	Dataset	45
Table 4.2	Convolutional Base	48
Table 4.3	Model architecture	49

Table 4.4	Test sample	53
Table 4.5	Confusion matrix	54
Table 5.1	Rain classes - PREVIMET	60
Table 5.2	Rain classes - MetOffice	61
Table 5.3	Rain classes - WMO	62
Table 5.4	Rain classes - JMA	62
Table 5.5	Rain classes - China Meteorological Ad- ministration	63
Table 5.6	Convolutional Base	72
Table 5.7	Model architecture	73
Table 5.8	Data set - 6 class classification	76
Table 5.9	Confusion matrix - 6 classes	81
Table 5.10	Metrics by class - 6 class classification	83
Table 5.11	Data set - 5 class classification	85
Table 5.12	Confusion matrix - 5 classes	89
Table 5.13	Metrics by class - 5 class classification	91
Table 6.1	Population and density of the macro areas	113
Table 6.2	Matera weather station	129
Table 6.3	Test sample of the TIM data set	135
Table 6.4	Confusion matrix - TIM data set	136
Table B.1	Rainfall Simulator technical specifications	157

ACRONYMS

NIED	National Research Institute for Earth Science and Disaster Prevention	43
TIM	Telecom Italia S.p.A.	131
API	Application Programming Interface	30
AI	Artificial Intelligence	33
CV	Computer Vision	26
ML	Machine Learning	26
DL	Deep Learnig	31
CNN	Convolutional Neural Network	27
RMSprop	Root Mean Square Propagation	50

IoT	Internet of Things	131
WR	With Rain	41
NR	No Rain	41
NLR	No Rain or Light rain	76
HMR	High Moderate rain	76
LHR	Low Heavy Rain	76
MHR	Medium Heavy Rain	76
HHR	High Heavy Rain	76
DVR	Violent Rain, Downpour	76
TP	True Positives	54
FP	False Positives	54
TN	True Negatives	54
FN	False Negatives	54
MCC	Matthews correlation coefficient	56
WMO	World Meteorological Organization	61
JAXA	Japan Aerospace Exploration Agency	134
GSMaP	Global Satellite Mapping of Precipitation	134
5G	5th Generation mobile network	131
MATEERA	MATera Extreme Events Resilience and Awareness	139



INTRODUCTION

This research was supported by Regione Basilicata, within the School of Engineering (University of Basilicata) Ph.D. Program “Engineering for Innovation and Sustainable Development” (curriculum: Methods and Technologies for Environmental Monitoring and Protection) - Industry 4.0, topic: Enhancing flood risk management, through near real-time methods and technologies, for risk communication at local scale.

The Ph.D. here presented and entitled *A Deep Learning approach for monitoring severe rainfall in urban catchments using consumer cameras. Models development and deployment on a case study in Matera (Italy)* aims to trace a scientific-technical innovative scenario, using digital technologies (such as 5th Generation Mobile Networks and Artificial Intelligence) applied to an environmental domain as flood risk mitigation.

The process of investigation interfaced with experimental activities, contextualization, and theoretical references. The stages took place in Italy and Japan, particularly in Potenza, Matera and Tsukuba.

The study was performed in continuous collaboration with the Storm, Flood and Landslide Research Unit of the NIED - National Research Institute for Earth Science and Disaster Resilience 防災科学技術研究所, that applies advanced sensing technology developing precise observation and prediction techniques to mitigate damage from water and sediment disasters. The experiments involved the use of the NIED Large-scale Rainfall Simulator, the largest simulator in the world in terms of rainfall area and sprinkling capacity.

In order to get in touch with the production environment, the training path comprised a collaboration with TIM S.p.A. - Telecom Italia. The company offers datasets, advanced information and communication technologies, and 5G connectivity.

The extent and the cumulative aspects of impacts from natural and man-made calamitous events demonstrate the importance of disaster management, meant as a set of policies and strategies to prevent, reduce or manage the risk. For over five decades,

flooding has been the most frequent and widespread natural disaster globally (EM-DAT 2019; Pesaresi et al. 2017). The extreme weather events stemming from climate change may alter the hydro-geological regime increasing flood frequency and magnitude (de Moel et al. 2009; IPCC 2012; Autorità di Bacino della Basilicata 2010). Urban and suburban contexts present altered hydrology (Fletcher et al. 2013; Griffiths and Singh 2019). Their proper representation requires near real-time and fine-grained information retrieved from rainfall measurements at local, fine scales with low latency (Schilling 1991; Einfalt, Arnbjerg-Nielsen, et al. 2002; Einfalt, Krejci, et al. 1998). Presently, most of the rainfall data is obtained from ground-based measurements or remote sensing that may present some limitations (limited temporal or spatial resolution, high costs, underrepresentation of urban areas). In this context, one of the biggest potential is represented by low-cost opportunistic sensors. Several studies developed unprecedented techniques to retrieve precipitation information with low operational costs that can be effectively combined with conventional systems despite their inaccuracy (Tauro et al. 2018).

Technology may have pivotal importance in improving rainfall-related hazard forecasting and early warning systems. Urban flood risk management can benefit from recent technological advancements in data, communication, and computational algorithms. Recent years have seen a vast rise in the amount of data that are continuously being produced and collected for different purposes that can opportunistically yield useful information.

The general goal of this thesis was disaster resilience enhancement through a technological evolution of risk prevention.

The key idea is to combine alternative data sources and computation techniques, such as Deep Learning and Computer Vision methods, to devise a method for near real-time heavy rainfall monitoring at local scale for flood risk mitigation in vulnerable urban and suburban areas.

The specific aim was to investigate the use of easily available photographing devices as rain detectors-gauges to develop a dense network of low-cost rainfall sensors to support the traditional methods with an expeditious solution embeddable into smart devices.

Despite the diversity of purposes, methods and epistemological fields, the literature on the visual effects of the rain supports the idea of camera-based rain sensors but tends to be device-specific. As opposed to existing works, the present study focuses

on maximizing the number of image sources (like smartphones, general-purpose surveillance cameras, dashboard cameras, webcams, digital cameras, etc.). This encompasses cases where it is not possible to adjust the camera parameters or obtain shots in timelines or videos.

Using a Deep Learning approach based on Transfer Learning with Convolutional Neural Networks, the rainfall information was gathered from single photographs taken in very generalizable conditions.

The first scenario of interest for supervised learning was a binary classification whose outputs indicated the presence of precipitation: cameras act as rain detectors.

The second scenario was multi-class classification whose outputs described ranges of quasi-instantaneous rainfall intensity: cameras act as rain estimators.

The models for rainfall detection and intensity estimation were compiled, trained, validated, and tested. They were shown to produce good outcomes encompassing unconstrained verisimilar settings. The preparation of the classifiers included the preparation of suitable datasets mimicking real-world scenarios: crowd-sourced images, dashboard cameras in Japan coupled with high precision multi-parameter radar data (data owned by NIED), and experiments conducted in the NIED Large Scale Rainfall Simulator.

The outcomes were applied to a real use case, with the experimentation through a pre-existent surveillance camera using 5G connectivity provided by TIM. in the city of Matera (Italy). The application on Matera case study took into account the interrelations between the different urban and environmental issues, using innovative technologies for investigation on water-related phenomena at local scale, in order to create a matrix of urban knowledge, sustainability, decision-making processes, and risk resilience. Structural components of the territorial context result from a balance between construction and destruction across the time and dialogue with natural elements such as watercourses, vegetation, exposure, geomorphology, revealing a structure made by flows and physical actions that can be read and interpreted (Macaione and Sichenze 2013; Macaione, Ippolito, et al. 2018). In the millennial history of Matera, water played an important role in driving urban evolution as demonstrated by historical changes in systems for water collection, storage, drainage, and sewage flows. The hydrologic traits evolved across

successive generations of urban ecosystems via adaptations over the centuries, shifting according to the changes of pressures. The context aspects contribute to creating some components of a Web prototype for flood risk communication at local scale.

The results of tests and deployment were encouraging for both the binary and multi-class classification problems. The case study proved the immediate applicability at an operational level of the theoretical variables considered and methodological components chosen. The experimental activities within the “Bari Matera 5G” project provided a promising perspective on the *smart* environmental monitoring using 5G connectivity.

The best performances were obtained in heavy rainfall and no-rain conditions, whereas the mispredictions are related to less severe precipitation.

The results achieved surpass the earlier work in this area in terms of flexibility, simplicity of application, comprehensiveness of shooting tools. The proposed method relies on single image classification, thus it has limited operational requirements, can be easily and quickly implemented in real use cases, can exploiting pre-existent devices (static or moving cameras without adjusted parameters) with a parsimonious use of economic and computational resources. The model can be exposed locally, remotely or *via* cloud by programming *smart* cameras or Internet of Things devices.

Despite being a prototype, it offers a first operative tool that for creating a low-cost sensors network for the characterization of rainfall. It can contribute to the traditional monitoring networks and forecast systems for building-up a hyperlocal information infrastructure that suits the future needs in terms of spatial and temporal resolution, scalability, heterogeneity, and dynamicity. The retrieved rainfall information can have practical utility for the studies on weather-hydrological information systems at local scale in urban areas and warning systems based on the identification of a significant meteorological state for flood triggering.

This approach is especially useful in urban areas where measurement methods such as rain gauges encounter installation difficulties or operational limitations or in contexts where there is no availability of remote sensing data.

The major limitation concerns the approximations inherent in the outputs. Additional data may be gathered to address the apparent gaps and improve the accuracy of the precipitation intensity prediction. Another limitation can stem from possible

ambiguities in the visual appearance of pictures: the system does not suit scenes that are also misleading for human perception.

The overall results suggest that Deep Learning methods offer an efficient strategy for gathering rainfall information from cameras-based low-cost sensors that can be replicated, updated, fine-tuned, and extended.

New technologies and non-conventional data sources offer great potential for engagement and co-production of knowledge to improve the representation of urban precipitation fields and build-up extreme events resilience.

Future directions might be related to the enhancement of the observational capability through an increase in spatial density of rain observations by further experiments and application to crowdsourced pictures. The integration of conventional monitoring networks with *opportunistic sensing* (Dickinson et al. 2010), voluntary geographic information (Goodchild 2007), crowdsourced data can promote communication, participation, and dialogue among stakeholders and increase public awareness, emergency response, and civic engagement through the smart city (Riva Sanseverino et al. 2017) and smart community idea.

The starting point of the research in this thesis is the risk paradigm. The Part i gives a contextual summary of the theoretical and legal variables of the mitigation of the urban flooding residual risk by non-structural measures, including a synoptic conceptual background and an overview of some generic issues relating to flood communication systems.

The Part ii concerns the problem of rainfall characterization through the methods of Computer Vision and Deep Learning. The Chapter 2 provides a concise review of the relevant contributions from the existing body of the literature on the visual effects of the rain in digital still photography and video frames. For the sake of clarity, the studies were divided into three main investigative strands: techniques for removing the visual effects caused by rain, rain measurement techniques, and weather classification techniques. The analysis of existing literature lead to the definition of the research specific goals, variables and components.

The Chapter 3 is concerned with the methodology used for this study: a Deep Learning approach based on Transfer Learning with Convolutional Neural Networks to perform single image classification.

*Breakdown of the
thesis*

The preparation of the Chapter 4 and of the Chapter 5 included: a) preliminary stage for preparing datasets; b) experimental activities conducted in the NIED Large-scale Rainfall Simulator; c) creation of datasets for the employment of Deep Learning techniques for characterization of rainfall and use of several data owned by NIED; d) development, training, validation, and test of the Convolutional Neural Networks. The outcomes were immediately applied to a real-world scenario, as illustrated in the Part iii.

The Part iii brings the prior knowledge in the case study: the city of Matera (Italy). The analysis unfolded on several levels: interpreting the context aspects and the important role of rainfall from driving its unique millennial urban evolution to determining present criticality; elaborating components for a Web prototyping tool for flood risk communication at local scale; deploying the elaborated models to experimentation with a pre-existent surveillance camera using 5G network connectivity in Matera provided by TIM to prove the applicability of the method proposed.

Chapter 7 delineates the significance of the main findings and includes some suggestions for improvement and speculating on future directions.

The Appendices presents the diachronic legal framework in Italy (Appendix A), the technical characteristics of the NIED Large-scale Rainfall Simulator (Appendix B), life saving tips and rules for self-protection in case of landslides and floods (Appendix C).

PART I

THEORETICAL FRAMEWORK

1.1 THE RISK PARADIGM

The extent and the cumulative aspects of impacts from calamitous events (natural and man-made disasters) demonstrate the importance of disaster management, meant as a set of policies and strategies to prevent, reduce or manage the risk. The actions are aimed both at minimizing the losses and at augmenting the resilience. These can be distinguished between prospective disaster risk management, corrective disaster risk management, and compensatory disaster risk management (residual risk management), depending on whether the risk is future, present or residual (United Nations General Assembly 2016).

The perspective of environmental sustainability and disaster risk reduction should be holistic: it requires the systematization of several gnosiological fields and epistemological criteria.

There are involved issues related to crisis, resilience, smartness, and ecology with complex relationships.

Effective risk mitigation must take the values and the quality of different factors and heterogeneous phenomena into account (Figure 1.1).

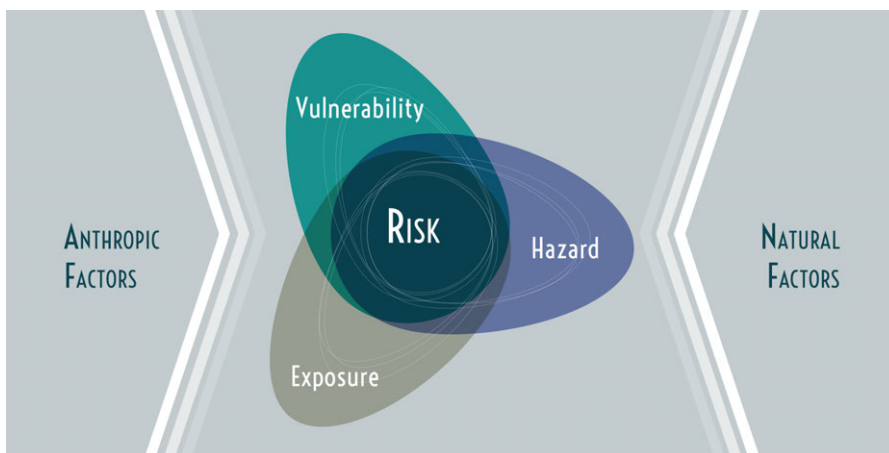


Figure 1.1: Determinants of risk.

The concept of risk is expressed by the formula:

$$Risk = hazard \times exposure \times vulnerability$$

Thus, the risk from natural hazards can be considered as a combination of three key components: *hazard*, *exposure*, and *vulnerability*, whose international agreed definitions, provided by the United Nations General Assembly (2016), are:

HAZARD: *a process, phenomenon or human activity that may cause loss of life, injury or other health impacts, property damage, social and economic disruption or environmental degradation. Natural hazards are predominantly associated with natural processes and phenomena.*

EXPOSURE: *the situation of people, infrastructure, housing, production capacities and other tangible human assets located in hazard-prone areas.*

VULNERABILITY: *the conditions determined by physical, social, economic and environmental factors or processes which increase the susceptibility of an individual, a community, assets or systems to the impacts of hazards.*

Typically, the natural hazards are illustrated in maps that are produced using probabilistic models representing the potential hazardous events that can occur in a certain area within a certain return period. Both the disaster probability and the potentially affected area depend on the time frame considered, so it may be useful to provide different hazard maps corresponding to several return periods.

The concept of return period is the most common, yet often misunderstood (UNISDR 2015), metric for the occurrence of natural hazards. It describes the likelihood of a hazard event to occur at (or above) a specific intensity within a time frame defined by a probability.

RETURN PERIOD: *is the average frequency with which a particular loss is expected to occur. It is usually expressed in years, such as 1 in X number of years. This does not mean that a loss will occur once every X numbers of years, but rather that it will occur once on average every X number of years. It is another way of expressing the exceedance probability: a 1 in 200 years loss has a chance of 0.5 percent to occur or be exceeded every year (UNISDR 2015).*

In the last 50 years, flooding have figured as the most frequent and widespread type of natural disaster, causing severe repercussions in terms of both loss of human life and socio-economic and environmental damage.

Overall, the hazardous events related to extreme weather make up the vast majority of natural disasters that were reported worldwide in the Emergency Events Database (EM-DAT 2019), an international database maintained by the Center for Research on the Epidemiology of Disasters (CRED) of the Université Catholique de Louvain (Brussels, Belgium) containing core data on technological and natural disasters from 1900 to the present day collected from various sources. The criterion that determines whether the event can be reported as a *natural disaster* is the existence of at least one of the following conditions: 100 or more affected people, 10 or more deaths, declaration of a state of emergency or call for international assistance. Due to social, political, and economical factors, a complete and homogeneous representation of all regions of the World is impossible, so the real disasters occurrence number is probably higher.

Floods alone account for an average of 37.8% of the total between 1970 and 2019, as shown in Figure 1.2, and 47.09% during 2019.

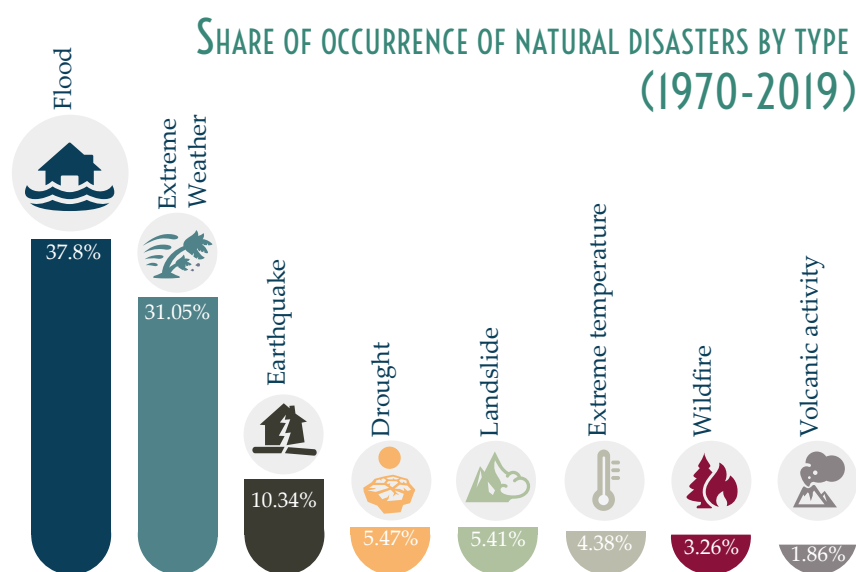


Figure 1.2: Share of occurrence of natural disasters by type, from 1970 to 2019. Data source: EM-DAT (2019)

Floods are considered major natural disasters globally and are the most common natural disaster in the European Region (Pesaesi et al. 2017), furthermore, climate change may increase their frequency and magnitude (de Moel et al. 2009; IPCC 2012) and this trend is expected to continue. The impacts of extreme precipitation events, stemming from climate change in Mediterranean Europe, include alterations in the hydro-geological regime which

could increase the risk of flash floods (Autorità di Bacino della Basilicata 2010).

The Figure 1.3 plots the annual reported number of natural disasters, categorized by type. It includes both weather and non-weather related disasters. The represented accrual over time of the number of calamitous events may indicate a critical under-reporting of disasters in the past, due to incompleteness of historical data. Nonetheless, the ratio of hydrological events remains steadily significant. The frequency of floods is growing in the last three decades, a period in which the data can be considered fairly reliable.

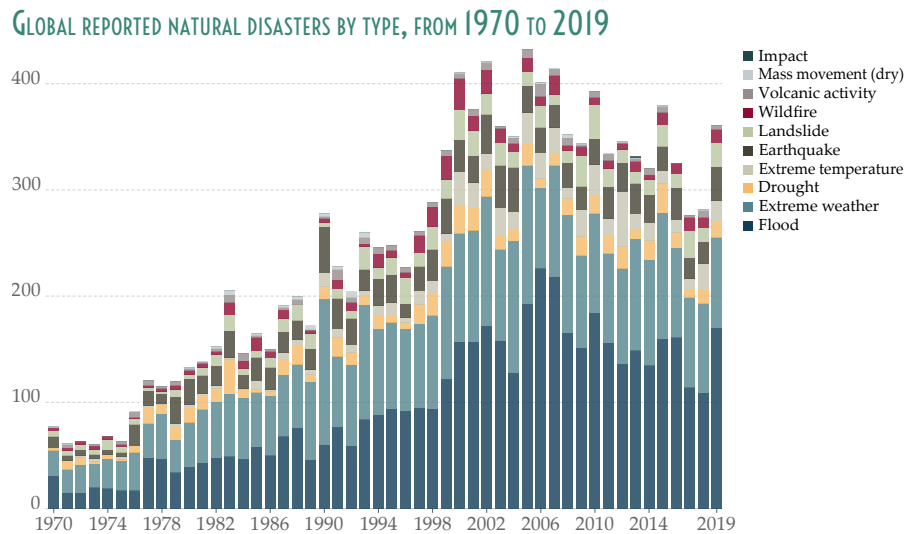


Figure 1.3: Number of global reported disasters by type, from 1970 to 2019. Adapted from Ritchie (2014), data source: EM-DAT (2019)

As thoroughly discussed by Parker (2000), floods can take many forms, so the definition for the term varies among researchers depending on the specific point of view.

Broadly speaking, we can define:

FLOODING: *a temporary condition of partial or complete inundation of normally dry land resulting from the overflow of inland or tidal waters, or from unusual and rapid accumulation of surface run-off from any source* (Shabman et al. 2014).

There are many types of flood (Parker 2000), as shown in Table 1.1, caused by different agents. The different flood types are not mutually exclusive, as they can coexist, interact and create a cascading chain of events. Thus, flood episodes are potentially

triggered by a variety of hydrological processes and their dynamics are influenced by the combination of different natural and anthropogenic driving factors. The leading cause of floods is heavy rainfall of long duration or of high intensity.

AGENT	DETAILS AND EXAMPLES
Rainfall	<i>riverine or non-riverine, slow-onset or flash flood, conventional/frontal/orographic, torrential rainfall floods.</i>
Snowmelt	<i>riverine, overland flow</i>
Icemelt	<i>glacial meltwater (rise in air temperature), glacial meltwater (geothermal heat source), spate floods</i>
Flooding during freeze-up	<i>riverine</i>
Flooding by Ice breakup	<i>riverine (also called ice-jam floods)</i>
Mudfloods	<i>floods with high sediment content</i>
Coastal/sea/tidal floods	<i>storm surge (tropical or temperate induced), ocean swell floods, percolation floods, tsunamis (induced by geological process)</i>
Dam	<i>dam-break flood, dam overtopping</i>
Sewer/urban drain flood	<i>storm discharge to sewers and drains exceeds capacity</i>
Rising water tables (high groundwater levels)	<i>many causal factors including land subsidence, rising sea levels, temporal reduction in water abstractions from aquifers</i>
Combined events	<i>examples include: riverine/tidal flooding; rain on snow floods</i>

Table 1.1: Flood types by agent (Parker 2000).

The vulnerability of urban structures demonstrates the urgency of mitigation interventions to improve the risk knowledge, dissemination and communication, response capability and monitoring and warning service. The flood sensitivity of European cities and towns is strictly linked to the potential material and human losses, which can be diminished heightening the protection levels (Kompil et al. 2015).

The urban and suburban landscapes are usually dominated by artificial impervious (or near impervious) surfaces, including different structural elements: the urban fabrics are composed of

paved areas (roads, sidewalks, parking lots, stations, industrial areas, airports, ports etc.) and buildings (rooftops).

The presence of the aforementioned impervious surfaces and drainage systems have a significant impact on the hydrological cycle (Griffiths and Singh 2019, Figure 1.4).

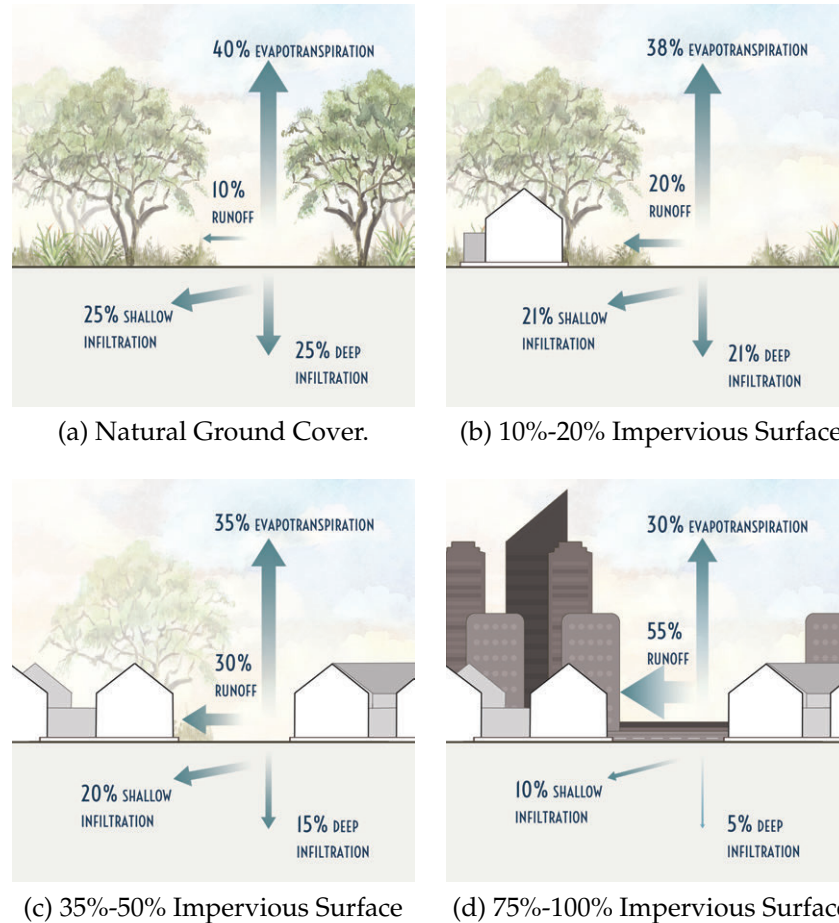


Figure 1.4: Impacts of urbanization on the hydrological cycle. Figures redrawn from the original in FISRWG (1998).

The influence of urbanization can result in increased peak flows, surface runoff volumes and flow variability, along with decreased infiltration and shorter lag times (Fletcher et al. 2013).

As a result of the described altered hydrology, extreme precipitation events are strongly relevant for urban and suburban areas, even if of short duration.

In fact, events over urban areas with the same amount of precipitation and the same duration can cause flooding faster and more severe than in areas with lower degrees of anthropization.

The intensity, duration and spatial distribution characteristics of the rainfall combined with the land use and topography,

surface conditions, vegetation, soil type, and soil water-content determine the dynamics and location of floods and related phenomena.

In this context, the meteorological forcing characterization becomes essential: the identification and monitoring of hydrological state indicators, such as rainfall levels, are a prerequisite to determine the critical thresholds for landslides or flood triggering. These indicators, together with the fragility of the system, shape the event scenarios and the risk scenarios within the territorial context and therefore the criticality and alert levels that establish the indication or warnings to the exposed population (A. Sole et al. 2013; Scarpino et al. 2018, Appendix C).

For example, the Figure 1.5 schematization represents an urban pluvial flood scenario based on the theoretical framework by Versace (2017) applied to a recent real event. The urban pluvial flood was caused by the hydraulic overload of the drainage network - due to severe weather - which occurred on 3 August 2018 in the city of Matera, Italy.



Figure 1.5: Urban flood scenario based on the theoretical framework by Versace (2017) applied on a real event in Matera.

The extreme precipitation reached a maximum cumulative precipitation in 1 h of 33 mm/h (rainfall data from the Centro Funzionale Decentrato Basilicata, Protezione Civile Basilicata n.d.), and overcame a critical threshold, triggering an event. Its relation with the fragility of the system and the territorial context determines the event and risk scenarios and therefore the behavioral measures for users (Scarpino et al. 2018; A. Sole et al. 2013).

Hence, environmental monitoring, warning and communication are crucial issues in reducing the residual risk. Rainfall data at scales of urbanized catchments is essential to evaluate the urban rainfall-runoff response. For the purpose of representation of the territory, especially for urban pluvial flood studies, the precipitation measurements are required at local, fine scales with low latency to give near real-time and fine-grained information (Schilling 1991; Einfalt, Arnbjerg-Nielsen, et al. 2002; Einfalt, Krejci, et al. 1998). The urban flood risk management can be enhanced by a local scale strategic system integrating near real-time methods, innovative technologies and conventional systems (Albano and Aurelia Sole 2018).

1.2 LEGAL FRAMEWORK

Presently, the legislative framework of flood in European Union member-state is the so-called *Flood Directive*: European Directive no. 2007/60 on the assessment and management of flood risks.

The purpose of the European *Flood Directive* is to establish a framework for the assessment and management of flood risks, aimed at the reduction of the likelihood and/or the direct and indirect impact of floods (i.e. the adverse consequences for human health, the environment, cultural heritage, and economic activity). The main focus is floods from rivers, mountain torrents, Mediterranean ephemeral water courses, and floods from the sea in coastal areas. It considers all aspects of risk management and in particular prevention, protection and preparation, including flood forecasting and warning systems.

The improvement of the knowledge about hydro-morphological processes connected with floods and the management of the associated risk goes along with the rights of public access the information and participation in the planning process.

Thus, the proposed approach to the flood risk management programs incorporates the elements of prevention, protection

(taking both structural and non-structural measures), preparedness, emergency response, and recovery and lessons learned.

The European Floods Directive has stimulated the implementation of a diversified of flood risk management strategies in member-state legislation.

The Directive has been transposed in the Italian national legislative system through the Legislative Decree 23 February 2010, no. 49 "Implementation of Directive 2007/60/EC on the assessment and management of flood risks" (*Decreto legislativo 23 febbraio 2010, n.49 "Attuazione della direttiva 2007/60/CE relativa alla valutazione e alla gestione dei rischi alluvioni"*).

Since the Unification of Italy, the legislative body on flooding hazard and in general hydro-geological risk was gradually constructed by many sectorial laws.

The shaping of policies and practices connected with natural risks had been strongly influenced by the occurrence of emergency events (e.g. the Decree Law no.180/1998, issued after the landslides in the town of Sarno in Campania region, or the Law no. 365/2000, which followed the flood of the town of Soverato in Calabria region). An overview of diachronic legal framework in Italy is given in Appendix A.

1.3 PEOPLE-CENTERED EARLY WARNING SYSTEMS AND RISK COMMUNICATION AT LOCAL SCALE

A number of structural and non-structural measures have been implemented to reduce the adverse impacts of flood. The strategy for risk management for prevention, protection and mitigation can involve technical or non-technical solutions (Plate 2002): actions on the areas of land-use planning, land management; sustainable development; construction; private sector (e.g. insurance); emergency planning; public awareness and preparedness; social involvement of communities.

Among the non-structural measures for risk mitigation and preparedness, *Early Warning Systems* provide an efficacious and cost-effective tool for reducing the residual risk and enhancing resilience (O'Sullivan et al. 2012) with multiple benefits.

The technical information is generated and disseminated dynamically and timely to the key actors (exposed communities, local authorities, fire brigade, police, medical services, urban planners and so on).

The chain of information-communication systems concerns all the capacities needed: networks of meteorological and hydrological sensors, model, event detection, decision subsystems and so forth. It forms an integrated system with the purpose of improve hazard monitoring, forecasting and prediction, disaster risk assessment, communication and preparedness.

The International Strategy for Disaster Reduction Platform for the Promotion of Early Warning (United Nations Office for Disaster Risk Reduction (UNDRR) 2006) identifies four inter-related elements in effective *end-to-end* and *people-centered natural hazard early warning systems*:

1. Risk knowledge, based on systematic data collection, risk assessments and its trends over time;
2. Monitoring and warning service, including detection, monitoring, analysis and forecasting of the hazards and potential consequences;
3. Dissemination and communication;
4. Response capability, at all levels.

Best practice early warning systems have multiple levels, strong interconnections and effective communication channels within and across sectors.

The urban pluvial flood risk assessment and management at the local scale may be a tool for providing guidance to decision makers to define policies and strategies for improving prevention, mitigation, resilience, as well as sustainability and smartness, while supporting the process of prioritizing and targeting investments for privates or public administrations and promoting communication, participation and dialogue among stakeholders to increase public awareness, emergency response, and civic engagement.

To assess the urban pluvial flood risk at the local scale, the integrated approach incorporates hazard modeling, social and physical vulnerability assessment indices, and coping capacity measures (Elboshy et al. 2018, Figure 1.6).

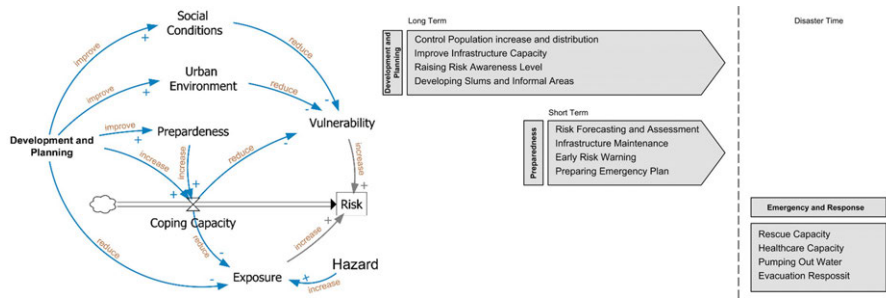


Figure 1.6: Risk management at local scale: conceptual model, stages and related factors. Reproduced from Elboshy et al. (2018).

The development of monitoring and early warning services is built upon the foundation of risk knowledge.

The monitoring process consists of observation, measurement and prediction of relevant hydro-meteorological parameters. Detection, analysis and combination from various sources (including monitoring networks and specific innovative and/or low-cost sensors, see Part ii) involves the harmonization of scientific methods with novel technologies and local knowledge. A model based on based on the co-production of knowledge, combining local and expert knowledge, can improve the level of flooding details and institutionalize this local knowledge, thereby increasing community resilience and trust (Orr et al. 2015).

As previously said in Section 1.1, in the context of precipitation-induced disasters early warning systems, the characterization of the meteorological forcing has a pivotal role. Proper rainfall thresholds identify the precipitation values (in terms of rainfall rate, duration and space extent) that may induce critical state functioning as a trigger for the prevention and emergency system alert (Georgakakos 1995; Montesarchio et al. 2009). It is possible, depending on the associated event and risk scenarios, to define schemes to use the rainfall thresholds for estimating criticality levels (ordinary, moderate and severe), which are associated to warning levels, according to Italian emergency plans (De Luca and Versace 2017).

Several community-based early warning systems developed for floods and natural disasters in general have proved effective for the issuance of the warning, the response and feedback, especially when they benefit from available technologies and local capacities (Macherera and Chimbari 2016).

Risk communication represents a continuous exchange of information and data integrated into the assessment and management process (Lang et al. 2001), with the main purposes of preparation – information, prevention and warning (Orr et al. 2015).

The human processing and perception of technical data and uncertainties surrounding risks benefit from design and linguistic strategies, methods and theories derived from socio-hydrology (Viglione et al. 2014; Di Baldassarre et al. 2013), psychology, neuroscience and evolutionary social sciences (Tucker et al. 2008; Ratna Reddy and Syme 2014). The internal risk communication between managers and assessors ensures that risks are fully evaluated, understood and managed. The external communication facilitates the empowerment of the stakeholders and public informedness, takes into account the emotional response and the decision making process preventing negative behavior whereas encouraging constructive responses to an event (Bell and Tobin 2007; F. Yamada et al. 2011; Fukuzono et al. 2006).

In a multi-disciplinary approach harmonizing methods from natural and social sciences, the flood disaster risk assessment should consider factors that influence the dynamics of risk perception and behavioral dynamics, such as flood experience, risk communication (Aerts et al. 2018; Thistlethwaite et al. 2018; Poussin et al. 2014; Renn 1991; Covello 1991; Lichtenberg and MacLean 1991, Figure 1.7).

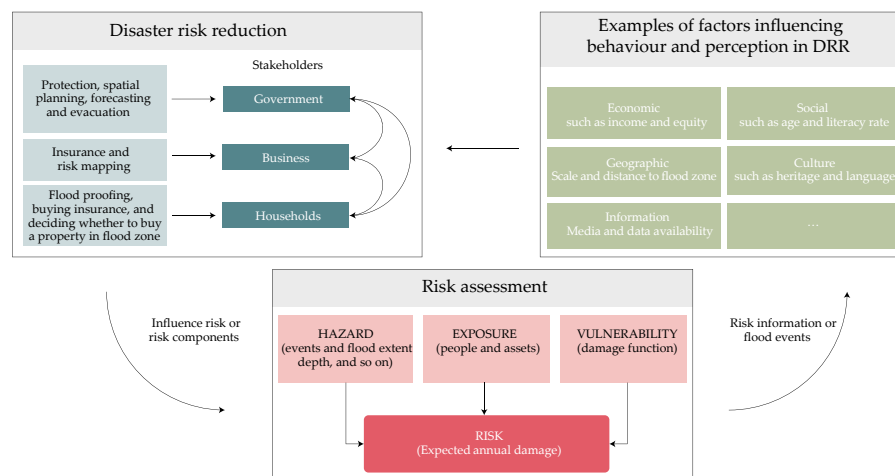


Figure 1.7: Extended risk assessment framework including behavioural factors and disaster risk reduction. Reproduced from Aerts et al. (2018).

The effectiveness of risk communication messages and strategies requires to establish trust and credibility (Peters et al. 1997; Slovic 1999; Renn and Levine 1991), in advance of the actual event. The basic factors that determine trust and credibility in environmental risk communication are: knowledge and expertise; openness and honesty; and concern and care (Peters et al. 1997).

The interplay of psychological, social, cultural, and political factors (e.g. emotions, egalitarian or individualist worldview, etc.) can amplify or attenuate public perception of risk and shape behavioral patterns (Slovic 1999; Renn 1991).

For example, risk probability can be rendered in different formats (return periods, frequencies, rates, percentages, verbal expressions, etc.). Thus, communicating risk probability information to the general public may be difficult and affect the risk perception, understanding, attitude, and behavioral response (Visschers et al. 2009).

User-centered design and visualizations are a powerful tool to convey information about unfamiliar and complex subject matter, resulting in enhanced dissemination, knowledge exchange and user engagement (Grainger et al. 2016; Henstra et al. 2018; Charrière et al. 2012; Hagemeyer-Klose and Wagner 2009, Table 1.2). The attributes of hazard maps play a fundamental role in the transition from visual to cognitive and emotional representation and comprehension which determines beliefs, intentions, and decision-making processes, according to laws ranging from semiotics to *Gestalt* to visual psychology. The meaning derived from maps and the response to risk information (monitoring and mitigation intentions) are substantially influenced by socio-cultural conventions, e.g. the commonly understood meaning of stoplight color system, together with personal characteristics of the viewer, e.g. the gender: females tend to have stronger risk beliefs and intentions to mitigate risk (Slovic 1999), degree of numeracy: the ability to use numbers and mathematical approaches for real life problem solving; prior beliefs and experiences (Severtson 2013; Palka et al. 2013, Figure 1.8).

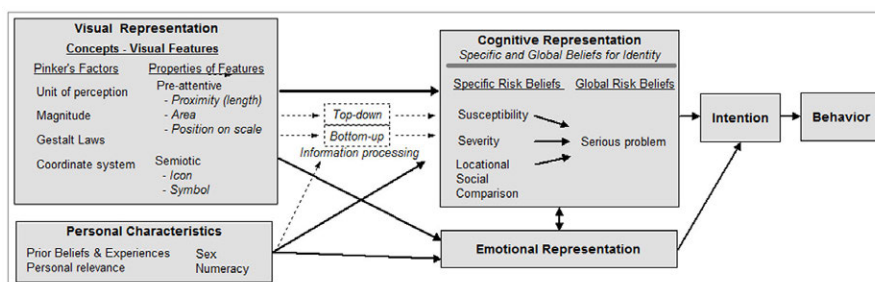


Figure 1.8: Representational and behavioral framework: from the visual stimuli to response. Reproduced from Aerts et al. (2018).

The warnings and all the information are effective when they comprise the following characteristics: informativeness, under-

CRITERION	DESCRIPTION
Personalized experience	<i>enables users to find information specific to their property (e.g., postal code search to locate property in relation to flood hazard)</i>
Local context	<i>contains identifiable places or landmarks (e.g., major and minor roads; public buildings; neighborhood names) that help an individual visualize the likely spatial extent of flooding</i>
Historical context	<i>depictions of past flood events (e.g., photographs; victim testimonials) to help users understand potential impacts</i>
Legend legibility	<i>clear explanation of lines, symbols, colors and terminology</i>
Flood zone legibility	<i>easy for the user to distinguish the extents of the flood hazard zone</i>
Explanation of technical terms	<i>meaning of terms is understandable to a lay audience</i>
Risk reduction advice	<i>paired with information about the consequences of flooding and preventative or precautionary actions that residents can take (e.g., install a backwater valve; buy flood insurance)</i>
Transparency about limitations and uncertainty	<i>provides information about types of flooding depicted and/or potential exposure of areas adjacent to the flood lines</i>
Depiction of multiple flood hazards	<i>depicts all forms of flooding to which a property is exposed (e.g., coastal, riverine, and pluvial)</i>

Table 1.2: Map assessment criteria. Adapted from Henstra et al. (2018).

standability, accurateness, unambiguousness, trustworthiness, audience, reach varying audience capacity, timeliness, reliability. The content desired by users (Rollason et al. 2018) should include details on timing, location, scale, impact, probability and response. An effective and participated communication seeks to develop a local *flood literacy* (Rollason et al. 2018) that can give rise to the build-out of resilience at a community level, increase in awareness, and/or behavioral change.

Near real-time methods and technologies are crucial to enhance flood risk management and risk communication at local scale. Digital data tools and novel technologies have expanded and developed rapidly in recent years, setting up a potential support for flood disaster risk reduction. Tools such as geographical information systems, automated gauges, volunteered geographic information, crowdsourced data can aid flood disaster risk reduction by intervening on its components hazard, vulnerability and exposure (McCallum et al. 2016).

PART II

RAINFALL ESTIMATION THROUGH DEEP LEARNING

As was mentioned in the previous chapter, for the purpose of representation of the territory, especially for urban pluvial flood studies, the precipitation measurements are required at local, fine scales with low latency to give near real-time and fine-grained information. To move from point measurements to a spatially accurate distribution it may be useful to build a high-density monitoring network system.

Research into precipitation measurement has a long history. Traditionally, rainfall has been assessed by employing several kinds of rain gauges (Strangeways 2010). Presently, most of the available data is obtained from ground-based measurements or remote sensing that provide limited information in terms of resolution (temporal or spatial). Other problems with this kind of data are related to their high costs. Rain gauges are unevenly spread and frequently placed away from the urban centers. Not all gauge observations are continuous and available to the public and often have their limitation due to the variability of the precipitation (Kidd et al. 2017). To overcome these limitations and provide a more detailed overview, it may be useful to employ a form of aggregation of data obtained from a dense network whose nodes are represented by numerous low-cost inaccurate sensors. Thus, several studies developed unprecedented approaches to retrieve precipitation information with low operational costs. Despite their inaccuracy, novel techniques could furnish valuable additional information in combination with conventional systems (Tauro et al. 2018).

2.1 RAINFALL AND COMPUTER VISION: STATE OF ART

The first discussions of a camera designed to photograph rainfall emerged during the 1950s with the *Raindrop camera* (Jones and Dean 1953), constructed with the specific purpose of measuring the dimensions of precipitation particles to support radar investigations. The film photography based system incorporated optical devices and electronic flash equipment and was capable of measuring raindrops larger than 0.5 mm to an accuracy of 0.3 mm.

The idea of a Camera Based Rain Gauge was suggested by Nayar and Garg (2005). In their pioneering investigation, they conducted systematic studies of the visual effects of the rain in pictures and video sequences setting the key theoretical framework (Garg and Nayar 2007) for all later research.

In fact, the presence of rain produces local variations in the pixel's intensity value of digital images. The appearance of rain streaks and the stationary drops depends on the intrinsic characteristics of the raindrops (shape, size, velocity, density), but also on the camera parameters (namely exposure time, F-number, depth of field, etc.) and the environment characteristics (scene brightness, background, etc.).

The literature on the perceptual properties of atmospheric precipitation in images has highlighted different approaches. The most recent advances in the field of Computer Vision (CV) and Machine Learning (ML), the new methods of analysis of digital photography and image processing, have facilitated the study of novel rain detection systems aimed at enhancing the visual aspects to increase the rainfall detection or to remove the raindrops and rain streaks from images and video frames.

For the sake of clarity and without any claim to exhaustiveness, three main investigative strands can be identified:

- A. techniques for removing the visual effects caused by rain
- B. rain measurement techniques
- C. weather classification techniques.

2.1.1 *Rain removal techniques*

A considerable amount of literature has been published on rain removal techniques (Shorman and Ali Pitchay 2016; Tripathi and Mukhopadhyay 2014) to enhance the adverse weather degraded outdoor images or videos for different applications, such as image or video editing, surveillance vision system and Vision-based Driver Assistance Systems (Hassim and Bade 2015).

A monocular raindrop detection system in single images based on a photometric raindrop model approach to improve image registration in rainy weather condition was presented by Roser and Geiger (2009). The applicability of the method to real-world scenarios was proven with the experimentation on video sequences taken from a moving vehicle.

An Intelligent Transport System oriented study identifies the unfocused raindrops on a transparent screen using a spatio-temporal approach to achieve real-time detection (Nashashibi et al. 2010). The rainfall was evaluated according to the number of detected raindrop laying on the windscreen and discretized in four states: no rain, light rain, medium rain, and heavy rain. The algorithm was tested within the ICADAC French-German project which objective is to Improve Camera based Detection under Adverse Conditions.

Classical Computer Vision techniques were applied for the detection of dynamic weather phenomena (snow and rain) in videos (Bossu et al. 2011). The rain detection process applied to a video comprised several stages: background subtraction for foreground moving objects detection, segmentation of potential rain streaks, and selection by dimension. The computation Histogram of Orientation of rain or snow Streaks (HOS) allows to distinguish the rain or snow pixels and to estimate the precipitation intensity value.

DerainNet is a Convolutional Neural Network (CNN) architecture aimed to remove rain streaks from a single image (Fu et al. 2016). The used training data set contains random *clean* outdoor images from the UCID data set (Schaefer and Stich 2003) and Google Images Search to represent the absence of adverse meteorological conditions and the same images edited with an Adobe Photoshop™ effect to simulate the presence of rain.

Also in further studies, the rain removal problem from a single image was addressed by developing a deep learning architecture (W. Yang et al. 2016). In this case, the multi-task model is trained to learn the binary rain streak map, the appearance of rain streaks, and the *clean* background (the desired output).

Katre and Dodkey (2017) proposed a single-image rain detection and removal algorithm based on subsequent operation of orientation filter, entropy maximization and background estimation taking advantage of the abrupt local changes between the intensity of the pixels corresponding to the raindrops and the background intensity.

Haurum et al. 2019 implemented a system based on a 3D CNN for the stand-alone rainfall detection from video-frames sequences with a temporal stride of 8 frames. They aimed at using existing surveillance cameras as rain detector to decide whether to apply removal algorithms.

In comparison with image sequences or video, single images comprise information about the recorded scene *per se* as they can

stand on their own, with consequent decrease in the amount of data that needs to be processed, stored, and transferred.

2.1.2 *Rain measurement techniques*

Whereas the existing literature on techniques for removing the visual effects caused by rain is fairly extensive, bearing in mind the recentness of major advances in digital photography, there is a smaller body of literature that is concerned with the field of rain measurement techniques.

Parajka et al. (Parajka et al. 2011) proposed a monitoring system through pictures for hydrological purposes at the small catchment scale. Their approach, however, as well as previous studies, focus on snow characteristics gathered from time-lapse photography and the snow precipitation visual features are significantly different from those of the rain precipitation.

A fully analytical measurement technique, based on fundamentals of camera optics and intrinsic rain characteristics, allowed to estimate the rain rate in terms of expected values and associated uncertainty with errors of the order of $\pm 25\%$ from pictures taken at adjacent time steps with stationary background (Allamano et al. 2015).

Image Processing based Rain Drop Parameter Estimation system (IPRDPE) is an image processing tool that process video frames collected from a high definition camera to measure the rainfall according the number of drop and its volume (Kolte et al. 2016).

Dong et al. (2017) proposed a classical image processing based method for real-time rainfall rate measurement from videos, counting the focused raindrops in a small depth of field to calculate a raindrop size distribution curve and estimate the corresponding rainfall rate. The raindrop detection was achieved through gray-tone functions and direction of rain streaks; the focused raindrop selection was based on average colour tensor response and average intensity difference. The algorithm was tested on videos taken by a SONY DSR-PD198P video camera with fixed parameters adjustment.

Recently, Jiang et al. (2019) proposed an *opportunistic sensing* (i.e. unconventional data collection) in hydrology by measuring rainfall intensity in videos acquired by surveillance cameras under specific settings. Their approach employs a convex optimization algorithm to decompose an image into a pure rain-streak layer and a rain-free background layer. Then, it estimates the instantaneous rainfall intensity via geometrical optics and

photographic analyses. The effectiveness and robustness was evaluated on synthetic numerical experiments (i. e. images processed in Adobe Photoshop™) and field tests, reaching a mean absolute error of 21.8%.

These techniques strongly rely on the image resolution, temporal information, acquisition device characteristics and proper setting of its parameters in order to obtain shootings suitable for the image processing that depicts accurately detectable raindrops and rain streaks.

2.1.3 *Weather classification techniques*

Adopting a ML approach, researchers have been able to devise robust algorithms for weather classification from single outdoor images, considering different weather categories.

The analysis of pictures captured by in-vehicle vision system was found to be useful to recognize weather conditions (Yan et al. 2009). Three main features were the determinant of discriminative information: the Histogram of Gradient Amplitude (HGA) that represents the degree of sharpness of an image; the Hue Saturation Intensity Value (HSV) colour histogram that indicates the brightness and contrast of the pixels, and Road Information that detects the Region of Interest (ROI). The Recognition Algorithm based on Real AdaBoost, employing the category structure to achieve the task of classification. The output consisted in three weather categories: Sunny, Cloudy, Rainy. The model reached an overall accuracy of 91.92% (96.00% for sunny images, 89.35% for cloudy images, and 90.41% for rainy images).

The *Two-Class Weather Classification* (Lu et al. 2014) relies on a collaborative learning approach for labelling single outdoor images as either sunny or cloudy. The obtained data set (*Weather Image Dataset*) comprises 10000 pictures belonging to the two aforementioned classes.

The mentioned data set was used to fine-tune a *Weather-CNN* Architecture (Elhoseiny et al. 2015) based on the same weather classes, achieving a 82.2% normalized classification accuracy.

A scene-free multi-class weather classification based on Multiple Kernel Learn (MKL) algorithm identifies as weather features were both local (i.e. sky, shadow, rainstreak, snow flake, dark channel) and global (i.e. contrast, saturation) image features (Zhang et al. 2016). Rain and snow were detected, respectively, as Histogram of Oriented Gradients (HOG) and as a kind of noise. The approach was evaluated on the *Multi-class Weather Image*

*Machine Learning
approach and
datasets*

(MWI) set, containing 20000 outdoor images (Sunny labelled: 10815, Rainy labelled: 2342, Snowy labelled: 2226, Haze labelled: 5004).

Image2Weather (Chu et al. 2017) is a large-scale image data set associated with weather information aimed to facilitate weather property estimation from a single image. It is freely available for research purposes. The different weather conditions are represented by 183798 images in JPG format. Starting from the URL and photo ID available in an existing image collection (i. e. the *European City 1 Million EC1M dataset*), the Chu et al. web crawler associates images with heterogeneous metadata. In the first step the picture are collected from the web using the Flickr API with their metadata containing information about capture time, location (latitude and longitude) and tags. The images were collected through the Flickr Application Programming Interface (API), then characterized with the Google Maps API and finally associated with meteorological information using the Weather Underground API: each given picture taken at time t is labelled as sunny, cloudy, snowy, rainy, foggy or other according to the temporally closest meteorological information measured by the spatially closest station (the distance between the meteorological station and the shot location is less than 4 km).

Additional set of data are available, such as the *Cerema AWR Adverse Weather Rain* and the *Cerema AWP Adverse Weather Pedestrian* data set which were originally designed for the assessment of the effect of adverse weather condition (i. e. the presence of rain and fog) in terms of loss of performance of Intelligent Transport Systems. These data sets include pictures containing both digitally simulated rain and rain obtained in a controlled laboratory environment.

Despite the diversity of purposes, methods and epistemological fields, all the studies on the visual effects of the rain support the hypothesis that photographs can provide useful information on precipitation and that digital image acquisition devices can function as rain sensor.

However, the literature focused on the use of a single image source: dashboard camera, i.e. cameras mounted under the windshield of a vehicle (Nashashibi et al. 2010; Roser and Geiger 2009; Yan et al. 2009); surveillance cameras (Haurum et al. 2019; Jiang et al. 2019; Dong et al. 2017; Bossu et al. 2011); outdoor scenes (Chu et al. 2017; Elhoseiny et al. 2015; Katre and Dodkey 2017;

W. Yang et al. 2016; Zhang et al. 2016; Lu et al. 2014); devices with adjustable shooting setting, like exposure time, F-number, depth of field, etc. (Allamano et al. 2015; Dong et al. 2017; Jiang et al. 2019; Kolte et al. 2016; Parajka et al. 2011). Proposed methods often exploit temporal information requiring videos, frames or sequential still images (Allamano et al. 2015; Bossu et al. 2011; Dong et al. 2017; Haurum et al. 2019; Jiang et al. 2019; Kolte et al. 2016; Nashashibi et al. 2010; Parajka et al. 2011; Roser and Geiger 2009). Thus, the literature focused on use cases with stringent operational requirements, so it lacks heterogeneity and generalizability and tend to be device-specific.

The final goal of this research is the characterization of rainfall for creating a dense network of low cost sensors to support the traditional data acquisition and collection methods with a relatively expeditious solution, easily embeddable into smart devices, benefiting from the aforementioned research progress and the advances in available technology, using Deep Learning (DL) techniques.

Aim of the thesis

The specific aim is to investigate the use of available photographing devices as rain detectors (Chapter 4) - gauges (Chapter 5) in order to obtain a sensing network as dense as possible. It is desirable, therefore, to maximize the number of image sources to provide a large informative and reliable database. As opposed to existing works, the focus of our model is the applicability on all easily accessible image acquisition devices (like smartphones, general-purpose surveillance cameras, dashboard cameras, webcams, digital cameras, etc.), including the pre-existent ones. This encompasses cases where it is not possible to adjust the camera parameters to emphasize rainfall appearance or obtain shots in timelines or videos. The proposed methodology has a number of attractive features: application simplicity; adherence to the physical-perceptual reality; cost-effective observational and computational resources. In fact, the classification task was performed on single photographs taken in extremely heterogeneous conditions by commonly used tools. The input data can be gained from different acquisition device in different lighting conditions and without special shooting settings, within the limits of visibility (i.e. human visual perception). Shots in timelines or videos are not required, so it can be possible to use also in pre-acquired images taken for other purposes. In an attempt to adhere physical-perceptual appearance of real rain, any form of digitally simulated rain was excluded from the input data.

The field of Artificial Intelligence (AI) encompasses a huge variety of sub-fields (Figure 3.1) and addresses the challenging aim of solving problems that are easy for humans to perform but hard to describe formally mimicking the human intelligence in completing tasks such as natural language processing, recognizing faces in images, sentiment analysis, and others (Goodfellow et al. 2016; LeCun et al. 2015; Russell et al. 2010).

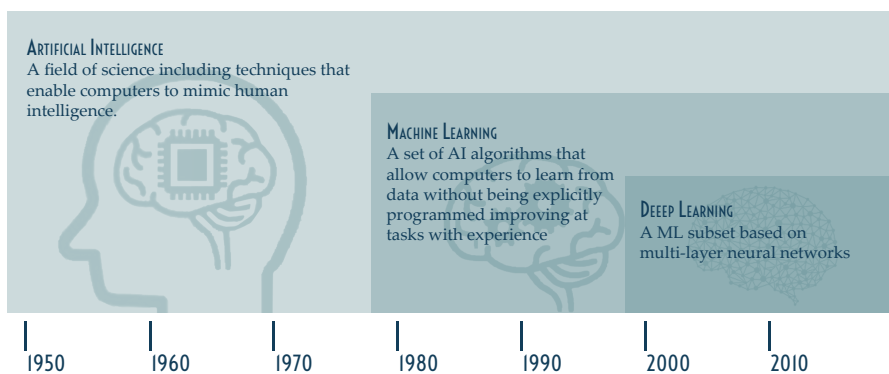
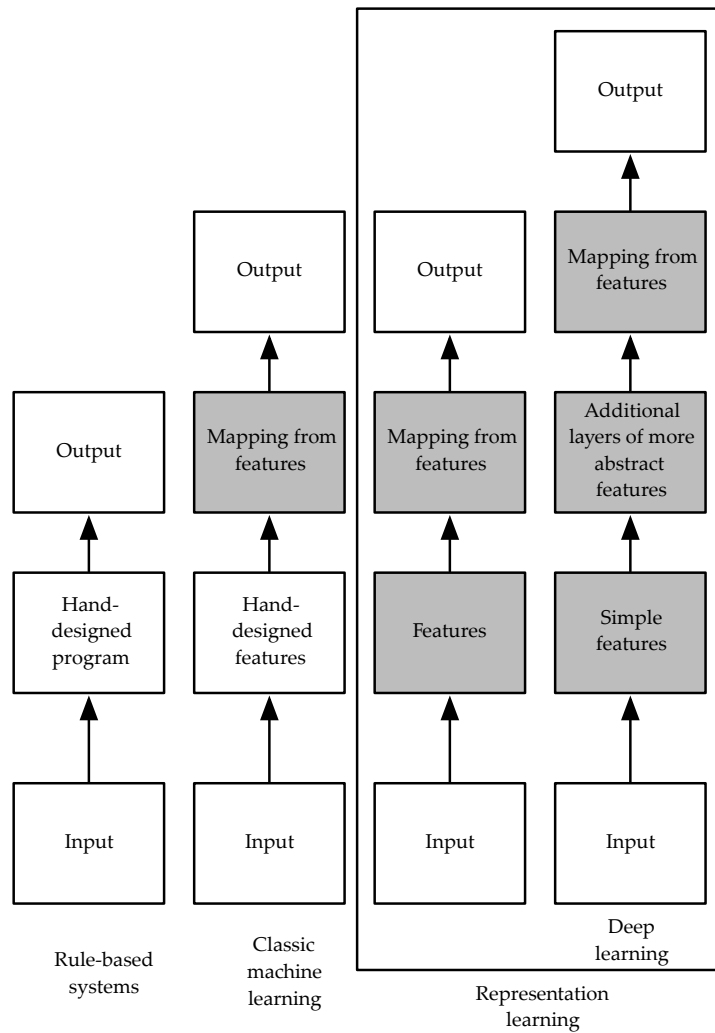


Figure 3.1: Timeline of Artificial Intelligence, Machine Learning, Deep Learning.

The traditional programming paradigm requires the definition of a comprehensible mathematical model to describe the phenomenon of interest, entailing data collection, formulation of hypothesis on patterns in the data, and validation with respect to the real data-generating process. The interpretation and modeling may be problematic for problems involving multiple complex or non-intuitive phenomena.

As opposed to this, ML is based on prediction: the training system is fed a large set of data (inputs paired with the known desired outputs), learns from the data, and matches the underlying pattern that rules the phenomenon, forming a predictive model which minimize the error between the actual and the predicted outcome. The main advantage of ML method is that it uses algorithms that iteratively learn from data and allows computers to solve a problem without being explicitly programmed how to do it (Samuel 1959).

The flowchart representing the relation between different parts of AI systems is schematically shown in Figure 3.2 (Goodfellow et al. 2016); shaded boxes indicate the components able to learn from data.



(Goodfellow 2016)

Figure 3.2: AI system parts and components learning from data. Reproduced from Goodfellow et al. (2016).

Using ML approach, in particular DL techniques such as CNN models, researchers have been able to provide robust algorithms to solve new and complex problems in the domain of digital image processing (LeCun et al. 2015), including image classification in disparate contexts with greater accuracy compared to traditional CV techniques (Mahony et al. 2020).

3.1 DEEP LEARNING FOR COMPUTER VISION: CONVOLUTIONAL NEURAL NETWORKS

DL is a subset of ML based on artificial neural networks with representation learning. The artificial neural networks, inspired by information processing and distributed communication nodes in biological systems, are composed of layers of interconnected artificial neurons. Each neuron can take simple decisions and feed them to other neurons. The power and scalability of neural networks derive from the complexity of the connections these neurons can form. A *shallow* neural network has only three layers of neurons (the input layer that accepts the independent variables or inputs of the model, one hidden layer, and the output layer that generates predictions), whereas a *deep* neural network has two or more hidden layers of neurons that process inputs.

Thus, DL is characterized by deep stacks of computations that grant the untangling of intricate and hierarchical patterns that characterize real-world datasets. Deep architectures contain multiple levels of abstraction and possess the ability to learn complex, non-linear, and high-dimensional functions. The processing layers learn representations of data with several levels of abstraction (LeCun et al. 2015). Learning means finding a combination of model parameters that minimizes a loss function (cost function) for the given training data set samples and their corresponding targets. The backpropagation (backward propagation of errors) algorithm regulates the changes of the machine internal parameters that are used to compute the representation in each layer from the representation in the previous layer.

The DL for CV techniques, namely CNN models (Khan et al. 2020), are widely used in as image-classification applications so appeared especially suitable for this purpose as they are inspired by the structural and the functional characteristics of the visual cortex of the animal world. Using a semiotic perspective (Eco 1986), the photographs can be defined as *iconic indexes* and the labels describing the desired object as *symbols*: CNN architectures transform the photographs to symbols acting as an *interpretant*, thus mimicking the functioning of the biological visual systems. A CNN based approach was chosen since it is the state-of-art among other image recognition methods (Srinivas et al. 2016; Razavian et al. 2014; Khan et al. 2020).

Convolutional Neural Networks (CNNs) are artificial neural networks that use convolution in place of general matrix multiplication in at least one of their layers (Goodfellow et al. 2016).

The general CNN structure consists of a series of layers implementing feature extraction and classification: the densely connected layers learn global patterns in their input feature space while the convolution layers learn local patterns (Chollet and Allaire 2018).

One benefit of the CNN models is that they avoid the problem of pre-processing input data since such algorithms recognize visual patterns directly in images represented by pixels. A digital raster image contains a fixed number of rows and columns of pixels, each with finite, discrete quantities of numeric representation for its intensity or gray level. DL breaks the mapping from a set of pixels to object identity into a deep sequence of nested simple mappings, each described by a different layer of the model. The transformation implemented in the layer is parameterized by its weights. Each layer includes a linear transformation controlled by learnable parameters (weight and biases) and a non-linear transformation called activation function. The most used activation functions are usually non-linear functions like Sigmoid, TanH (Tangent Hyperbolic), and ReLU (Rectified Linear Unit). A loss function (objective function), matching the type of problem addressed, measures the quality of the network's output computing a distance score between the predictions of the network and the true targets. The loss score is used as a feedback signal to adjust the weights in a direction that minimizes the loss function (cost function). The magnitude of the move is defined by the learning rate. The optimizer implements the backpropagation algorithm, which computes the gradient of the loss function with respect to the weights proceeding backward through the network. The optimizer specifies how to use the gradient to tune the parameters in order to minimize the cost function. It could be Root Mean Square propagation (RMSProp) optimizer, Adaptive Moment estimation (ADAM), Stochastic gradient descent (SGD) with Nesterov momentum, and so on.

The image is presented at the input layer, so named because it contains the variables that are visible to humans. Then series of increasingly abstract hidden layers extract features from the image. The intermediate layers in between input layers and output layers are called "hidden" because their values are determined by the model that learns which concepts are useful for explaining the relationships in the observed data. Broadly speaking, the first hidden layer identifies edges by comparing the values of the neighboring pixels. Recognizing collections of edges in the first image description, the second hidden layer search corners and

extended contours. Starting from the image description in terms of corners and contours, a third hidden layer detects the parts of specific objects and so forth.

The final description of the data is obtained by learning abstract representations that can be used to recognize the objects present in the image.

A convolution layer uses filters that perform convolution operations on an input image; its hyperparameters include the filter size and stride, the resulting output is the matrix formed by sliding the filter over the image and computing the dot product called feature map or activation map. The matrix of values (weights) that is multiplied with the input is also called kernel. Hence, a spatial convolution of the kernel is used to extract the relevant feature from an input image. A feature is a piece of information about the content of an image. Different filters act as feature detectors from the original input image: operations such as edge detection, sharpen, and blur can be performed just by changing the numeric values of the filter matrix. Features may be specific structures in the image (points, edges, or objects), the result of a general neighborhood operation or feature detection applied to the image, related to motion in image sequences, or to shapes defined in terms of curves or boundaries between different image regions.

A pooling layer implements a downsampling operation of feature maps to reduce the spatial size of the representation and thus the number of parameters and amount of computation in the network. It is typically applied after a convolution layer, resulting in more robust down sampled feature maps introducing some spatial invariance. Hereby small translations of the input don't produce a change in the values of most of the pooled outputs. Max and average pooling take the maximum (most activated presence of a feature) and average value, respectively.

A fully connected layer operates on a flattened input, each input is connected to all neurons. Fully connected layers are usually placed towards the end of CNN architectures and can be used to optimize objectives such as class scores.

Traditional CV techniques use manually made feature descriptors for object detection. The features must be informative, non-redundant, and not susceptible to recall bias. Manual feature engineering can become quite complex and cumbersome in novel problems. It requires a meticulous trial and error process to decide which features are more descriptive or informative for the desired task. Moreover, the feature definition requires dealing

with several manually fine-tuned parameters. CNN models automate the process of feature engineering, learning kernel values that can extract latent features. The machine is trained on the given data and discovers the underlying patterns in classes of images, learning automatically the most descriptive and salient features - that can be very subtle and inconspicuous - with respect to the addressed task benefitting from the DL concept of *end-to-end* learning (Mahony et al. 2020).

In addition to such simplicity, CNN models and frameworks provide great scalability, versatility and flexibility because can be re-trained and re-purposed using a custom dataset of arbitrary size or any use case, whereas CV algorithms tend to be more domain-specific (Mahony et al. 2020; Chollet and Allaire 2018).

The visual effects of rain presence in pictures are complex and often inconspicuous due the unique physical properties of rain (Garg and Nayar 2007). The supply of data inherent in the problem is limited due to the lack of public dataset of big dimensions and the difficulties of data collection or creation. The non-trivial nature of the task of interest and the small size of the available image dataset meant that one of the most effective strategies to use Convolutional Neural Networks (CNNs) it was the transfer learning approach (Pan and Q. Yang 2010; Yosinski et al. 2014; Weiss et al. 2016) combining fine-tuning and freezing layers strategies.

TRANSFER LEARNING: This ML technique exploits the knowledge acquired in one setting to improve generalization in another setting: in the context of a supervised learning for image classification, the semantics of the inputs are the same but the target are of a different nature, as any visual categories share low-level notions of edges and visual shapes, the effects of geometric changes, changes in lighting, etc. (Goodfellow et al. 2016). The available pre-trained models are typically developed by research institutes for standard computer vision benchmark datasets, such as the *ImageNet*¹ image recognition tasks. The first part of the networks pre-trained on a large-scale general dataset can be employed as convolutional base (feature extraction) for a new classifier trained on the new target dataset and new task of interest; the transferred features can be frozen (the weights are not updated during training) or fine-tuned

¹ <http://www.image-net.org/>

(Yosinski et al. 2014; Chollet and Allaire 2018). The convolutional base of the pre-trained model. A major advantage of re-purposing a network that was previously trained on a large-scale image-classification dataset is the portability of the learned features. The feature maps show the presence of generic concepts over a picture that are likely to be useful for the most computer-vision tasks. Thus, the spatial hierarchy of features can work as a generic model of the visual world for novel perceptual problems (Chollet and Allaire 2018). Transfer learning has the benefit of decreasing the training time and can result in lower generalization error.

FREEZING LAYERS: Deep networks trained on natural images all tend to learn first-layer features that resemble either Gabor filters or color blobs, independently from the chosen dataset and task. On contrary, the last layer depend greatly on the chosen dataset and task. So we can consider first-layer features as *general* (applicable to many datasets and tasks) and last-layer features as *specific* (Yosinski et al. 2014). The freezing layer approach prevent the weights from being updated during the training of the new network so as to preserve the representations that were previously learned and avoid overfitting that can result from training (fine-tuning) on medium or small datasets and large number of parameters.

FINE TUNING: The pre-trained model used as convolutional base may need to be adapted or refined on the input-output pair data available for the second task of interest. Fine-tuning consists of jointly training both the new layers added to the base and some part of the base (the last-layers containing specific features). This strategy slightly adjusts the more abstract representations of the model being reused, for making them more relevant for the problem addressed, while the other parts of the pre-trained convolutional base remain frozen.

The choice of whether freeze or fine-tune the layers depends on the size of the base and new dataset, the number of parameters and the features characteristics to obtain a fair compromise between goodness of fit and accuracy (Yosinski et al. 2014).

The task of detecting rainfall can be achieved through the analysis of the perceptual aspects that determine whether the single photograph in heterogeneous scenes represents a condition of

"presence of rain" or "absence of rain". For obvious reasons the two conditions are mutually exclusive classes. The first scenario of interest for the proposed study is a case of supervised learning of binary classification type (Murphy 2012): the objective is to learn a mapping from known inputs x (pictures) and outputs y_i (labels), where $i \in \{1, \dots, C'\}$, with C' being the number of classes. In the binary case $C' = 2$, so it's assumed that there are two classes corresponding to the considered weather conditions: C_1 and C_2 . The model aims to generalization, that is to say generating accurate predictions on novel unseen inputs, associating a picture to a label.

The output result of the binary approach allows the detection of the presence of precipitation (without a quantification), which is a necessary condition but not sufficient for the creation of a rain gauge network based on cameras.

Similarly, the task of quantifying the rainfall intensity can be achieved through the analysis of the perceptual aspects that determine whether the single picture represents a significant weather condition (classifying the rainfall intensity into ranges). In this case, the conditions form multiple mutually exclusive classes. The second scenario of interest can be modeled as a case of supervised learning for multi-class classification, where $C' > 2$.

The deep learning model was entirely implemented with open source tools, namely R² programming language with the Integrated Development Environment RStudio³ using Keras⁴ framework and Tensorflow⁵ engine backend (Chollet and Allaire 2018).

Tensorflow is free and open source library developed by Google for numerical computation using data flow graphs, originally developed for building machine learning and deep learning models. The graphs are composed of nodes (mathematical operations) and edges (the multidimensional data arrays - tensors). communicated between them.

Keras is also free and open source library written in Python⁶, a high-level neural networks API designed to enable fast experimentation with deep neural networks and capable of running on top of TensorFlow.

2 <https://www.r-project.org/>

3 <https://rstudio.com/>

4 <https://keras.rstudio.com/>

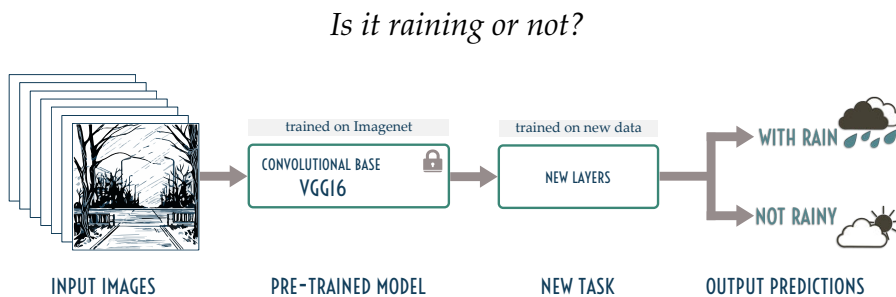
5 <https://tensorflow.rstudio.com/>

6 <https://www.python.org/>

BINARY CLASSIFICATION

It was stated in the previous chapters (Chapter 2, Chapter 3) that the task of detecting rainfall can be achieved through the analysis of the perceptual aspects that determine whether the single photograph in heterogeneous scenes represents a condition of "rain presence" or "rain absence". For obvious reasons the two conditions are mutually exclusive classes.

The first scenario of interest for the proposed study is the rainfall detection, namely a case of supervised learning of binary classification type (Murphy 2012) in single images answering the question:



4.1 DATASET CREATION

The entire dataset used in the different stages of the creation of the CNN model - training, validation and test - was produced on the basis of the essential requirements inherent in the demanded classification task.

The task of the detection of liquid precipitation was modeled as a supervised binary classification in single images. Each input instance was paired with exactly one output label describing the class. The classes created for the dichotomization (according to the presence or absence of visible rainfall) were *With Rain (WR)* and *No Rain (NR)*.

In realistic rainfall detection scenarios, the accessible images are weather degraded and exhibit a large variability of the conditions under which the images have been taken. The dataset was meant to represent unconstrained and verisimilar image settings for designing robust model capable of coping with the variations in the given images. Criteria for building the dataset were as

follows: availability, weather conditions representativeness, the variety of the locations as well as the diversity of the capture time and lightning conditions. Each photograph depicted an outdoor scene; in the case of pictures belonging to the WR group, their visual appearance altered by the rainfall was perceptible by human eye. The pictures with digitally synthesized rain were excluded. In particular, raindrops or streaks were not generated through processing with photo editing software (e.g. Adobe Photoshop, GIMP, etc.) or through other computer graphics techniques, such as 3d modeling or rendering with graphics engines (e.g. Blender, Unity 3D, etc.). To increase the scene heterogeneity and have a sufficiently large and balanced number of instances, different datasets with the mentioned characteristics have been combined.

The first part of the dataset was obtained by selecting the images originally labeled as “sunny” and “rain” in the *Image2Weather* set (Chu et al. 2017), which is a large-scale single images dataset grouped by weather condition and freely available (Figure 4.1). The total number of images in the original set was: 70,501 for sunny class; 45,662 for cloudy class; 1,252 for snowy class; 1,369 for rainy; 357 for foggy class; 64,657 for “other” class (unclear weather conditions). To use as many instances as possible and have two balanced classes, the number of selected images was chosen including all the available rainy pictures: 1,369 for WR group and 1,369 for NR group.



(a) Picture labeled as *rainy*.



(b) Picture labeled as *sunny*.

Figure 4.1: Examples from *Image2Weather* dataset (Chu et al. 2017).

The second source for image collection is a set of pictures taken by dashboard cameras mounted on vehicles moving around Tokyo metropolitan area (Figure 4.2) from 2017.08.19 to 2017.08.20 (©National Research Institute for Earth Science and Disaster Prevention (NIED), Japan).

The ground truth was obtained associating the rainfall rates retrieved from the high precision multi-parameter radar data (Hirano, Maki, et al. 2014; Hirano and Maki 2018) of XRAIN (eXtended RADar Information Network) operated by the Ministry of Land, Infrastructure, Transport and Tourism (MLIT), Japan, to the images according to the capture time and GPS location. The minimum rainfall threshold used for labeling images as belonging to rainy class was $4\text{mm}/h$ (A. Suzuki and T. J. Yamada 2015) for the veracity of the association of the radar data with the position on the ground surface.

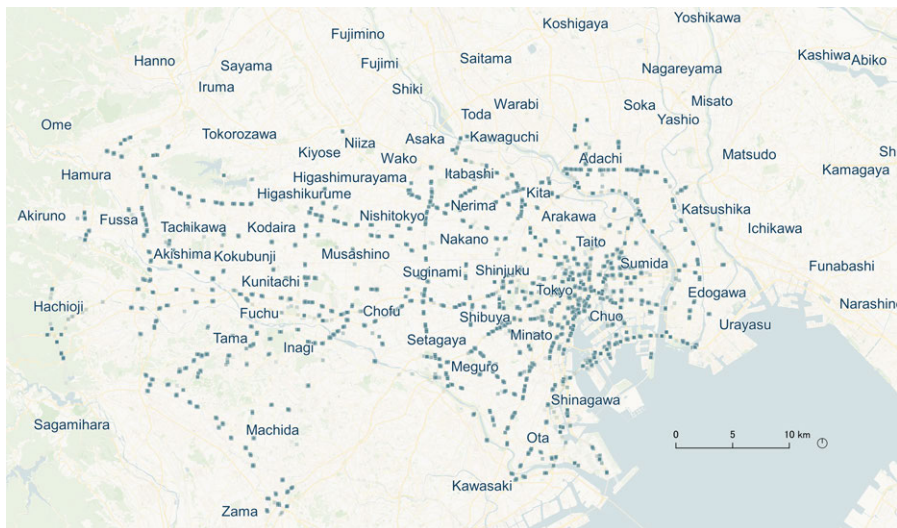


Figure 4.2: Geolocation of the images taken from the dashboard cameras.

Finally, the third tranche of the data was built through experimental activities in the Large-scale Rainfall Simulator of the NIED located in Tsukuba (Ibaraki prefecture, Japan) shown in Figure 4.3. The benefit of using a large scale rain simulator is that it allows experimental tests to be carried out in a relatively short time, reproducing events of different known intensities, including those with a rather remote occurrence frequency, such as rain showers and downpours with high return periods under controlled and repeatable conditions.

This facility for hydro-geological processes simulation and measurement is the largest simulator in the world in terms of

rainfall area (approximately 3000 m^2) and sprinkling capacity. It can produce fairly accurate precipitation fields for rainfall intensities between 15 and 300 mm/h . The nozzles, set up at a height of 16 m above the ground surface, are capable of reproducing the natural rainfall constant speed and generating raindrops with a diameter ranging from 0.1 to 6 mm . An overview of the NIED Large-scale Rainfall Simulator is presented in Appendix B.

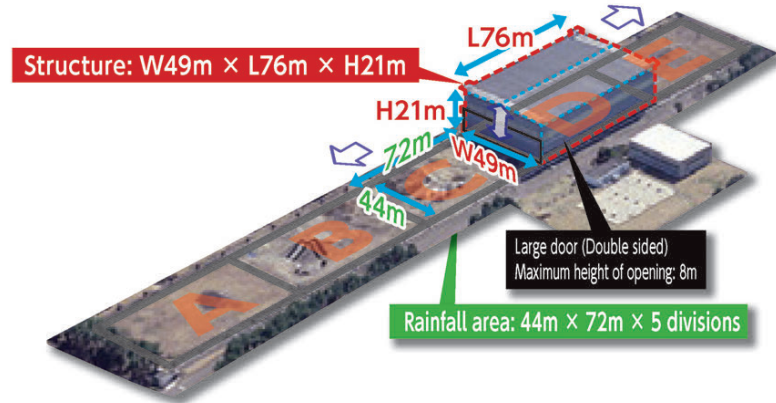
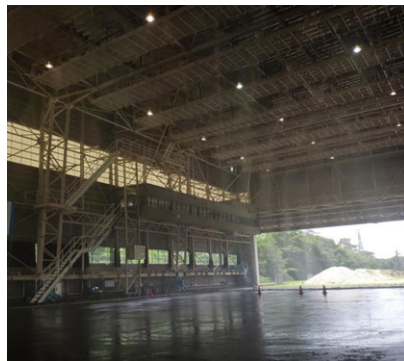


Figure 4.3: NIED Large-scale Rainfall Simulator located in Tsukuba (Ibaraki prefecture, Japan) ©NIED.

During the experiments, the nominal produced intensity ranged from 20 mm/h to 150 mm/h and was assumed as ground truth.

For the purpose of the heterogeneity of the scenes, the photographs (Figure 4.4) were shot with 5 different devices: Canon XC10, Sony DSC-RX10M3, Olympus TG-2, XiaoYI YDXJ 2, XiaoMi MI8 (smartphone).



(a) Picture labeled as *With Rain*.



(b) Picture labeled as *No Rain*.

Figure 4.4: Example of the dataset built during the NIED Large-scale Rainfall Simulator experiments.

The total dataset consisted of 7968 color images (3984 for the class *WR* and 3984 for the class *NR*) coming from the different

devices saved in the JPEG format (pixel resolution ranged from 333×500 up to 5472×3648 pixels).

All the collected images were labeled and organized into the necessary non-overlapping categories (Russell et al. 2010) as shown in Table 4.1: the available data are split into a set for training the model (60% of the total examples), a set for validation (20%) and a set for the test on new data (20%). The training dataset contains the labeled pictures to be used to fit the model. The validation dataset is used to provide an unbiased evaluation of the model goodness of fit during the training steps while tuning the model’s hyperparameters. The test dataset serves to evaluate the generalization ability of the final model, that is to say the accuracy of the predictions on unseen inputs.

The number of instances of the two classes were properly balanced.

LABEL	DATASET	# OF IMAGES			
		(Total)	Train	Validation	Test
WR (presence of rainfall)	Image2weather	1369	823	273	273
	NIED car pictures dataset	1870	1123	374	374
	NIED Rainfall Simulator Experiment (14 June 2019)	744	448	148	148
	Image2weather	1369	823	273	273
WR (absence of rainfall)	NIED car pictures dataset	1870	1123	374	374
	NIED Rainfall Simulator Experiment (14 June 2019)	744	448	148	148
	Image2weather	1369	823	273	273
	NIED car pictures dataset	1870	1123	374	374

Table 4.1: Dataset creation: label division and number of labeled images per dataset

Data augmentation based on basic image manipulations was adopted as a strategy to artificially create new training examples from the existing ones (Shorten and Khoshgoftaar 2019) in order to mitigate overfitting caused by the small number of images, in combination with the other strategies for increasing generalization performance that focus on the model’s architecture itself.

A data-specific design of augmentations guaranteed the safety of the method, the preservation of the labels after the transformations (Shorten and Khoshgoftaar 2019). The random geometric transformations were chosen so as to be isometric and guarantee the physical compatibility with the natural appearance of meteorological phenomena. Other data augmentation methods (e.g. color space transformations, random erasing, mixing images, etc.) were avoided since they compromise the visual effects of the rain in pictures.

The *new* pictures were generated by a mirror-reversal of an original across a vertical axis (horizontal flip or reflection) and/or a 2 degrees angle rotation as shown in Figure 4.5.

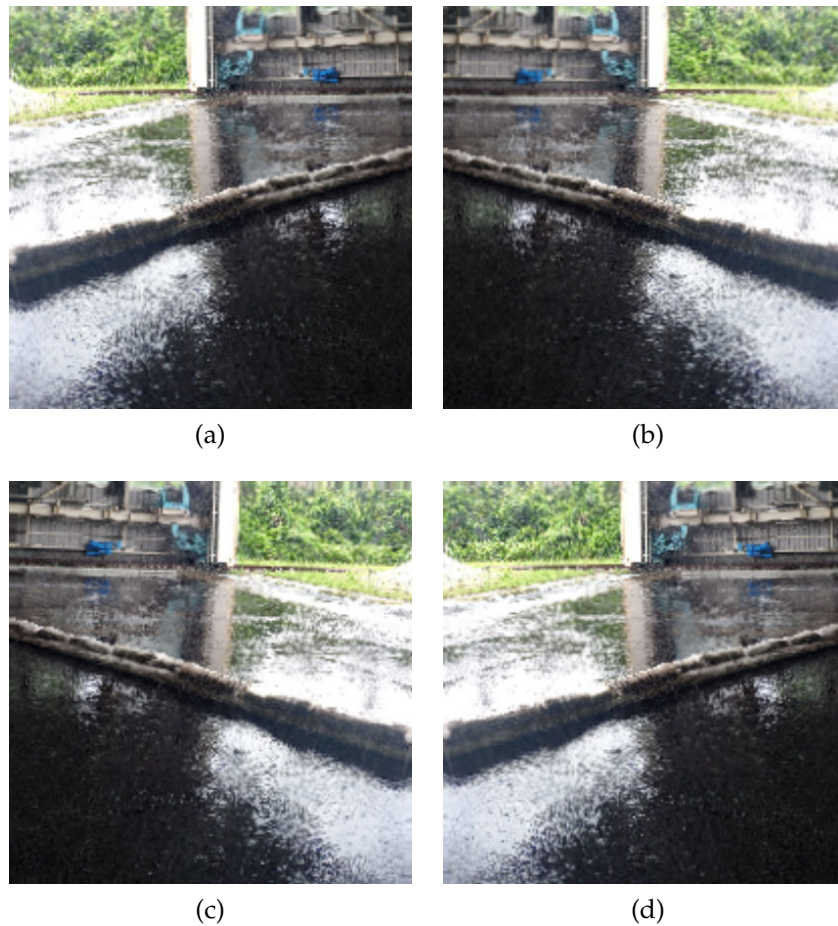


Figure 4.5: Generation of new pictures via random data augmentation.

4.1.1 Model architecture setup

The deep learning model was entirely implemented with open source tools, namely R programming language with the Inte-

grated Development Environment RStudio using Keras framework and Tensorflow engine backend (Chollet and Allaire 2018).

A transfer learning approach was adopted for the extraction of the features, choosing the VGG16 network (Simonyan and Zisserman 2014) as convolutional base because of its characteristics of generality and portability of the learned features, excluding the densely connected classifier on its top as shown in Figure 4.6; the shaded box indicates the components able to learn from the new data.

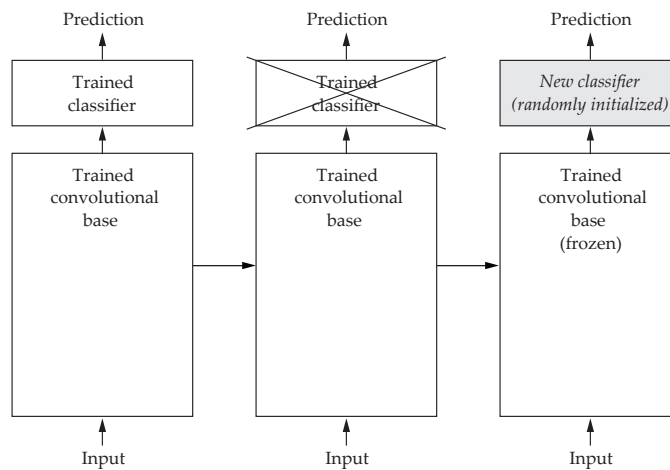


Figure 4.6: Transfer learning approach: feature extraction with Convolutional Base. Reproduced from Chollet and Allaire (2018).

The VGG16 network (Simonyan and Zisserman 2014), proposed by the Visual Geometry Group in the University of Oxford, was trained on 1.4 *million* labeled images of the *ImageNet dataset*¹ and 1,000 different classes (mainly animals and everyday objects) achieving a classification accuracy of 92.7, winning the Large Scale Visual Recognition Challenge 2014 (ILSVRC2014)².

It was retained only the feature extraction part of the model, which includes the layers from the input layer to the last max pooling layer, whereas the rest of the network (the classification part of the model) was discarded.

Since the convolutional base obtained from VGG16 has a considerable number of parameters (14 714 688), the layers were frozen before the compiling and training of the new network.

Freezing was necessary to prevent the weights from being updated during the training of the new network so as to preserve the representations that were previously learned and avoid

1 <http://www.image-net.org/>

2 <http://image-net.org/challenges/LSVRC/2014/results>

overfitting that can result from fine-tuning using a small dataset (Yosinski et al. 2014).

Table 4.2 summarizes the architecture of the convolutional base obtained from the VGG16 network.

LAYER (TYPE)	OUTPUT SHAPE	PARAMETERS #
input_39 (InputLayer)	(None, 200, 200, 3)	0
block1_conv1 (Conv2D)	(None, 200, 200, 64)	1792
block1_conv2 (Conv2D)	(None, 200, 200, 64)	36928
block1_pool (MaxPooling2D)	(None, 100, 100, 64)	0
block2_conv1 (Conv2D)	(None, 100, 100, 128)	73856
block2_conv2 (Conv2D)	(None, 100, 100, 128)	147584
block2_pool (MaxPooling2D)	(None, 50, 50, 128)	0
block3_conv1 (Conv2D)	(None, 50, 50, 256)	295168
block3_conv2 (Conv2D)	(None, 50, 50, 256)	590080
block3_conv3 (Conv2D)	(None, 50, 50, 256)	590080
block3_pool (MaxPooling2D)	(None, 25, 25, 256)	0
block4_conv1 (Conv2D)	(None, 25, 25, 512)	1180160
block4_conv2 (Conv2D)	(None, 25, 25, 512)	2359808
block4_conv3 (Conv2D)	(None, 25, 25, 512)	2359808
block4_pool (MaxPooling2D)	(None, 12, 12, 512)	0
block5_conv1 (Conv2D)	(None, 12, 12, 512)	2359808
block5_conv2 (Conv2D)	(None, 12, 12, 512)	2359808
block5_conv3 (Conv2D)	(None, 12, 12, 512)	2359808
block5_pool (MaxPooling2D)	(None, 6, 6, 512)	0
		Total parameters: 14 714 688

Table 4.2: Convolutional Base architecture

The model was extended by adding new layers on top (Table 4.3), in order to obtain a new classifier capable of generating predictions with the two desired output classes (predict whether the picture represents rainy conditions WR or not NR). The trainable weights are the variables to be included in backpropagation, whereas the non trainable weights (frozen parameters) are not included in backpropagation.

The dropout layer, which randomly drops some input units and their connections with probability $1 - p$, was used as a regularization technique (Goodfellow et al. 2016; Chollet and Allaire 2018; Srivastava et al. 2014) to reduce possible data overfitting problems in the learning phase so as to preserve the algorithm generalizability. The dropout rate was set to 25, meaning one in 4 inputs was randomly excluded from each update cycle during the training phase.

LAYER (TYPE)	OUTPUT SHAPE	PARAMETERS #
vgg16 (Model)	(None, 6, 6, 512)	14714688
flatten (Flatten)	(None, 18432)	0
dense (Dense)	(None, 256)	4718848
dropout (Dropout)	(None, 256)	0
dense_1 (Dense)	(None, 1)	257
Total parameters: 19 433 793 (14 714 688 frozen)		

Table 4.3: Model architecture

Hence, the chosen strategies implemented to mitigate the risk of model overfitting and enhance generalization ability were as follows:

- dataset construction: heterogeneity of acquisition devices, comprehensive assortment of rainfall conditions, pictures depicting the same place exposed to different conditions;
- partitioning of the data into training, validation, and hold-out test sets;
- augmentation of the training data;
- transfer learning with freezing of the convolutional base (feature extraction);
- dropout layer (dropout rate 25);
- low learning rate ($lr = 1 \times 10^{-5}$);
- small batch training (batch size equal to 20);
- stopped training after the model convergence to desirable values of the error (cost function) and the accuracy to avoid overtraining.

4.2 RESULTS AND DISCUSSION

4.2.1 *Training and validation*

The labeled pictures of the training set (Table 4.1) constituted known examples of ordered pairs of input (image) and output (WR or NR class) to feed the network so that the final model can make predictions starting from inputs.

The CNN was initialized with random values of the trainable parameters. Then, the optimizer updated automatically - for each elaborated instance - the weights values implementing the error backpropagation algorithm. The optimization procedure modified the training parameters of the model in order to maximize the prediction accuracy and minimize the cost function, updating the parameters with the gradient multiplied by a learning rate so that the model will perform better. The loss of binary cross entropy between the training data and the model's predictions was used as the cost function (Goodfellow et al. 2016).

A disjoint validation set (Russell et al. 2010, Table 4.1) provided an early unbiased evaluation of the model fit on the training dataset while tuning the hyperparameters of the model, thus preserving its generalization ability.

The training configuration setup can be summarized as follows:

- Data Augmentation: horizontal flip, 2° rotation.
- Loss: binary crossentropy as cost function for monitoring and improving the model skills.
- Optimizer: RMSprop³ implementing the Root Mean Square Propagation (RMSprop) algorithm (Tieleman and Hinton 2012) to update the neural network.
- Metric: accuracy. The amount of correctly classified instances.
- Learning rate: $lr = 1 \times 10^{-5}$.

Figure 4.7 illustrates the predictive effectiveness of the network plotting the trends of the accuracy (*acc*) and loss (*loss*) values over the subsequent iterations for training and for validation, in order to monitor the training stability (constant improvements

³ keras.io/api/optimizers/rmsprop/

without abrupt changes) and the presence of a possible overfitting (graphically identifiable as a divergence between the values calculated on the known data - training - and *unknown* ones - validation).

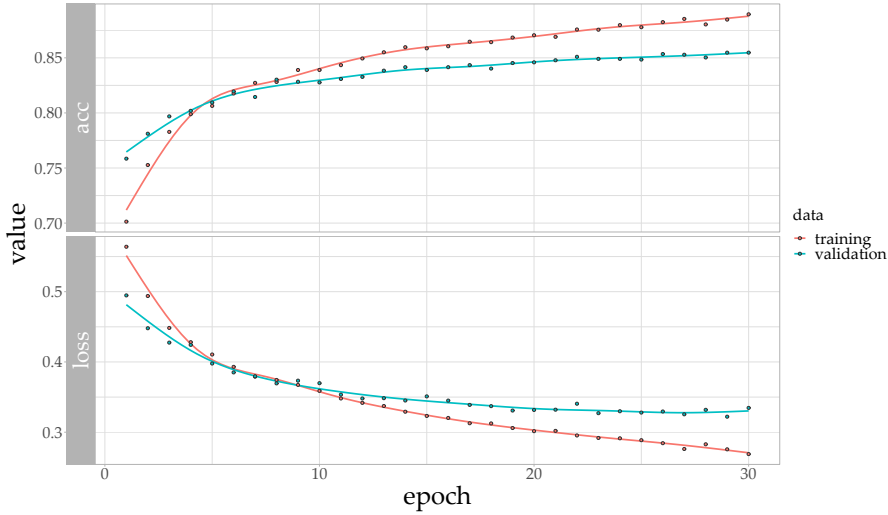


Figure 4.7: Training and validation: overall accuracy and loss values for the binary model

During the 30 epochs - complete presentations of the entire training and validation datasets - the learning rate was set to a fairly low value (1×10^{-5}) to maintain stability (Goodfellow et al. 2016; Bengio 2012). The trained model reached an accuracy of 88.95% on the training set and 85.47% on the validation set (Figure 4.7) and a loss (Murphy 2012) respectively of 0.27 and 0.33

The Loss (Binary Cross Entropy) was calculated as follows:

$$\begin{aligned} \text{Cross Entropy} &= - \sum_{i=1}^{C'=2} t_i \log(f(s_i)) \\ &= -t_1 \log(f(s_1)) - (1 - t_1) \log(1 - f(s_1)) \end{aligned}$$

Where t_i and s_i are respectively the ground-truth and the raw score for each class i in C and

$$f(s_i) = \frac{1}{1 + e^{-s_i}}$$

is the logistic sigmoid activation function which is necessary for the output to be interpreted as a probability.

The case of interest is a binary classification problem: given the input x (picture) we need to predict its output y_i (label), where $y \in \{0, 1\}$ (binary representation of $\{NR, WR\}$) and $i \in \{1, \dots, C'\}$, with $C' = 2$ being the number of classes.

It's assumed that there are two classes: C_1 and C_2 , so $t_1 \in [0, 1]$ and $f(s_1) \in [0, 1]$ are the ground truth and the probability value for C_1 (output label $y_1 = 0$). $t_2 = 1 - t_1$ and $f(s_2) = 1 - f(s_1)$ are the ground truth and the output score for C_2 (output label $y_2 = 1$), as the classes are mutually exclusive.

The values are significantly far from a random prediction in a balanced binary problem.

The random predictor can be metaphorically modeled as a *fair coin* (Murphy 2012; Kerrich 1946), where the tossing is a discrete-time stochastic process that takes only two values (0 or 1) that are mutually exclusive. A single flip of a coin is an event (or trial) that is not connected to or influenced by other events, each of the two outcomes (head or tail, 0 or 1) is equally likely. The likelihood of landing heads up (outcome 0) is 0.5 (50% chance). The same value 0.5 (50% chance) express the probability of landing tail up (outcome 1), since the coin is fair.

Hence, the non-informative values correspond to an accuracy of 50% and loss of 0.69.

4.2.2 Testing and evaluation

In order to evaluate the performance measures of the proposed algorithm, the trained model was applied on the test dataset (holdout dataset) to give an unbiased estimate of model skill (Russell et al. 2010).

The test set of data was disjoint from the training set and the validation set, so it contained examples independent from the data used for the previous steps.

The generalization ability of the model, i.e. how well the algorithm performs on data that it has not seen before, provides useful hints on the reliability of the predictive model deployed in the real world.

In the test phase, predictions were gathered from the final model on the inputs from the test dataset and then compared to the withheld output values.

A random sample of 20 pictures from the test dataset showing predicted class versus actual one on is given in Table 4.4, to allow a manual control on the misclassified instances.

	IMAGE	ACTUAL	PREDICTED	ERROR
1	20170820_00002699.jpg	NR	NR	
2	20170819_00017352.jpg	WR	WR	
3	20170819_00012555.jpg	WR	WR	
4	3543121411.jpg	WR	WR	
5	809423109.jpg	WR	WR	
6	2364621619.jpg	NR	NR	
7	2684425378.jpg	WR	WR	
8	308068832.jpg	NR	NR	
9	20170819_00012315.jpg	WR	WR	
10	C1350611.JPG	WR	WR	
11	20170819_00013587.jpg	WR	WR	
12	20170819_00005405.jpg	NR	NR	
13	20170819_00008640.jpg	NR	NR	
14	IMG_20190614_115340.jpg	WR	WR	
15	IMG_0260.JPG	WR	WR	
16	20170819_00016647.jpg	WR	WR	
17	20170819_00016297.jpg	WR	WR	
18	CAMERA01 (142).jpg	NR	NR	
19	2428240737.jpg	WR	WR	
20	20170819_00001630.jpg	NR	WR	<—

Table 4.4: Predicted classification on a sample of 20 pictures from the test dataset

The test set is independent of the training and validation datasets, but follows the same probability distribution. It contains 1590 unseen examples, 795 for the WR class and 795 for the NR class.

To assess the quality of the predictions on new pictures, the confusion matrix was constructed over the entire test set, as reported in Table 4.5.

Unlike overall accuracy, confusion matrix allows to show a detailed breakdown of correct and incorrect classifications for each class (Zheng 2015). The confusion matrix opposes instances in a predicted class (model response) against instances in an actual class. The correct predictions represented by values in the

diagonal of the matrix while the prediction errors are located outside the diagonal.

		REFERENCE	
		Positive = WR	Negative = NR
PREDICTION	Positive = WR	719 of TP	158 of FP
	Negative = NR	76 of FN	637 of TN

Table 4.5: Confusion matrix for the binary classification problem

Given the WR label (presence of rain) as the positive class and NR (absence of rain) as the negative class, it was counted the number of True Positives (TP), False Positives (FP), True Negatives (TN) and False Negatives (FN) to calculate useful metrics (Goodfellow et al. 2016; Zheng 2015; Murphy 2012; Chicco and Jurman 2020; McHugh 2012).

The accuracy, with a significant p-value (equal to 2×10^{-16}), and the loss of entropy calculated on the test set are respectively 85.28% and 0.34. The accuracy and loss are significantly different from a random prediction and consistent with the metrics obtained in the training and evaluation phase (Section 4.2.1).

In order measure the rain detection performance, several metrics are used and compared to reference values (Goodfellow et al. 2016; Zheng 2015; Murphy 2012; Chicco and Jurman 2020).

$$\text{Overall accuracy} = \frac{(TP + TN)}{(TP + FP + FN + TN)} = 85.25\%$$

Reference values: worst=0%, best=100%.

$$\begin{aligned} \text{Cross Entropy} &= - \sum_{i=1}^{C'=2} t_i \log(s_i) \\ &= -t_1 \log(s_1) - (1 - t_1) \log(1 - s_1) \\ &= 0.3400635 \end{aligned}$$

Reference values: perfect ≈ 0 , good < 0.69 , bad ≥ 0.69 .

$$\text{Sensitivity} - \text{Recall} = \frac{TP}{(TP + FN)} = 90.44\%$$

Reference values: worst=0%, best=100%.

$$Specificity = \frac{TN}{(FP + TN)} = 80.13\%$$

Reference values: worst=0%, best=100%.

$$Precision = \frac{TP}{TP + FP} = 81.98\%$$

Reference values: worst=0%, best=100%.

$$F1 = \frac{(1 + \beta^2) \times precision \times recall}{(\beta^2 \times precision) + recall} = \frac{2 \times precision \times recall}{precision + recall} \\ = 0.8600$$

Reference values: worst=0, best=1.

The β parameter was chosen to determine the weight of recall in the harmonic mean: the recall was considered β (=1) times as important as precision for the combined score.

Kappa value shows good consistency (McHugh 2012):

$$Cohen's\ kappa = \kappa = \frac{p_o - p_e}{1 - p_e} = 1 - \frac{1 - p_o}{1 - p_e} \\ = 0.7057$$

where p_o is the relative observed agreement and p_e is the hypothetical probability of chance agreement (i.e. the accuracy expected by a random classifier, related to the number of instances of each class).

The interpretation of Cohen's kappa values can be summarized as follows(Cohen 1960; McHugh 2012):

- $\kappa \leq 0$ indicates no agreement;
- $0.01 < \kappa < 0.20$ indicates no to slight agreement;
- $0.21 < \kappa < 0.40$ indicates fair agreement;
- $0.41 < \kappa < 0.60$ indicates moderate agreement;
- $0.61 < \kappa < 0.80$ indicates substantial agreement;
- $0.81 < \kappa < 1$ indicates almost perfect agreement.

An effective and reliable metric in binary classifications is the Matthews correlation coefficient (MCC). The MCC value ranges from worst value -1 to best value $+1$ (Chicco and Jurman 2020).

$$\begin{aligned} MCC &= \frac{TP \times TN - FP \times FN}{\sqrt{(TP + FP)(TP + FN)(TN + FP)(TN + FN)}} \\ &= 0.7094 \end{aligned}$$

Taken together, the metrics showed significant outcome. From the results it is evident that the model exhibits good overall predictive reliability.

The sensitivity, $\approx 90\%$, is higher than the specificity, $\approx 80\%$. That means the model is responsive to rainy condition detection but also prone to the risk of reporting false positives. In the application field of interest, i.e. urban flood risk management, high sensitivity is desirable: missing cases of rainfall presence could lead to delays in early warning systems. The detection will easily mark rainy pictures, ensuring that dangerous pluviometric forcing is recognized. On the other hand, the classification was performed on balanced class although in reality a condition of absence of rain is more likely to occur. Hence, specificity is important to avoid unnecessary alerts. The false positive occurrence may be explained by the presence of lens flare caused by sun-rays and artificial lighting which produces artifacts that may resemble to raindrops accumulated on the lens. Closer examination of the results reveals some ambiguity in the visual appearance of the misclassified pictures and hence a limitation of our system: it does not suit scenes that are also misleading for human vision.

The model for rain detection was also tested in a real-world operational setting with completely different novel input images. The results obtained from experiments on the real use case in Matera city are described in the Chapter 6.

The major limitation of the proposed model is intrinsic to the output results: in fact, the detection of the presence of precipitation (without a quantification) is a necessary condition but not sufficient for the creation of a rain gauge network based on cameras. In this regard, in the next chapter, it will be presented another algorithm based on the proposed methodology in order to allow the quantitative characterization of the precipitation forcing. The development of other CNN networks based on the proposed methodology involved several steps: the rainfall inten-

sity was classified into ranges; the dataset was expanded and improved according to criteria of availability of known rainfall intensity values, while the model was properly readapted, fine-tuned, and evaluated to serve the needs of hydro-meteorological monitoring.

As seen in previous chapters, the existing literature for rain measurement from images (Section 2.1.2) strongly relies on acquisition device characteristics and setting and exploits temporal information, as it uses CV techniques based on optics and photographic analyses to retrieve rain drop information to estimate the rainfall intensity.

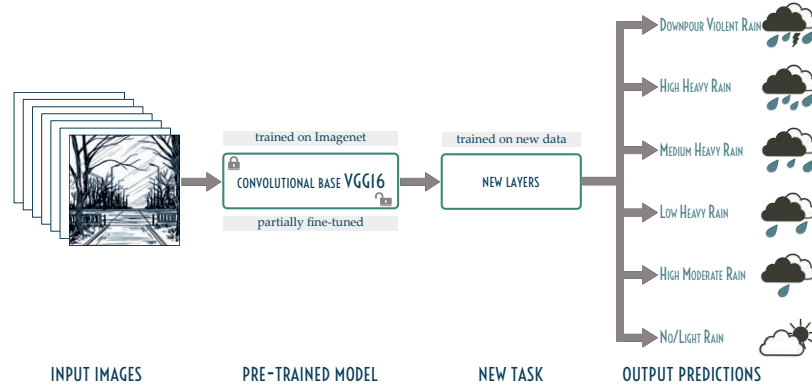
In the previous chapter, a Transfer Learning with CNN approach has proved to be effective for the task of rainfall detection in single images.

In this chapter, the goal is the effective usage of DL techniques to provide an approximated but robust near real time quantitative characterization of the precipitation forcing, through an algorithm based on the same methodology. In comparison with algorithms based on image sequences or video, single-image-based algorithms require to process a lower amount of data and are more robust in urban scenarios where the background contains non-static elements, such as moving pedestrians or vehicles, as they don't depend on background subtraction techniques (Piccardi 2004). The proposed methodology relies on CNN based extraction of global or local key features and identification of classes, focusing more on the rainfall perceptual effects on the raw pictures than on the intrinsic characteristics of the raindrops (shape, size, velocity, density, distribution).

In the context of precipitation-induced disasters early warning systems, the meteorological forcing should be described by suitable threshold values that include duration, spatial extent and intensity (Versace 2017). The duration and space extent can be described by combining the presence of rain (Chapter 4) with temporal and geographical data (i.e. time of capture, location of the camera). The other fundamental quantity that may induce a critical state is the rainfall intensity, so it can be useful to classify it into ranges into non-overlapping ranges that will be the basis for setting up the multi-class image classification. The discretization of the quasi-instantaneous rain intensity values may reduce the effects of minor observational errors; the desired outputs for the model become categorical and not a positive real-valued scalar.

Hence, the second scenario of interest for the study is the rainfall intensity quantification, formalized as a case of supervised learning of multi-class classification type (Murphy 2012) in single images answering the question:

How much is it raining?



5.1 RAINFALL INTENSITY RANGES

The thresholds for defining rainfall intensity classes are challenging to define because a generally accepted definition is lacking, so the values vary considerably from one country to another. A general classification system could be useful to provide a basis for defining critical values for flood triggering considering the local conditions. The critical thresholds depend at a specific scale on the considered watershed characteristics that impact hydrological processes, such as topography, geomorphology, soil properties, land cover, antecedent conditions, and so forth.

The Spanish Meteorological Institute defined rainfall-induced risk scenarios on the basis of the thresholds of average hourly intensity reported in Table 5.1 (Llasat 2001), during the *Plan de Predicción y Vigilancia Meteorológica* PREVIMET specific meteorological surveillance of heavy rains campaign.

INTENSITY RANGE [mm/h]	INTENSITY CLASS
$I \leq 2$	Light rainfall
$2 < I \leq 15$	Moderate rainfall
$15 < I \leq 30$	Heavy rainfall
$30 < I \leq 60$	Very heavy rainfall
$I > 60$	Torrential rainfall

Table 5.1: Thresholds for rainfall intensity classification used by Spanish Meteorological Institute (Llasat 2001).

For synoptic purposes, the United Kingdom Meteorological Office (Met Office, National Meteorological Library and Archive 2005) indicates the thresholds for rainfall intensity classification listed in Table 5.2. In the report, the term *rain* refers to any liquid atmospheric precipitation whose drops are larger than 0.5 mm in diameter (whereas smaller drops, conventionally with diameters between about 200 and 500 μm , are classed as drizzle). The rainfall from a convective cloud (cumulus or cumulonimbus) is described as a *shower* and is distinguished from the precipitation, intermittent or continuous, from layer clouds. Showers often present short duration and rapid fluctuations of intensity.

VARIABLE	INTENSITY RANGE [mm/h]	INTENSITY CLASS
Rain	$I < 0.5$	Slight
(other than showers)	$0.5 \leq I < 4$	Moderate
	$I \geq 4$	Heavy
Rain	$I < 2$	Slight
(showers)	$2 \leq I < 10.0$	Moderate
	$10.0 \leq I < 50$	Heavy
	≥ 50.0	Violent

Table 5.2: Thresholds for rainfall intensity classification used by Met Office, National Meteorological Library and Archive (2005).

In an attempt to establish internationally agreed standards for the generation of data and information on weather, climate and water, the World Meteorological Organization (WMO) regularly publishes an updated version of the *Guide to Meteorological Instruments and Methods of Observation* since 1954. Its purpose is to furnish a comprehensive and up-to-date guidance on the best practices for carrying out meteorological observations and measurements. In the seventh edition of the guide, the World Meteorological Organization (2014) established the *Criteria for light, moderate and heavy precipitation intensity* on the basis of the recommendation by the WMO Expert Meeting on Automation of Visual and Subjective Observations (Trappes/Paris, France, 14–16 May 1997) and the Working Group on Surface Measurements (Geneva, Switzerland, 27–31 August 2001). The light, moderate and heavy precipitation are defined with respect to the type of precipitation and to I intensity values based on a 3 minutes measurement period (Table 5.3).

VARIABLE	INTENSITY RANGE [mm/h]	INTENSITY CLASS
Drizzle	$I < 0.1$	Light
	$0.1 \leq I < 0.5$	Moderate
	$I \geq 0.5$	Heavy
Rain (also showers)	$I < 2.5$	Light
	$2.5 \leq I < 10.0$	Moderate
	$10.0 \leq I < 50$	Heavy
	≥ 50.0	Violent (Intense/Extreme)
Snow	$I < 1.0$ (water equivalent)	Light

Table 5.3: Thresholds for precipitation intensity classification used by World Meteorological Organization (2014).

Table 5.4 discloses the rainfall intensity classification by Japan Meteorological Agency (2017) used in messages for severe weather preparedness (emergencies warnings, warnings, advisories and bulletin systems). The messages are issued by Local Meteorological Offices to their respective prefectures and disseminated to the public through administrative organs and a wide variety of media, blending technical details and more user-friendly provision of meteorological information.

INTENSITY RANGE [mm/h]	INTENSITY CLASS	
$10 \leq I < 20$	Slightly heavy rain	やや強い雨
$20 \leq I < 30$	Heavy rain	強い雨
$30 \leq I < 50$	Intense rain	激しい雨
$50 \leq I < 80$	Very intense rain	非常に激しい雨
$I \geq 80$	Torrential rain	猛烈な雨

Table 5.4: Thresholds for rainfall intensity classification used by Japan Meteorological Agency (2017).

To enable the users to understand and use correctly the weather information, each class is clearly described with different perceptual aspects, direct effects on people, indoor effects, outdoor effects, effects when driving in a car. A pictorial illustration associated with each aspect allows users to quickly gain an empiric understanding of the rain intensity (Figure 5.1). Although being a well-developed method, there are still gaps between the transmission and reception of information on rainfall amounts,

expressed either as a quantitative value or using qualitative language (Shimazaki et al. 2018).

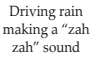
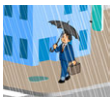
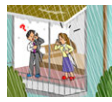



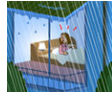
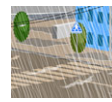

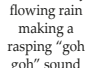
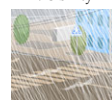

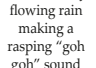
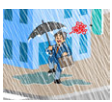
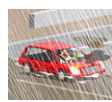
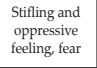
HOURLY PRECIPITATION [mm/h] INTENSITY CLASS	IMAGE THAT PEOPLE PERCEIVE	INFLUENCE ON PEOPLE	INDOOR (wooden houses)	OUTDOOR	WHEN RIDING A CAR
10 ≤ I < 20 Slightly heavy rain		The rain bounces from the ground and wets the feet 	The sound of rain covers the voices 	Rain puddles form anywhere on the ground 	
20 ≤ I < 30 Heavy rain		People get wet even when using an umbrella 	Approximately half of sleeping people can notice the rain 	Roads are turned into rivers 	Low visibility even with high windshield wiper speeds 
30 ≤ I < 50 Intense rain	Rainfall like poured from a bucket 			Water splashing whitens the surroundings and reduces visibility 	When driving at high speed, a layer of water builds between the vehicle wheels and the road surface, leading to a loss of controllability and braking efficiency (aquaplaning phenomenon) 
50 ≤ I < 80 Very intense rain	Continuously flowing rain making a rasping "goh goh" sound 	Umbrellas are totally useless 			Driving a car is dangerous 
I ≥ 80 Torrential rain	Stifling and oppressive feeling, fear 				

Figure 5.1: Informative rainfall intensity classification. Translated and adapted from Japan Meteorological Agency (2017).

In contrast to the aforementioned classification systems, the China Meteorological Administration rainfall classification reported by Miao et al. (2018) refers to daily precipitation (Table 5.5).

24 HOUR RAINFALL TOTAL [mm]	CLASS
0	No rain
0.1 – 2.15	Light to moderate rain
25 – 50	Heavy rain
50 – 75	Torrential rain
75 – 100	Heavy torrential rain
≥ 100	Downpour

Table 5.5: Thresholds for rainfall classification used by China Meteorological Administration (Miao et al. 2018).

However, a classification based on the rainfall total within 24 hours does not appear to be especially suitable for the purposes of the present study.

5.2 DATA SOURCES

Both the dataset used for the binary classification in Chapter 4 and the dataset chosen for the multi-class classification share a number of key characteristics inherent in the classification task in single images. In both cases, the dataset was representative with respect to realistic scenarios with unconstrained and verisimilar image settings, where the pictures are weather degraded and exhibit a large variability. The quality of the dataset affects the model robustness and the capability of coping with the variations in the given images.

The detection of liquid precipitation was a case of supervised learning of binary classification type (Murphy 2012), so the examples were composed of input instances x and the output labels $y \in \{NR, WR\}$ (binary representation $y \in \{0, 1\}$) according to the presence or absence of visible rainfall.

By contrast, for the quantitative characterization of rainfall the input images x must be labeled with the outputs y_i , where $i \in \{1, \dots, C'\}$, with $C' > 2$ being the number of classes. Each label y_i indicates a class C_i corresponding to the considered rainfall conditions, i.e. categories formed by ranges of rain rates, used to classify rainfall average intensity over given periods of time (Monjo 2016).

The dataset used in the Chapter 4 was expanded in terms of number of instances and improved according to criteria of availability of known rainfall intensity values, while the model was properly re-adapted, fine-tuned, and evaluated to meet the needs of hydro-meteorological monitoring. A larger dataset might ensure adequate representation of different rainfall levels and capturing conditions.

Criteria for inclusion were as follows: outdoor scene depiction, known value of rainfall intensity, availability, multiple rainfall conditions representativeness, diversity of acquisition devices, variety of the locations, heterogeneity of the capture time and lightning conditions.

The pictures with digitally synthesized raindrops or streaks (i.e. generated with photo editing, 3d modeling and rendering software) were excluded due to the difficulties of simulating rain

intensity values with verisimilar physical-perceptual appearance (Duthon et al. 2016).

The picture belonging to *Image2Weather* set (Chu et al. 2017), which were used for the binary classification (Chapter 4), did not meet inclusion criteria for the study due to the lack of rainfall rate information as the images originally were labeled as “sunny” and “rain”.

The first part of the dataset corresponds with the set of pictures taken by dashboard cameras mounted on vehicles moving around Tokyo Metropolitan Area (Figure 4.2) from 2017.08.19 to 2017.08.20 (©NIED, Japan), already used in the binary case.

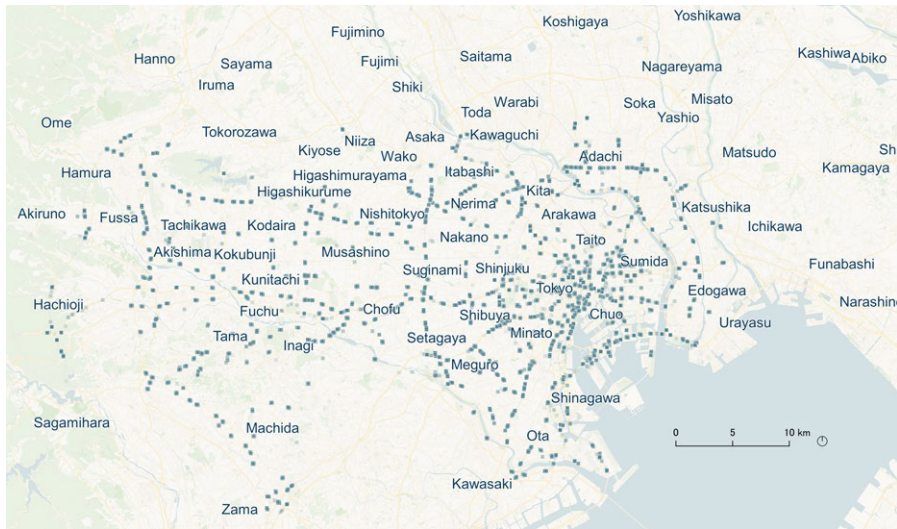


Figure 5.2: Geolocation of the images taken from the dashboard cameras around Tokyo Metropolitan Area.

The onboard cameras collect pictures by recording the view through a vehicle’s front windscreen. Hence, to increase the possibilities of capturing different precipitation conditions, the geographical area and the time span for the dash-cam image collection were expanded to seasons and areas where rain is expected to be frequent. Japan is characterized by four distinct seasons and its climate ranges from subarctic in the north to subtropical in the south; Honshu, Shikoku and Kyushu Regions have hot or very hot and humid summers (Peel et al. 2007; *Japan Meteorological Agency | Climate of Japan* n.d.).

The second collection of dashboard camera pictures were taken from moving vehicles in several Japanese prefectures (Figure 5.3) for almost a year, from 2017.07.08 to 2018.06.19 (©NIED).

In both sets, the ground truth for each photography was obtained associating the rainfall rate retrieved from the high pre-

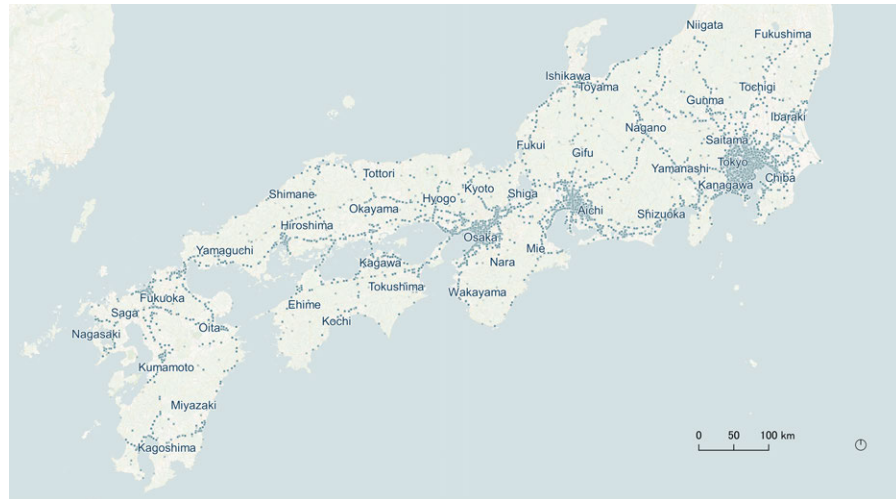


Figure 5.3: Geolocation of the images taken from the dashboard cameras in different Japanese Prefectures.

cision multi-parameter radar XRAIN (Hirano, Maki, et al. 2014; Hirano and Maki 2018) to the image according to the capture time and GPS location. For the veracity of the association of the radar data with the position on the ground surface, the minimum rainfall threshold used for labeling was 5 mm/h .

The data obtained previously through experimental activities in the NIED Large-scale Rainfall Simulator located in Tsukuba (Appendix B), were inflated with further experiments using the same heterogeneous shooting devices (Figure 5.4): Canon XC10, Sony DSC-RX10M3, Olympus TG-2, XiaoYI YDXJ 2, XiaoMi MI8 (smartphone).

The Large-scale Rainfall Simulator (Appendix B) experiments simulated fairly accurate precipitation fields for given rainfall intensities in a controlled and repeatable way within areas reproducing different outdoor landscapes and surfaces, such as asphalt or grass. By using the physical simulation it shall be ensured the inclusion of a comprehensive assortment of rainfall conditions, including the extreme rain events that usually have a rather remote occurrence frequency, such as rain showers and downpours with high return periods. A major advantage of physical simulation is that delivers raindrops of similar size and velocity as natural rainfall partially solving the problem of waiting for a natural event to occur to collect data.



Figure 5.4: NIED Large-scale Rainfall Simulator experiments.

As previously stated, the training dataset should allow an adequate generalization, which means that the CNN should be capable of learning meaningful image features that would enable the extension to new datasets and therefore the model deployment for prediction using novel images. To achieve this, the dataset should include images where the same place is exposed to different conditions, including the absence of precipitation so as to avoid misinterpretation of part of the background as “rainy features”. Hence, the photos taken in the Simulator comprised scenes where the nozzles were turned off and no precipitation was produced. Before the experiments the scenes depicted dry surfaces, after the experiments the surfaces were wet and some puddles accumulated on the ground, creating realistic scenarios.

During the experiments in the simulator, the nominal constant intensity produced by the nozzles was set to the following values: 0 mm/h (before or after the rain simulations); 20 mm/h (the minimum amount that can be set to obtain an accurate precipitation field); 30 mm/h ; 40 mm/h ; 50 mm/h ; 60 mm/h ; 70 mm/h ; 80 mm/h ; 90 mm/h ; 100 mm/h ; and 150 mm/h for a certain time frame.

The minimum scheduled time span was 15 minutes and the maximum was 60 minutes , to ensure the stability of the rainfall rate produced. The intervals of shift from a given intensity to the subsequent one were not considered part of the experiment to avoid uncertainty.

The produced intensity was assumed as ground truth for image labeling. The nominal rain intensity was confirmed by averaging the measurements that were taken each 30 seconds by different rain gauges during each experiment (Figure 5.5).



Figure 5.5: Rain gauges used for checking nominal rain intensity.

The final data set included 61519 heterogeneous color images coming from the different devices (dashboard moving cameras, smartphone, action cam, digital cameras) mentioned previously.

The collected images were saved in the JPEG format. Coming from disparate sources, pictures have various pixel resolutions ranging from 333×500 up to 5472×3648 pixels.

Each picture was associated with its respective known value of rainfall rate assumed as ground truth (nominal produced intensity for the pictures gathered during the experimental activities,

XRAIN data for the dashboard camera pictures). In the resulting dataset the quantity of images with a precipitation intensity $0 \leq I \leq 10$ slightly outnumbered the other ones as a condition of absence of rain or rain intensity lower than 10 mm/h was more frequent in the dash-cam pictures. An over-compensation with the data coming from NIED Large-scale Rainfall Simulator could have affected the representational capacity of the deep CNN and increased the gap in the portion of images associated with a precipitation intensity $10 < I < 20$.

An important thing to bear in mind when training a Neural Network is the number of training instances. Large data results in better generalization. Large-scale data is a commonly-used notion in ML and yet it is a concept difficult to quantify precisely. Commonly used large-scale CV datasets¹ contain millions of pictures. In this case the number of available examples is about 8 times larger than the amount used for the binary classification in Chapter 4, but neither datasets can generally be defined as large-scale datasets.

None of the large scale public dataset available could satisfy the requirements inherent in the task of interest, i.e. images that depict natural rainfall with a given intensity, so it was not possible to integrate further images.

The chosen strategy to address the problem of limited data was data augmentation to artificially increase the number of exposed instances, creating more data with stochastic changes that don't impact the interpretation of the images. A data-specific design of augmentations ensures the safety of the method, i.e. the likelihood of preserving the label post-transformation. This data-space solution helps to mitigate overfitting (Shorten and Khoshgoftaar 2019), in combination with the other regularization strategies focusing on the model's architecture itself.

Image data augmentation is extremely useful to improve the robustness of the network, but can be a computationally expensive and time-consuming process. Geometric transformations suffer from the following drawbacks: additional memory, transformation compute costs, and additional training time (Shorten and Khoshgoftaar 2019).

To obtain a good compromise between computational time and a sufficiently large number of training instances, the chosen geometrical transformation for image data augmentation was restrained to the horizontal flip. Horizontal flip or reflection is a mirror-reversal of an original picture across a vertical axis pas-

1 <https://www.datasetlist.com/>

ing through its center. As can be clearly seen in Figure 5.6, it doesn't affect the natural appearance of the precipitation for obvious reasons. avoided since they compromise the visual effects of the rain in the pictures.



(a) Original Image



(b) Flipped image

Figure 5.6: Generation of new pictures via random data augmentation.

5.3 MODEL ARCHITECTURE SETUP

The CNN model architecture setup is similar to that used in the previous case.

The DL model was implemented using open source tools: R programming language with the Integrated Development En-

vironment RStudio, Keras framework, and Tensorflow engine backend (Chollet and Allaire 2018).

Transfer learning methods offer an effective way of overcoming the difficulties of training very deep architectures due to the non-triviality of the addressed task and the limited supply of available training data (Pan and Q. Yang 2010; Yosinski et al. 2014; Weiss et al. 2016).

The transfer learning approach was applied using the VGG16 network (Simonyan and Zisserman 2014) for the convolutional base (Table 5.6) excluding the full connected layers of its original architecture (Figure 5.7). As seen in Section 4.1.1 the main advantages of the VGG16 are its generality and the portability of the features learned on the standard, large-scale, high-quality computer vision benchmark dataset *ImageNet*².

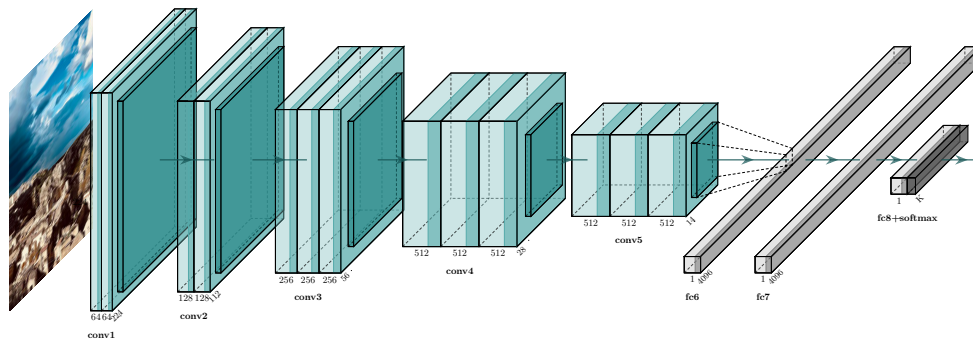


Figure 5.7: VGG16 model architecture.

Given the numerousness of parameters in the VGG16 network, it was partially frozen before the compiling and training of the new network. The first-layers of a deep network trained on natural images learn *general* features resembling Gabor filters or color blob that work as generic semantic representations of the visual world also for novel perceptual problems (Yosinski et al. 2014; Chollet and Allaire 2018). Such layers were frozen to prevent the weights from being updated during the training of the new network so as to preserve the previous knowledge and avoid overfitting on the novel smaller dataset (Yosinski et al. 2014). The last convolutional layer (*block5_conv3*) was unfrozen to allow fine-tuning (weights updating during the training) as it contains features that can be considered more *specific* (Yosinski et al. 2014) to the task and data-related. This was found to be a necessary component in developing the new network because the ImageNet database contains pictures representing mostly animals,

² <http://www.image-net.org/>

plants, food, and everyday objects that are not directly related to meteorological conditions or outdoor scenes. Freezing layer and fine-tuning approaches were combined to obtain a good trade-off between the computational time, the goodness of fit, and the accuracy.

LAYER (TYPE)	OUTPUT SHAPE	PARAMETERS #
input_39 (InputLayer)	(None, 200, 200, 3)	0
block1_conv1 (Conv2D)	(None, 200, 200, 64)	1792
block1_conv2 (Conv2D)	(None, 200, 200, 64)	36928
block1_pool (MaxPooling2D)	(None, 100, 100, 64)	0
block2_conv1 (Conv2D)	(None, 100, 100, 128)	73856
block2_conv2 (Conv2D)	(None, 100, 100, 128)	147584
block2_pool (MaxPooling2D)	(None, 50, 50, 128)	0
block3_conv1 (Conv2D)	(None, 50, 50, 256)	295168
block3_conv2 (Conv2D)	(None, 50, 50, 256)	590080
block3_conv3 (Conv2D)	(None, 50, 50, 256)	590080
block3_pool (MaxPooling2D)	(None, 25, 25, 256)	0
block4_conv1 (Conv2D)	(None, 25, 25, 512)	1180160
block4_conv2 (Conv2D)	(None, 25, 25, 512)	2359808
block4_conv3 (Conv2D)	(None, 25, 25, 512)	2359808
block4_pool (MaxPooling2D)	(None, 12, 12, 512)	0
block5_conv1 (Conv2D)	(None, 12, 12, 512)	2359808
block5_conv2 (Conv2D)	(None, 12, 12, 512)	2359808
block5_conv3 (Conv2D)	(None, 12, 12, 512)	2359808
block5_pool (MaxPooling2D)	(None, 6, 6, 512)	0
		Total parameters: 14 714 688

Table 5.6: Convolutional Base architecture

The model was extended by adding new layers on top (Table 5.7), to obtain a new classifier for the addressed classification task.

The number of total parameters of the network is equal to 18 402 494. 6 047 614 trainable weights were the variables included in backpropagation, whereas the 12 354 880 frozen parameters were excluded from the training.

The dropout layer randomly drops some input units (along with their connections) from the neural network during train-

ing with probability $1 - p$. This prevents units from co-adapting excessively. It was used as a regularization technique to reduce the risk of data overfitting so as to preserve the algorithm generalizability (Goodfellow et al. 2016; Chollet and Allaire 2018; Srivastava et al. 2014). The dropout rate was set to 20%, meaning one in 5 inputs was randomly excluded from each update cycle during the training phase.

LAYER (TYPE)	OUTPUT SHAPE	PARAMETERS #
vgg16 (Model)	(None, 6, 6, 512)	14714688
flatten (Flatten)	(None, 18432)	0
dense (Dense)	(None, 200)	3686600
dropout (Dropout)	(None, 200)	0
dense_1 (Dense)	(None, C')	1206
Total parameters: 18 402 494 (12 354 880 frozen)		

Table 5.7: Model architecture

The task of interest is a C' -way classification, so the last layer had C' outputs and a softmax activation to return an array of C' probability scores (summing to 1). Each score represents the probability that the image exposed to the classifier belongs to one of the classes C_i , where $i \in \{1, \dots, C'\}$ with $C' > 2$ being the number of classes.

5.3.1 Training and validation setup

The process of training involves providing to the learning algorithm with known examples of ordered pairs of input and output to feed the network. Each training instances consisted of an input picture x paired with exactly one output label y_i corresponding to the considered rainfall conditions. The aim is obtaining a final fitted model that can make accurate predictions starting from novel unseen inputs taking as input a picture x and generating predictions of the classes C_i , giving as output a predicted label \hat{y}_i^3 where $i \in \{1, \dots, C'\}$, with C' being the number of classes, that is to say to predict what rainfall intensity range is photographed.

Two different binning set-ups were used according to the purpose of study: a $C' = 6$ classification and a $C' = 5$ classification. This process is described in more detail in the next section.

³ The hat is used to denote an estimated value.

During the training phase, the CNN was initialized with random values of all the trainable parameters. For each example exposed to the model, the RMSprop optimizer updated automatically the values of the weights implementing the error back-propagation algorithm. The parameters were modified through the optimization procedure so as to maximize the prediction accuracy and minimize the cost function. The loss of categorical cross entropy between the training data and the model's predictions was used as the cost function because the model aimed to perform a multi-class classification: images are classified into multiple mutually exclusive classes (Goodfellow et al. 2016; Chollet and Allaire 2018).

A disjoint validation set (Russell et al. 2010, Table 4.1) provided an early unbiased evaluation of the model fitness while tuning the model's hyperparameters (Figure 4.7), thus safeguarding its generalization ability.

The Loss (Binary Cross Entropy) was calculated as follows:

$$\text{Cross Entropy} = - \sum_{i=1}^{C'} t_i \log(f(\mathbf{s})_i)$$

Where t_i is the ground-truth for each class C_i and

$$f(\mathbf{s})_i = \frac{e^{s_i}}{\sum_j^C e^{s_j}}$$

is the softmax activation function appended to the last layer. The activation function is necessary to normalize the outputs of the neural network (raw scores) to a probability distribution over predicted output classes.

Prior to softmax activation, the component of the vector \mathbf{s} , the raw scores inferred by the net, can assume any values in \mathbb{R} and might not sum to 1. The numeric outputs of the last linear layer of the multi-class classification neural network (logits) need to be turned into probabilities. After applying softmax, all the components $\in [0, 1]$ and sum to 1. The softmax function takes as input the vector \mathbf{s} of C' real numbers, and normalizes it into a probability distribution consisting of C' probabilities proportional to the exponentials of the input numbers. As elements represent a class, they can be interpreted as class probabilities.

For training and validation, the deep network completed 30 epochs, i.e. complete presentations of the entire training and

validation datasets. Each epoch required several iterations to accomplish one forward pass and one backward pass of all the examples as they were parsed into batch size equal to 20. The use of a small batch guarantees a significantly smaller memory footprint and may offer a regularizing effect resulting in lower generalization error (Bengio 2012; Masters and Luschi 2018).

The learning rate controls the size of the step an optimizer takes towards the minima of the loss function. The chosen adaptive learning rate technique, implemented through the Keras callback *ReduceLROnPlateau*, was set to reduce the learning rate by a 0.1 factor when the optimizer cannot improve the results over 5 epochs (*patience* number of epochs). This situation means that the optimizer has reached a *plateau* (Goodfellow et al. 2016), and it needs the step size to be reduced in order to move down the error towards the new minima. Hence, if the target training metric (namely the loss) had stopped improving and stagnated over 5 epochs, the learning rate was adjusted. Since the procedure was repeated over the epochs, the learning rate was reduced only when needed, giving the optimizer enough time to find a better path towards the minima.

The implemented strategies to prevent overfitting can therefore be resumed as follows:

- dataset construction: heterogeneity of acquisition devices, a comprehensive assortment of rainfall conditions, pictures depicting the same place exposed to different conditions;
- partitioning of the data training, validation, and holdout test sets;
- augmentation of the training data;
- transfer learning with partial freezing of the convolutional base;
- dropout layer (dropout rate 20%);
- adaptive learning rate;
- small batch training (batch size equal to 20);
- stopped training after the model convergence to adequate values of the error (cost function) and the accuracy.

5.4 6 CLASS CLASSIFICATION

The total data set consisted of 61519 color images acquired from the different devices saved in the JPEG format (pixel resolution ranged from 333×500 up to 5472×3648 *pixels*).

The images were labeled according to the associated rainfall intensities, whose values were binned into six ranges.

Combining the thresholds arranged by World Meteorological Organization (2014) and by Japan Metereological Agency (2017), the rain rate categories were defined as non-overlapping classes: No Rain or Light rain (NLR), High Moderate rain (HMR), Low Heavy Rain (LHR), Medium Heavy Rain (MHR), High Heavy Rain (HHR), and Violent Rain, Downpour (DVR), using the ranges given in Table 5.8.

The available data were divided into the non-intersecting subsets needed (Russell et al. 2010) as listed in Table 5.8. For each class C_i , where $i \in \{1, \dots, 6\}$, about 60% of the total examples was chosen randomly for training the model, 20% for validation and 20% for the test on novel instances.

LABEL	INTENSITY RANGE [<i>mm/h</i>]	# OF IMAGES			
		(Total)	Train	Validation	Test
NLR - No rain or Light Rain	< 5	10278	6026	2126	2126
HMR - High Moderate Rain	$5 \leq I < 10$	15551	8742	3406	3403
LHR - Low Heavy Rain	$10 \leq I < 20$	5919	3294	1308	1317
MHR - Medium Heavy Rain	$20 \leq I < 30$	7820	4520	1648	1652
HHR - High Heavy Rain	$30 \leq I < 50$	7818	4716	1661	1441
DVR - Violent Rain, Downpour	$I \geq 50$	8214	4914	1650	1650

Table 5.8: Data set creation: label division and number of labeled images per data set

The obtained dataset did not have exactly equal number of instances in each class. The classes were slightly imbalanced. Although could be useful for generating a balanced distribution of

all classes, undersampling strategies involve removal of some of the data and may generate gaps. Furthermore, in the considered real world scenarios a condition of absence of rain or rain intensity lower than 10 mm/h is more likely to occur. It is reasonable to expect that the influence of this mild imbalance is negligible (Google Developers n.d.). For the sake of data completeness, all available examples were used.

In order to enlarge the size of the training set, new instances were created via data augmentation (Shorten and Khoshgoftaar 2019). This helps prevent overfitting enhancing the model generalization ability, together with the other strategies addressing the model architecture. The *new* examples were obtained through a mirror-reversal of the original pictures x across a vertical axis as shown in Figure 4.5, retaining the associated label y_i . The chosen transformation is isometric and guarantees the physical compatibility with the natural appearance of meteorological phenomena and the background elements of the scene portrayed (urban environments, vehicles, people, road, grass surface, and so on).

5.4.1 Results and discussion

5.4.1.1 Training and validation

The setup previously described in Section 5.3 has been used for the process of training and validation on a holdout set generated from the original total data (Table 5.8).

The set training configuration (Section 5.3.1) can be summarized as follows:

- Data Augmentation: horizontal flip.
- Loss: categorical cross-entropy. It was used as the cost function to map the network performance and improve the preparation of the model.
- Optimizer: RMSprop⁴. This optimizer implementing the RMSprop algorithm (Tieleman and Hinton 2012) is the mechanism through which the network update itself.
- Metric: accuracy. The fraction of the images that were correctly classified was the metric monitored during training and testing.

⁴ keras.io/api/optimizers/rmsprop/

- Adaptive learning rate: ReduceLROnPlateau⁵.

Figure 5.8 plots the accuracy (*acc*) and loss (*loss*) curves respectively in the top and the bottom panel for validation and training by epoch.

After an essentially improving trend with some fluctuation (they seem to peak around the 10th epoch) in the very first epochs due to a random initialization of the network and the number of the classes, the training and validation loss values decreased over the epochs, and the accuracy values increased over the epochs.

As seen in the plot, the values stopped improving significantly after 20 epochs. In the subsequent epochs, the accuracy values stopped to significantly improve: the training accuracy stalled at 80% – 81% , whereas the validation accuracy stalled at 78%. The training and validation loss values were not decreasing significantly at the 21st epoch.

The model shows comparable skills on on both datasets: the visible plateau and the absence of abrupt changes in the curves indicates that the network has converged and the absence of inflection for validation curves indicates the absence of over-learning of the training data.

The trends over the subsequent iterations for training and for validation identified a good model fit: the curves tended to reach a point of stability with a minimal gap between the final values relative to the two sets.

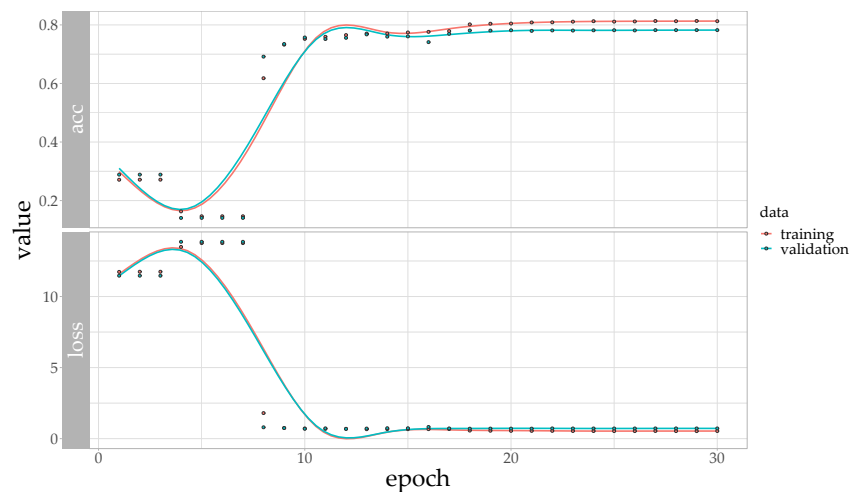


Figure 5.8: Training and validation: overall accuracy and loss values for the 6 class model.

⁵ keras.io/api/callbacks/reduce_lr_on_plateau

The model was stopped after 30 epochs because the continued training of a good fit may likely lead to an overfit, learning representations that are specific to the training data and don't generalize to data outside of the training set.

After the 30 training epochs, the network reached an overall accuracy of 81.27% on the training set and 78.22% on the validation set (Figure 5.8) and a loss (Murphy 2012) respectively of 0.54 and 0.72.

The Loss (Binary Cross Entropy) was calculated as follows:

$$\text{Cross Entropy} = - \sum_{i=1}^{C'=6} t_i \log(f(\mathbf{s})_i)$$

Where t_i is the ground-truth for each class C_i and

$$f(\mathbf{s})_i = \frac{e^{s_i}}{\sum_j^C e^{s_j}}$$

is the last layer softmax activation function.

The case of interest is a 6-way classification problem: given the input x (picture) we need to predict its output y_i (label), relative to the C_i class where $i \in \{1, \dots, C'\}$, with $C' = 6$ being the number of classes. Interpreting the activated score as a probability distribution, the predicted class label corresponds to the maximum activated score among all classes.

The values obtained by the final model are significantly far from a random prediction considering the accuracy and loss of a balanced 6-class classification problem, where the non-informative values correspond to accuracy of 16,67% and loss of 1.79.

5.4.1.2 *Testing and evaluation*

To obtain an independent evaluation of the algorithm predictive skills, a test set was exposed to the trained model. The test set (holdout set) was locked away completely during the training and evaluation steps, to avoid "peeking" (Russell et al. 2010). The test set contained 11625 examples randomly chosen from the total dataset that were not seen by the network in the previous step, following the same probability class distribution. Hence it was used to assess the generalization ability of the model to test the reliability of the model deployment on new use scenarios.

During the test phase, the final model generated output predictions on the unseen inputs images to be compared to the withheld output labels.

The overall accuracy was calculated on the test set, measuring the fraction of the total samples that were correctly classified.

The obtained value 77.71% was significantly higher from a random 6 class classifier prediction accuracy and coherent with the values obtained in the training and evaluation steps (Section 5.4.1.1), the 95% confidence interval was of 0.7639 and 0.7793, so there is a 95% likelihood that the actual accuracy for the model lies within this range.

$$\text{Overall accuracy} = \frac{\text{correct predictions}}{\text{total predictions}} = 77.17\%$$

Reference values: worst=0%, best=100%.

The “no-information rate” was the largest proportion of the observed classes: the C_2 class HMR, *No Information Rate* = 0.29. This value represents the accuracy achievable by always predicting the majority class C_2 label $y_2 = HMR$.

It was also computed a hypothesis test to verify whether the overall accuracy rate was greater than the rate of the largest class, obtaining a significant p-value (equal to 2.2×10^{-16}).

Kappa value, calculated as the classification accuracy normalized by the imbalance of the classes in the data, indicates a good reliability:

$$\begin{aligned} \text{Cohen's kappa} = \kappa &= \frac{p_o - p_e}{1 - p_e} = 1 - \frac{1 - p_o}{1 - p_e} \\ &= 0.7095 \end{aligned}$$

where p_o is the relative observed agreement and p_e is the hypothetical probability of chance agreement (namely the accuracy expected by a random classifier, calculated with respect to the number of instances of each of the 6 classes).

The interpretation of Cohen’s kappa values can be summarized as follows (Cohen 1960; McHugh 2012):

- $\kappa \leq 0$ indicates no agreement;
- $0.01 < \kappa < 0.20$ indicates no to slight agreement;
- $0.21 < \kappa < 0.40$ indicates fair agreement;
- $0.41 < \kappa < 0.60$ indicates moderate agreement;

- $0.61 < \kappa < 0.80$ indicates substantial agreement;
- $0.81 < \kappa < 1$ indicates almost perfect agreement.

The overall statistics indicate that the obtained classification is significantly better than random predictions.

To compare the relationship between known reference data (ground truth) and the corresponding results of the classification it was built an error matrix compare on a class-by-class basis.

Table 5.9 shows the confusion matrix of rainfall type 6-way classification, where columns represent the true labels of the instances, whereas rows represent the estimated labels. The elements of the diagonal represent the number of correctly predicted instances. The off-diagonal elements report the count of misclassified elements, which are the examples belonging to a class that are mistakenly associated with another class. The shades of gray indicate the percentage of the test elements in the given class. These results are generally very promising. The worse performance can be observed for photos belonging to the LHR C_3 class: almost all the instances are mislabeled as belonging to HMR.

		REFERENCE						%
		NLR	HMR	LHR	MHR	HHR	DVR	
PREDICTION	NLR	1770	126	28	5	5	1	
	HMR	343	3131	1135	269	194	92	
	LHR	2	137	142	30	33	16	
	MHR	5	4	7	1333	128	1	
	HHR	1	0	3	7	1057	30	
	DVR	5	5	2	8	24	1510	

Table 5.9: Confusion matrix for the 6 class classification problem

In order to assess a class-wise benchmark of the rain intensity classification performance, a set of “one-versus-all” metrics were calculated starting from the confusion matrix. The metrics were then compared to reference values (Goodfellow et al. 2016; Zheng 2015; Murphy 2012; Chicco and Jurman 2020).

The one-versus-all comparisons splits the multi-class classification problem into separate binary one-versus-all comparisons. Since the considered classification has C_i classes where $i \in \{1, \dots, C'\}$, with $C' = 6$, they were required $C' = 6$ different binary one-versus-all comparisons. Each of them produced the metrics listed in Table 5.9, which were used get the measure of the classifier skills for each class.

Given the C_i class of interest as the “positive” class and all the other classes as the “negative” class, it was counted the number of corresponding TP, FP, TN and FN to calculate the desired metrics (Goodfellow et al. 2016; Zheng 2015; Murphy 2012; Chicco and Jurman 2020; McHugh 2012). TP were the outcomes where the model correctly predicts the C_i class. Similarly, TN were all the correct predictions where the model correctly assigns a class different from C_i . The off-diagonal elements represents the mis-predictions: FP were all the elements incorrectly classified as belonging to C_i , whereas FN are the elements mistakenly classified as not belonging to C_i .

Hence, the metrics of the classifier relative to the C_i class can be calculated as follows:

$$\text{Sensitivity} - \text{Recall} = \frac{TP_i}{(TP_i + FN_i)}$$

$$\text{Specificity} - \text{Selectivity} = \frac{TN_i}{(FP_i + TN_i)}$$

$$\text{Precision} - \text{Positive Predictive Value} = \frac{TP_i}{TP_i + FP_i}$$

$$\text{Negative Predictive Value} = \frac{TN_i}{TN_i + FN_i}$$

$$F1 = \frac{(1 + \beta^2) \times \text{precision} \times \text{recall}}{(\beta^2 \times \text{precision}) + \text{recall}} = \frac{2 \times \text{precision} \times \text{recall}}{\text{precision} + \text{recall}}$$

$$\text{Balanced Accuracy} = \frac{\text{sensitivity} + \text{specificity}}{2}$$

Prevalence express how often the C_i class actually occurred in the sample and reflects the distribution given in Table 5.8. It was calculating by dividing the sum of the elements in the i^{th} column (instances belonging to C_i) by the sum of all instances in the sample. Detection Rate counted exclusively the correct C_i class predictions made as a proportion of all of the predictions. Detection Prevalence computed the number of all C_i class predictions (correct and incorrect) made as a proportion of all of the

predictions. The rates are strongly influenced by the mislabeled instances of C_3 : the busted values are localized in C_2 and C_3 .

	NLR	HMR	LHR	MHR	HHR	DVR	REFERENCE VALUES
Sensitivity - Recall [%]	83.25	92.01	10.782	80.69	73.352	91.52	worst=0% best=100%
Specificity - Selectivity [%]	98.26	75.16	97.878	98.54	99.596	99.56	worst=0% best=100%
Precision - Pos Pred Value [%]	91.47	60.63	39.444	90.19	96.266	97.17	worst=0% best=100%
Neg Pred Value [%]	96.31	95.77	89.536	96.85	96.34	98.6	worst=0% best=100%
F1	0.8717	0.7309	0.16935	0.8518	0.83261	0.9426	worst=0 best=1
Prevalence	0.1834	0.2936	0.11364	0.1425	0.12434	0.1424	proportion of the class
Detection Rate	0.1527	0.2702	0.01225	0.1150	0.09121	0.1303	rate of true labels predicted
Detection Prevalence	0.1670	0.4456	0.03106	0.1275	0.09475	0.1341	prevalence of label prediction
Balanced Accuracy [%]	90.76	83.59	54.33	89.62	86.474	95.54	worst=0% best=100%

Table 5.10: Evaluation metrics: values for each class.

The macro-averaged F1-score, computed as a simple arithmetic mean of the per-class F1-scores, was 0.73, rather close to best reference value 1.

The proposed classifier provides generally much more accurate results than a random guess. The best performances were obtained in the classes C_1 , C_2 , C_4 , C_5 , C_6 (NLR, HMR, MHR, HHR, and DVR), whereas the mispredictions were mostly limited to C_3 class (LHR). The 6-class classifier correctly predicted only about a tenth of LHR pictures (sensitivity \approx 11%). About 11% of the total pictures were actually representing LHR (prevalence) but the class was predicted in approximately 3% of cases (detection prevalence), with about two fifth of these being correct (positive predictive value).

The observed model behavior may attribute to the relative scarcity of data: image number could not be inflated by experiments in the NIED Rainfall Simulator since the minimum rainfall rate is 20 mm/h for accurate rain reproduction. However, is not yet clear whether the class imbalance is the leading factor in determining the erroneous classification since the other minority classes (MHR, HHR, DVR) exhibit high rates of correct classification and don't suffer from the same degree of misclassification. A possible explanation for this inconsistency might be that sometimes it is difficult even for people to distinguish photos taken in rainy conditions with close values of precipitation intensity. This may be supported by the findings that the model tends to assign the pictures to an adjacent class.

The model performance mismatch could result in underestimating the rainfall rate, that's why it was proposed a new classification scenario with 5 classes presented in the next section (Section 5.5).

5.5 5 CLASS CLASSIFICATION

In ML studies, there is a potential for bias from poor construction of the dataset. To assess whether and how much the performance of the model can improve, it was determined a different binning set-up based on 5 classes for the rainfall intensity.

The rain rate categories were defined as mutually exclusive classes: NLR, HMR, MHR, HHR, and DVR, using the ranges given in Table 5.11.

These are obtained with respect to the previous one by merging the *old* LHR and MHR classes. The *new* MHR includes photos taken with a rainfall intensity $10 \text{ mm/h} \leq I < 30 \text{ mm/h}$. As can be seen in the previous subsection Section 5.4.1.2, the 6-class model yielded poor performance for the LHR class, introducing the risk of underestimating the rainfall rate. The

The new binning was chosen adopted to be on the safe side and allow a more balanced class distribution in the train set. Another advantage of using the modified classification is that it ensured that the model avoided the over-adaptation to peculiarities introduced by the specific images in the train set. The *old* LHR and the HMR contained exclusively the dash-cams pictures, due to the Rainfall Simulator characteristics. The NLR, MHR, HHR, and DVR classes entailed a mix of the pictures coming from the vehicles and the experiments. The NLR contained a balanced rate of pictures collected from the two data sources, whereas

the MHR, HHR, and DVR classes consisted mostly of pictures acquired during the Rainfall Simulator experiments, due to the ordinary occurrence of the natural precipitation phenomena.

The new classes were meant to contain a more equitable combination of the data sources to minimize the risk of learning features that are not descriptive nor informative for the addressed task.

A total of 61519 color JPEG images were labeled and organized according to the associated range of rainfall rate. For each class C_i , where $i \in \{1, \dots, 5\}$, the available data set was randomly divided into the non-intersecting subsets necessary with a ratio of 60 : 20 : 20 for training, validation and testing sets, respectively.

LABEL	INTENSITY RANGE [mm/h]	# OF IMAGES			
		(Total)	Train	Validation	Test
NLR - No Rain or Light Rain	< 5	10278	6026	2126	2126
HMR - High Moderate Rain	$5 \leq I < 10$	15551	8742	3406	3403
MHR - Medium Heavy Rain	$10 \leq I < 30$	13739	7814	2956	2969
HHR - High Heavy Rain	$30 \leq I < 50$	7818	4716	1661	1441
DVR - Violent Rain, Downpour	$I \geq 50$	8214	4914	1650	1650

Table 5.11: Data set creation: label division and number of labeled images per data set.

The obtained dataset did not have an exactly equal number of instances in each class, but the imbalance was milder compared to the previous case and was similarly expected to be negligible (Google Developers n.d.). The class distribution may be suitable for a general likelihood of precipitation in a real world scenario (excluding peculiar regional and latitudinal distribution that may require specific analysis).

Prior to model initialization, the size of the training set was enlarged through data augmentation (Shorten and Khoshgoftaar 2019) to reduce overfitting and enhance generalization, as seen before.

5.5.1 Results and discussion

5.5.1.1 Training and validation

The same setup used for the 6-class classifier (Section 5.3), described in Section 5.3, has been implemented for training and validating the 5-class model using the data subsets described in Table 5.11.

The set training configuration (Section 5.3.1) can be summarized as follows:

- Data Augmentation: horizontal flip.
- Loss: categorical cross-entropy. It was the cost function for monitoring and improving the model performance.
- Optimizer: RMSprop⁶ implementing the RMSprop algorithm (Tieleman and Hinton 2012) for self-updating of the network.
- Metric: accuracy. The measure of correct classification during training and testing.
- Adaptive learning rate: ReduceLROnPlateau⁷.

Figure 5.9 provides an overview of the loss and accuracy of the model over the training and holdout validation data during training, reporting the epoch of presentation of the instances on the abscissa and the value on the ordinate.

According to this plot, during the first 15 epochs the training accuracy increased while the loss decreased, constantly improving without abrupt changes.

After 18 epochs, the accuracy reached $\approx 82\%$ for the training set and $\approx 79\%$ for the validation set. The loss stalled at ≈ 0.45 for the training set and to ≈ 0.64 for the validation set.

For the subsequent epochs, the plots indicate that the training and validation curves reached a plateau. The small gap between the curves relative to the two subsets indicates that the network has converged reaching a point of stability without over-learning of the training data.

The training was stopped after 30 epochs, to avoid the degradation of the performance of the model (Goodfellow et al. 2016), visible when accuracy decreases and/or loss increases on the

⁶ keras.io/api/optimizers/rmsprop/

⁷ keras.io/api/callbacks/reduce_lr_on_plateau

unseen examples of the validation set. The presence of possible overfitting is graphically identifiable as a divergence between the curves of training and validation for each metric.

The smaller scale of *value* axes (*acc* and *loss*) indicates an improvement over the previous network.

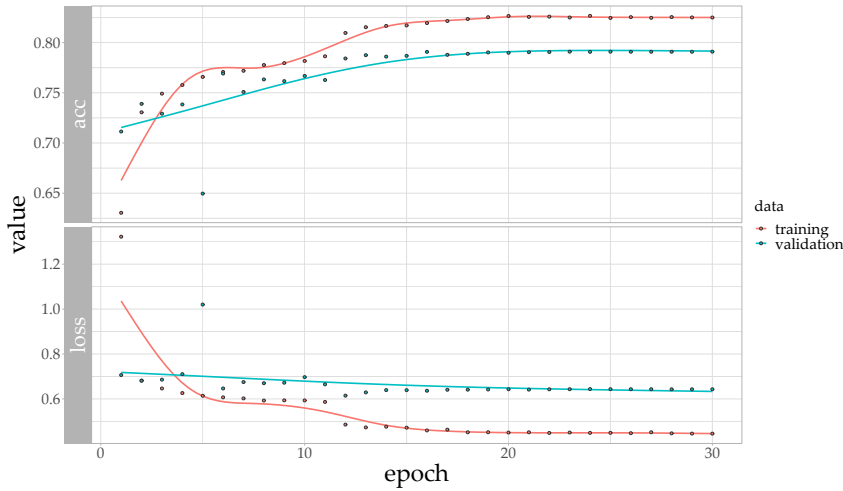


Figure 5.9: Training and validation: overall accuracy and loss values for the 5 class model.

After the 30 training epochs the final network reached an overall accuracy of 82.49% on the training set and 79.09% on the validation set (Figure 5.9) and a loss (Murphy 2012) respectively of 0.45 and 0.64.

The Loss (Binary Cross Entropy) was calculated as follows:

$$\text{Cross Entropy} = - \sum_{i=1}^{C'=5} t_i \log(f(\mathbf{s})_i)$$

Where t_i is the ground-truth for each class C_i and

$$f(\mathbf{s})_i = \frac{e^{s_i}}{\sum_j^C e^{s_j}}$$

is the last layer softmax activation function.

In this case, the considered problem is a 5-way classification: for each input picture x , the network outputs a label y_i that is associated with the C_i class where $i \in \{1, \dots, C'\}$ and the number of classes $C' = 5$. The class output is based on predicted class

probabilities distribution: the maximum activated score among all classes indicates the predicted class label.

The values differ significantly from a random guess considering the accuracy and loss of a balanced 5-class classification problem, where the non-informative values correspond to accuracy of 20% and loss of 1.60.

5.5.1.2 *Testing and evaluation*

The evaluation of the modified classification algorithm on the test set was performed according to the procedure used in the Section 5.4.1.2.

The overall accuracy calculated on the test set was 78.05%, slightly better than the previous model value of 77.71%. It is significantly higher from the random classifier accuracy and consistent with the values obtained in the previous steps (Section 5.5.1.1), with a 95% confidence interval was of 0.7728 and 0.788.

$$\text{Overall accuracy} = \frac{\text{correct predictions}}{\text{total predictions}} = 78.05\%$$

Reference values: worst=0%, best=100%.

Since the majority class C_2 label $y_2 = HMR$ has not changed the “no-information rate” is still *No Information Rate* = 0.29. The overall accuracy was enough for the model to offer significantly better performance over the no-information rate as indicated by the p-value 2.2×10^{-16} .

The Kappa statistic for the 5-class model was 0.7143, which is relatively high (possible values $\kappa \in [-1, 1]$, usual values $\kappa \in [0, 1]$). According to the reference values (Cohen 1960; McHugh 2012) the value obtained falls into the range $0.61 < \kappa < 0.80$, indicating substantial agreement between the obtained classifier and the true class labels once random accuracy is controlled for.

The obtained overall statistics show an overall moderate improvement.

To assess the improvements on a class-by-class basis, a breakdown of the predictions generated on the test examples is reported into the confusion matrix. The confusion matrix shown in Table 5.12 displays the cross-tabulation of the observed and predicted classes: the diagonal elements are the count of the correct predictions, whereas the off-diagonal elements are the count of the incorrect predictions made. The shades of gray represent the rate of the given class. These results are generally very promising.

Most of the instances were placed on the main diagonal (correct predictions); the misclassified elements are mostly examples belonging to the MHR C_3 class that are mistakenly associated with the HMR C_2 class.

		REFERENCE					
		NLR	HMR	MHR	HHR	DVR	
PREDICTION	NLR	1796	123	51	3	0	% 100 75 50 25 0
	HMR	304	3020	1227	146	74	
	MHR	24	256	1675	215	43	
	HHR	1	2	9	1052	31	
	DVR	1	2	7	25	1502	

Table 5.12: Confusion matrix for the 5 class classification problem.

A series of “one-versus-all” metrics was then calculated and compared to the corresponding reference values (Goodfellow et al. 2016; Zheng 2015; Murphy 2012; Chicco and Jurman 2020). The one-versus-all comparisons splits the multi-class classification problem into 5 separate binary one-versus-all comparisons, one binary comparison for each possible outcome C_i , being $i \in \{1, \dots, C'\}$ and $C' = 5$. Given the C_i class of interest as the “positive” class and all the other classes as the “negative” class, the count of TP, FP, TN, and FN formed the basis for the metrics. Hence, the metrics associated with each C_i class were computed using the equations given in Section 5.4.1.2:

$$\text{Sensitivity} - \text{Recall} = \frac{TP_i}{(TP_i + FN_i)}$$

$$\text{Specificity} - \text{Selectivity} = \frac{TN_i}{(FP_i + TN_i)}$$

$$\text{Precision} - \text{Positive Predictive Value} = \frac{TP_i}{TP_i + FP_i}$$

$$\text{Negative Predictive Value} = \frac{TN_i}{TN_i + FN_i}$$

$$F1 = \frac{(1 + \beta^2) \times \text{precision} \times \text{recall}}{(\beta^2 \times \text{precision}) + \text{recall}} = \frac{2 \times \text{precision} \times \text{recall}}{\text{precision} + \text{recall}}$$

$$\text{Balanced Accuracy} = \frac{\text{sensitivity} + \text{specificity}}{2}$$

$$\text{Prevalence} = \frac{TP_i + FN_i}{TP_i + FP_i + TN_i + FN_i} = \frac{\text{instances } C_i}{\text{total predictions}}$$

$$\text{Detection Rate} = \frac{TP_i}{TP_i + FP_i + TN_i + FN_i}$$

$$\text{Detection Prevalence} = \frac{TP_i + FP_i}{TP_i + FP_i + TN_i + FN_i}$$

Each of them produced the metrics used to assess classifier skills for the 5 different classes.

A summary of calculated metrics is in Table 5.13.

The results appeared to be unaffected by the class imbalance since the relatively worst results were obtained in the C_3 class, label $y_3 = MHR$, that has prevalence $\approx 26\%$ and the predictions within the minority classes (C_4 labeled $y_4 = HHR$ with prevalence $\approx 12\%$, C_5 labeled $y_5 = DVR$ with prevalence $\approx 14\%$) were pretty accurate.

Best performances were achieved in the C_5 class described by label $y_5 = DVR$ (all metrics values were almost perfect), despite being a minority class (prevalence $\approx 14\%$) in terms of both sensitivity ($\approx 91\%$) and specificity ($> 99\%$).

Similarly to the 6-way classification model, the error were located in the low-medium heavy rainfall range: the measures are affected by the mislabeled instances of C_3 . For 1227 instances, the classifier predictions incorrectly indicated the C_2 class when the images were belonging to C_3 , lowering the model precision for C_2 and sensitivity for C_3 .

The differences between the 6-class model and the 5-model were modest.

	NLR	HMR	MHR	HHR	DVR	REFERENCE VALUES
Sensitivity - Recall [%]	84.48	88.75	56.42	73.005	91.03	worst=0% best=100%
Specificity - Selectivity [%]	98.13	78.61	93.76	99.576	99.65	worst=0% best=100%
Precision - Pos Pred Value [%]	91.03	63.3	75.69	96.073	97.72	worst=0% best=100%
Neg Pred Value [%]	96.57	94.38	86.2	96.293	98.53	worst=0% best=100%
F1	0.8763	0.7389	0.6465	0.82965	0.9426	worst=0 best=1
Prevalence	0.1834	0.2936	0.2562	0.12434	0.1424	proportion of the class
Detection Rate	0.1550	0.2606	0.1445	0.09078	0.1296	rate of true labels predicted
Detection Prevalence	0.1702	0.4117	0.1910	0.09449	0.1326	prevalence of label prediction
Balanced Accuracy [%]	91.30	83.68	75.09	86.291	95.34	worst=0% best=100%

Table 5.13: Evaluation metrics: values for each class.

Taken together, the results showed significant outcomes for both classifiers.

The approximations inherent in both models are acknowledged: the achievable results cannot be claimed to universally be useful for all rainfall monitoring applications. In some cases, the data gathered from the proposed Convolutional Neural Networks (CNNs) might be supplemented by data reporting more precise (quasi) instantaneous rainfall intensity. However, they demonstrate the adequacy of the method for the problem of interest: monitoring severe rainfall in urban catchments within Early Warning Systems. The best performances are achieved in heavy rainfall and no-rain conditions, whereas the mispredictions are related to lower rainfall rates. In the application field of interest, it is important to gather high sensitivity in extreme precipitation events, to mitigate the risk of missing cases of severe rainfall that could lead to delays in early warning systems. It is worth remark-

ing here that the near instantaneous liquid precipitation rate is given in units of mm/hr for the sake of standardization. It represents the equivalent hourly rain that would have fallen if a given short-term rainfall rate remained constant for one hour. Typically urban floods stem from a hydro-meteorological extreme events of severe precipitation in short spans of time (Chapter 1). Hence, quasi-instantaneous rainfall rate values appear bigger than hourly precipitation.

The performance obtained in Classes with rainfall intensity $I > 30 mm/h$ may guarantee that the model can recognize the dangerous pluviometric forcing more prone to trigger urban floods. It was also found that the Transfer Learning with CNN approach produces good quality results in both models in terms of specificity for all classes. This, in combination with the ample skills in the $C_1 = NLR$, might ensure to avoid unnecessary alerts.

The occurrence of misclassifications in less severe near instantaneous rainfall intensities may be explained by the constraint of the dataset and the intrinsic characteristics of the pictures. Closer inspection of the training photos reveals some ambiguity in the perceptual aspects of these classes of rain: the raindrops accumulated and wiped on the vehicle windshield make the scenes very similar. Furthermore, a common behavior associated with precipitation is sticking a hand out from under an umbrella to feel the rain since the visual effects of precipitation may be often inconspicuous.

The limitation of the system is consistent with the findings in Chapter 4: the proposed approach does not suit scenes that are misleading for human vision. Additional data may be gathered to address gaps that are apparent. Further data collection is required to reach better results within the range of low heavy precipitation $10 \leq I < 20$. A larger dataset might expose a different and perhaps more balanced perspective on the classes.

It is necessary to have access to different kinds of pictures and known rainfall rates but this is not straightforward.

PART III

MATERA CASE STUDY

MATERA CASE STUDY

Matera is located in the eastern part of Basilicata region in Southern Italy (Figure 6.1), bordering the south-western part of the metropolitan city of Bari (with the municipalities of Altamura, Gravina in Puglia and Santeramo in Colle), the extreme part north-west of the province of Taranto (with the municipalities of Ginosa and Laterza). It is the capital of the province of Matera, the second largest town in Basilicata by population and the largest municipality. It rises at 401 m above sea level, right on the border between the Murge plateau to the east and the Bradanica pit to the west, crossed by the Bradano river. The course of this river is blocked by a dam, built in the late 50s for irrigation purposes, forming the artificial lake called Lake San Giuliano, which is part of the regional San Giuliano Nature Reserve.



Figure 6.1: Area of interest.

In a phenomenological perspective, each settlement becomes a semiotic object (Eco 2011) with multiple "narrative dimensions" and is the result of a balance between construction and destruction across the time and dialogue with natural elements such as watercourses, vegetation, exposure, geomorphology, revealing a structure made by flows and physical actions that can be read and interpreted (Macaione and Sichenze 2013; Macaione, Ippolito, et al. 2018). Structural components of the territorial context lie on multiple and overlapping levels (Figure 6.2, Figure 6.3) which include physical-environmental, socioeconomic, and historical levels that are not always visible. Matera is a place that has resisted the adversities and attacks inflicted by the time of history, assuming an inestimable historical value and a huge attractive

charm (Sichenze 2017; Sichenze 2014). The town is claimed as the third-oldest continually inhabited settlement in the world¹. Understanding the diachronic evolution of the urban morphology is important not only for knowledge of the historical context and the cultural heritage, but also for tracing the hydrological framework.



Figure 6.2: Sassi view. A millenary layered urban cultural landscape.

In the history of Matera, water played an important role in driving urban evolution as demonstrated by historical changes in systems for water collection, storage, drainage, and flows (Laureano 2012; Manfreda et al. 2016; Ermini et al. 2010; Spilotro et al. 2019; Mays 2010; Laureano 2009). The hydrologic traits evolved across successive generations of urban ecosystems via adaptations over the centuries, shifting according to the changes of pressures. The cultural importance of water in whittling Matera life was iconically represented by Japanese artist Kenjiro Azuma with the big drop shaped sculpture *Mu 765 G²* in Piazza Giovanni Pascoli.



Figure 6.3: Sassi view from an house in via Lombardi.

1 <https://www.theguardian.com/travel/2019/sep/01/matera-basilicata-italy-european-capital-of-culture-2019>

2 [https://luoghidelcontemporaneo.beniculturali.it/mu-765-g-\(la-goccia\)](https://luoghidelcontemporaneo.beniculturali.it/mu-765-g-(la-goccia))

6.1 DIACHRONIC EVOLUTION OF THE URBAN MORPHOLOGY

The studies by Rota (2016) and Laureano (2012) offer probably the most comprehensive analysis of the historical and ecological aspects of the evolution through time of the urban morphology of Matera that can not be separated from the Materan ancient hydraulic systems (Manfreda et al. 2016; Ermini et al. 2010; Spilotro et al. 2019; Mays 2010; Laureano 2009).

Settlements in Matera dates from Palaeolithic age, as testified by the evidence of prehistoric human occupation on hilltops and along the cavernous ravines surrounding Matera's site. Due to continued reuse of the site of the subterranean spaces and through expanded urban development of the cliff, datable prehistoric remains within the urban area are limited to Eneolithic and Bronze Age artefacts. The early settlers identified the natural resources and introduced the shaping of caves for habitation and for water and food storage (Toxey 2009). Neolithic entrenched villages were found in Murgecchia, Tirlecchia, Trasano, Murgia Timone, Serra d'Alto, Trasanello, and in the Civita. The distribution of the Neolithic and Paleolithic settlements results from the proximity of the small Jurio waterfalls, an important natural reserve of water.

The geomorphology of the Gravina canyon, a deep ravine on the bottom of which the homonymous stream flows, strongly influenced the development of the settlements (Figure 6.7).

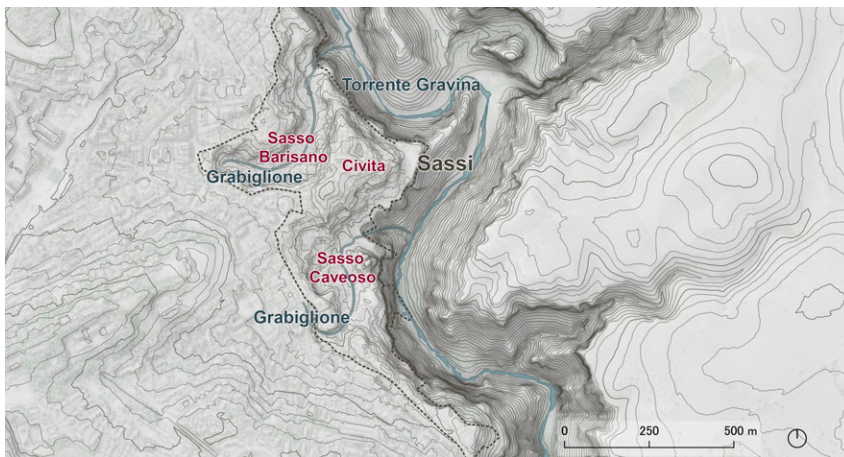


Figure 6.4: Hydro-morphological elements of Sassi settlement system.

The *Civita*, the central spur of the *Sassi*, is delimited by two torrential incisions called *grabiglioni* (small ravines, Rota 2016). On the slopes of the *grabiglioni*, the *Sasso Barisano* and the *Sasso*

Caveoso developed successively, adopting housing structures consisting of overlapping terraces. The *Sassi*, meaning *boulder, rock*, form an urban complex carved and built in calcarenite (locally improperly called *tuff*). Calcarenite is a calcareous sedimentary rock of biochemical origin; its availability, ease of quarrying and workability allowed the settlement and its use as construction materials since prehistoric times. By contrast, these propitious features could increase the vulnerability to deterioration processes and weathering phenomena.

The *Sassi* are modeled in a vertical succession of levels totally or partially excavated and built, depending on the original conformation of the slope, integrating the natural terraces with vertical cuts of the calcarenite rock according to the level curves. The heart of the city formed as a “chthonic construction” that modeled as an urban ecosystem of exchanges with and parsimonious use of natural elements, especially water, soil and sunlight. The historical elements of the excavated architecture (hypogea, urban voids, public and private spaces) epitomize a capacity for adaptation and regeneration to natural and anthropic phenomena. The complex urban system of *Sassi* lived in a balance of environmental, energetic and poetic sustainability, making up a layered cultural heritage of a millenary urban knowledge landscape, which might still suggest strategic solutions to contemporary issues. In this sense, *Matera* can be considered a paradigmatic example of the reinvention of places.

Originally, the *Sassi* basins hosted a water collection system for irrigation purposes. The demographic pressures lead to an increasing need for space and a consequent transformation of the cisterns for residential purposes (Figure 6.5).

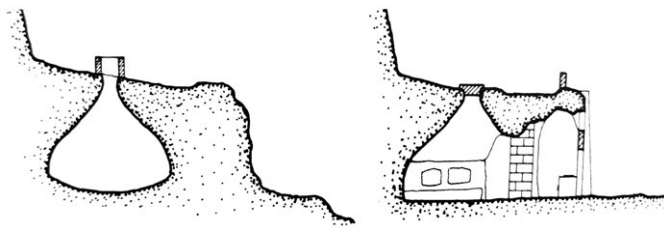


Figure 6.5: Cistern transformed into a dwelling space. Reproduced from Laureano 2012.

As time went on, architectural types of cisterns and residential ones intermingled increasingly (Figure 6.6). During the Classical age (IV century BC), the population is concentrated in scattered nuclei, mainly on *Civita* and in *Sasso Caveoso*.

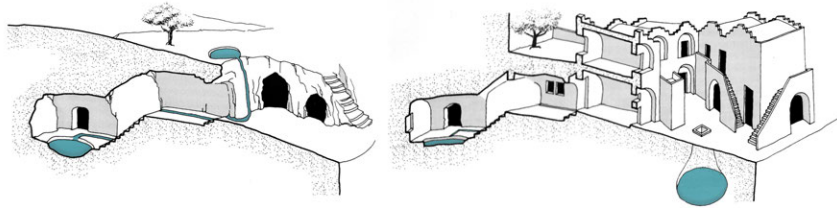


Figure 6.6: *Jazzo* and *vicinato*. Reproduced from Laureano 2012.

The urban morphology developed along with water infrastructures as an adaptive habitat system documenting a millennial human journey (Figure 6.7).



Figure 6.7: Evolution of the Sassi urban ecosystem. Reproduced from Laureano 2012, watercolor by D. Giorgi.

The anthropological and spatial optimal balance of the housing system with stratified terraces and the water collection surface, storage and consumption ensured a good regulation of surface and sub-surface waters. The ancient hydraulic systems spread over overlapping levels combining the different principles of capture, distillation and condensation. During heavy rains, the rain-water harvesting systems protected homes and inhabitants from runoff and erosion phenomena and, at the same time, ensured the accumulation and use of scarce water resources: the precipitation was conveyed by gravity from the slopes and roofs (channeled by means of descending terracotta conduits, Figure 6.8) and collected in a diffused single or neighborhood - *vicinato* - hypogean cistern system. During the dry season, the cisterns accumulated

condensation water from atmospheric humidity captured by the caves in the nighttime.

During the early Middle Ages (IX-XI century), monasticism elements and hydraulic technology blended into a coherent urban fabric, the rupestrian habitat of Byzantine and oriental origin representing the *rock civilization*.

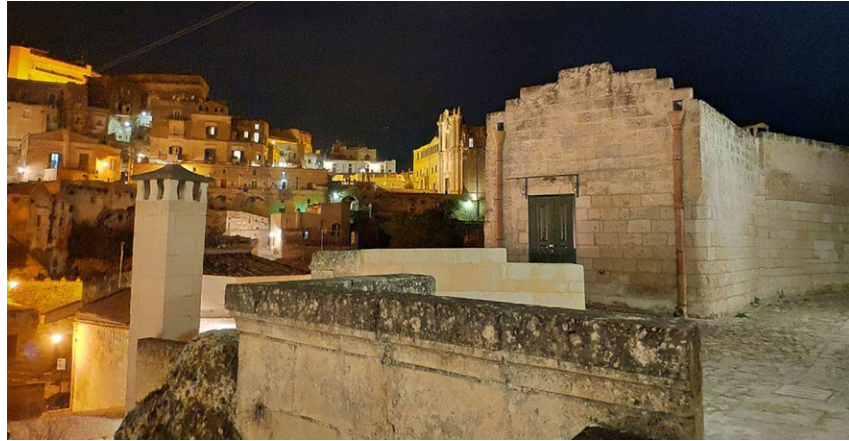


Figure 6.8: Sassi view. The roof is contained in the masonry walls and descending terracotta conduits are visible on the facade.

In the Norman-Swabian period (XI-XII century) the feudal system catalyzed the development: the Civita became a fortified urban center of western origin, whereas outside the walls the population is distributed in the rocky settlement that forms the first nuclei of the Sassi. During the Swabian-Angevin phase (XIII-XIV century) the city becomes an important ecclesiastical center: the Cathedral and the Old Castle (*Castelvecchio*) were built inside the walled nucleus of Civita, rock churches and monasteries developed *extra moenia*. The terraces of the Sassi structured themselves into semirural habitats. The medieval pattern remained heavily characterized by hypogeum structures following the morphology of the areas and infrastructural network.

During the Aragonese Renaissance phase (XV-XVI century), Matera experienced a consolidation of the urban organization. The Civita became the historic and representative center, the Sassi were the dwellings for the middle and lower classes, the Piano developed its urban infrastructure becoming the center of commercial life and of public administration. Tramontano Castle was built on a hill outside the medieval city. Construction of the new city walls and towers began. There was evidence of the Casalnuovo district and of the Ghetto of Seminario.

A new expansion (XVII-XVIII century) determines the Baroque urban arrangements (*forma urbis*), based on the hierarchy of perspective values of the “urban scenes”.

The morphology evolution continued to balance residential development needs and water infrastructural systems. The distributed system consisting of single or neighborhood cistern was expanded with large and central storage tanks, built following the urban expansions after 1500 and in the second half of the 1800s (e.g. the *Palombaro grande* lying underneath the main square Piazza Vittorio Veneto).

Demographic pressures generated significant increases in soil and water consumption, altering the urban ecosystem balance. The raw wastewater was still disposed directly into the *grabighioni* which served as an open-air channel for the collection of sewage, becoming a serious health threat due to the population growth. The hygienic-social decay in the XIX century caused the displacement of the wealthier classes in the upper margin of the Sassi (Piano).

At the beginning of the XX century, the water resources were not sufficient to satisfy the needs of approximately 17,000 inhabitants and the situation became increasingly unsustainable from the health point of view. The ancient water supply systems were replaced by a modern aqueduct.

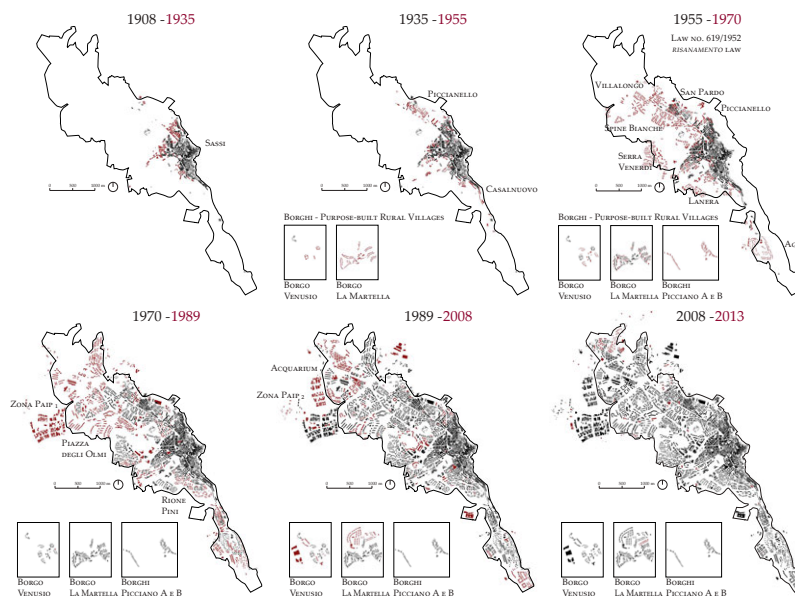


Figure 6.9: Contemporary urban morphology.

The period immediately following World War II determined a new demographic context. The distinctive cave homes were

inadequate for additional housing needs, shared with animals and riddled with disease. Carlo Levi's "Christ stopped at Eboli" brought to national attention the dwelling issues of the Sassi. The leader of the Italian Communist Party Togliatti was the first to arrive in the Lucanian city in 1948 and defined the unhealthy environments as "national shame". A few years later, De Gasperi, founder of the Christian Democratic Party and first Prime Minister of the Italian Republic, had declared that evacuating and resettling Materan peasants was a national priority.



Figure 6.10: Henri Cartier-Bresson: Matera, Basilicata, Italy. © Henri Cartier-Bresson | Magnum Photos

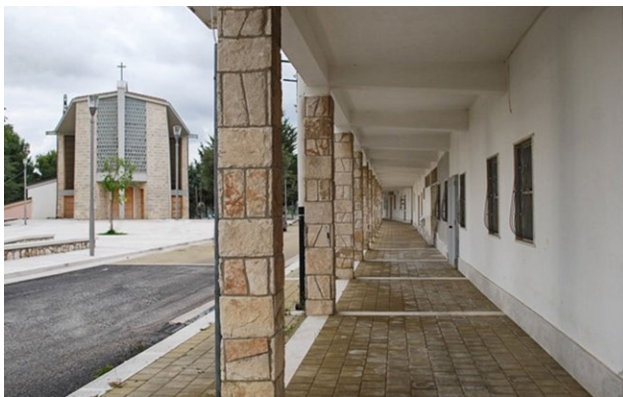
The distinct catholic and communist ideas about society and urban planning produced a debate of anthropological, sociological, and urban interest (Figure 6.10) with a substantial contribution by Olivetti (president of the National Institute of Urban Planning) and sociologist Friedman. The government implemented a rehousing program for Matera's cave dwellers in 1952. As a result, the Sassi were gradually emptied and the local population was rehoused in purpose-built rural villages and urban quarters. A process of socio-economic and urban planning regeneration, the *Risanamento*, led to new districts and purpose-built rural villages designed by prestigious exponents of contemporary urban planning and architecture (e.g. La Martella by Quaroni, Serra Venerdi by Piccinato, Spine Bianche by Aymonino and De Carlo, etc., e.g. see Figure 6.11), representing an important work of the current Neorealist Rationalism Italian.



(a) La Martella by Ludovico Quaroni with Gorio, Lugli and others (1951/1953)



(b) Spine Bianche by Aymonino, with De Carlo, Fiorentino and others (1955/1959)



(c) Venusio by Piccinato and others (1954/1957)

Figure 6.11: Some of the new districts of *Risanamento*.

Since the 1980s, with the restoration of the Sassi, new vital energies were born, transforming the old poverties into richness. In 1993, UNESCO granted The Sassi and the Park of the Rupesian Churches of Matera World Heritage status. The city was an European Capital of Culture in 2019. Matera represents a

resilient “model” of unique urban-living experience (Sichenze 2014; Macaione, Ippolito, et al. 2018, Figure 6.12).



Figure 6.12: Old and new urban fabric view.

From a hydrologic point of view, nowadays the city suffers from recurrent urban flooding due to city landscapes (both in the historical center and in the modern districts) that cannot absorb or otherwise manage heavy rainfall. The recent events (see Section 6.3) triggered by extreme meteorological phenomena demonstrate the change in the contemporary relationship between man and water. Most of the ancient infrastructures don't serve their original function of regulation of the water regime since replaced with more efficient modern systems. The *grabiglioni* were closed with the arrival of the sewerage system, becoming the access routes to the Sassi. Although modern water and sewerage infrastructures are present, the water-soil-urbanization balance is profoundly altered. In light of this diachrony between rainwater and anthropogenic systems, it is important to investigate the current dynamics between urban sub-basins and meteoric water in order to define the strategies of interventions (in particular non-structural) for risk mitigation, monitoring and response, with practices involving behavioral factors, information and perception processes.

In this sense, one of the broader objectives of the research is the recreation of a novel *Materan* resilience declined in the field of urban flood risk.

Flooding can damage architectural heritage and immovable cultural heritage. An extreme rainfall event can result in a wide range of damages caused by different concomitant forces: horizontal static pressure of raised water; upward hydrostatic pressure; dynamic low velocity streams; dynamic high-velocity streams; dynamic impact of waves; dynamic impact of floating objects; compacting of soils or infill; changes in subsoil conditions; saturation of materials with water; contamination of materials with chemical and biological agents; formation of barriers; ice floes; and post-flood effects (Drdácký 2010).

The geological and urban history of Matera site is graphically depicted in Figure 6.13 through a series of historically accurate 3D computer graphics generated panoramas, in eight chronological phases. The 3D reconstructions were gathered from *Matera città Narrata* (Matera: Tales of a City) project³ (Eva Pietroni et al. 2011; E. Pietroni 2012) which is a project realized by the Institute for Technologies Applied to Cultural Heritage (ITABC CNR) and supported by the Regional Promotion Agency (APT) and the Basilicata Regional Government's Department of Manufacturing/Production Activities, involving a web site and applications for mobile devices for the access to cultural contents using new technologies.

Figure 6.13: Matera: Tales of a City - 3D reconstructed panoramas.



³ www.materacittanarrata.it

POINT OF VIEW Piazza Vittorio Veneto

NOW



LATE 19TH CENTURY (1875 – 1898)



ARAGONESE RENAISSANCE PERIOD (XV-XVI A.C.)



SWABIAN – ANJOU PERIOD (XIII – XIV CENTURY A.C.)



THE BYZANTIUM AND NORMAN PERIOD (IX – XII CENTURY A.C.)



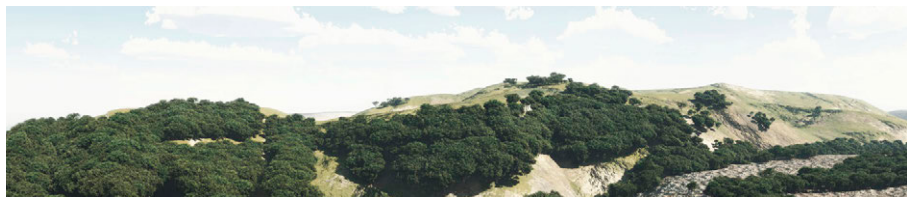
CLASSICAL PERIOD (IV CENTURY B.C.)



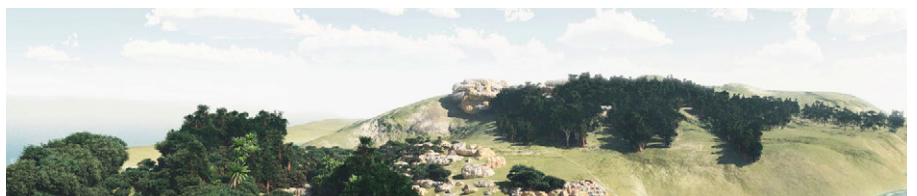
THE NEOLITHIC AGE (5.000 – 4.000 B.C)



THE SUPERIOR PLIOCENE AGE (2 MILLION YEARS AGO)



THE CALABRIAN PLEISTOCENE AGE (1 MILLION YEARS AGO)



POINT OF VIEW Sant' Agostino

NOW



LATE 19TH CENTURY (1875 – 1898)



ARAGONESE RENAISSANCE PERIOD (XV-XVI A.C.)



SWABIAN – ANJOU PERIOD (XIII – XIV CENTURY A.C.)



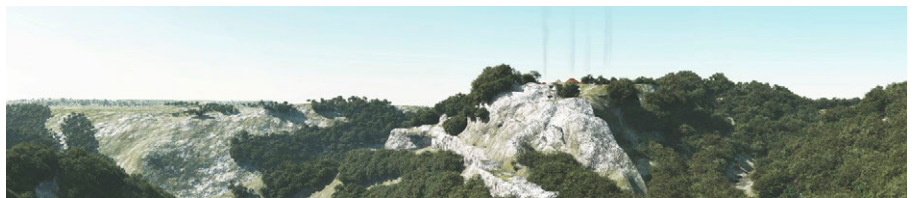
THE BYZANTIUM AND NORMAN PERIOD (IX – XII CENTURY A.C.)



CLASSICAL PERIOD (IV CENTURY B.C.)



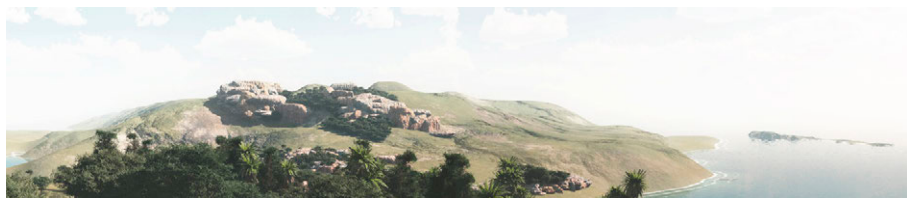
THE NEOLITHIC AGE (5.000 – 4.000 B.C.)



THE SUPERIOR PLIOCENE AGE (2 MILLION YEARS AGO)



THE CALABRIAN PLEISTOCENE AGE (1 MILLION YEARS AGO)



POINT OF VIEW Belvedere della Murgia

NOW



LATE 19TH CENTURY (1875 – 1898)



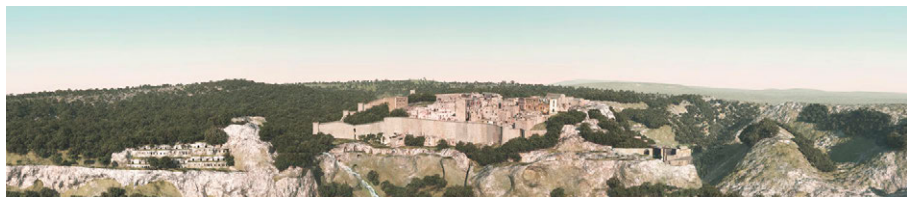
ARAGONESE RENAISSANCE PERIOD (XV-XVI A.C.)



SWABIAN – ANJOU PERIOD (XIII – XIV CENTURY A.C.)



THE BYZANTIUM AND NORMAN PERIOD (IX – XII CENTURY A.C.)



CLASSICAL PERIOD (IV CENTURY B.C.)



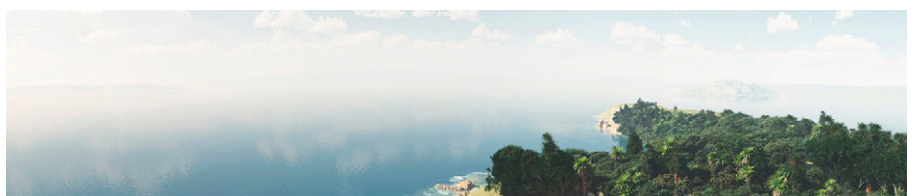
THE NEOLITHIC AGE (5.000 – 4.000 B.C.)



THE SUPERIOR PLIOCENE AGE (2 MILLION YEARS AGO)



THE CALABRIAN PLEISTOCENE AGE (1 MILLION YEARS AGO)



POINT OF VIEW Piazza Giovanni Pascoli

NOW



LATE 19TH CENTURY (1875 – 1898)



ARAGONESE RENAISSANCE PERIOD (XV-XVI A.C)



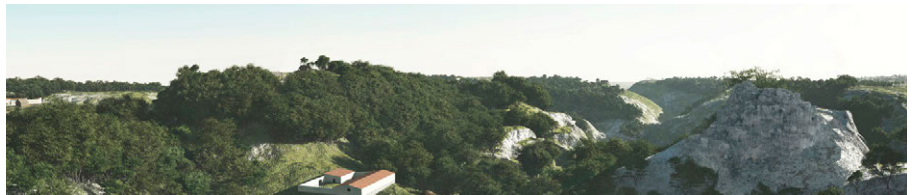
SWABIAN – ANJOU PERIOD (XIII – XIV CENTURY A.C.)



THE BYZANTIUM AND NORMAN PERIOD (IX – XII CENTURY A.C.)



CLASSICAL PERIOD (IV CENTURY B.C.)



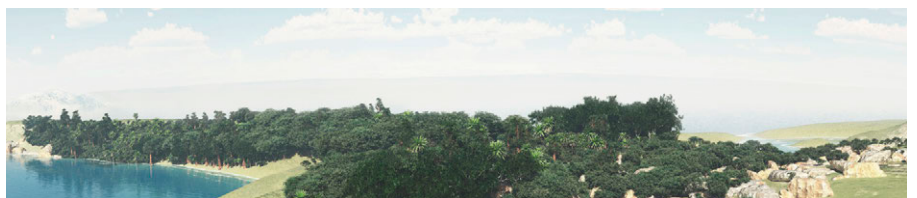
THE NEOLITHIC AGE (5.000 – 4.000 B.C)



THE SUPERIOR PLIOCENE AGE (2 MILLION YEARS AGO)



THE CALABRIAN PLEISTOCENE AGE (1 MILLION YEARS AGO)



POINT OF VIEW Piazza Postergola - Porta Pistola

NOW



LATE 19TH CENTURY (1875 – 1898)



ARAGONESE RENAISSANCE PERIOD (XV-XVI A.C.)



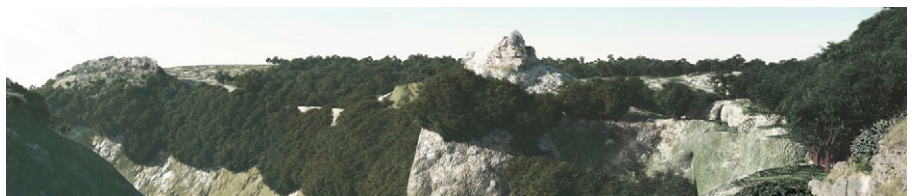
SWABIAN – ANJOU PERIOD (XIII – XIV CENTURY A.C.)



THE BYZANTIUM AND NORMAN PERIOD (IX – XII CENTURY A.C.)



CLASSICAL PERIOD (IV CENTURY B.C.)



THE NEOLITHIC AGE (5.000 – 4.000 B.C.)



THE SUPERIOR PLIOCENE AGE (2 MILLION YEARS AGO)



THE CALABRIAN PLEISTOCENE AGE (1 MILLION YEARS AGO)



POINT OF VIEW Piazzale del Duomo (Cattedrale)

NOW



LATE 19TH CENTURY (1875 – 1898)



ARAGONESE RENAISSANCE PERIOD (XV-XVI A.C.)



SWABIAN – ANJOU PERIOD (XIII – XIV CENTURY A.C.)



THE BYZANTIUM AND NORMAN PERIOD (IX – XII CENTURY A.C.)



CLASSICAL PERIOD (IV CENTURY B.C.)



THE NEOLITHIC AGE (5.000 – 4.000 B.C.)



THE SUPERIOR PLIOCENE AGE (2 MILLION YEARS AGO)



THE CALABRIAN PLEISTOCENE AGE (1 MILLION YEARS AGO)



6.2 STATISTICS

To frame the urban and territorial system, Census data can provide fairly accurate information on the characteristics of residents and buildings. *Open data* taken from the *Istat Census 2011 - 15th General Census of Population and Housing* by Italian National Institute of Statistics (Istat Istituto Nazionale di Statistica 2011) were subjected to univariate descriptive statistics to provide benchmarks of the population and housing stock. The 15th General Census of Population and Housing is dated 9 October 2011. The observational field is disaggregated to the sub municipal level (Figure 6.14).

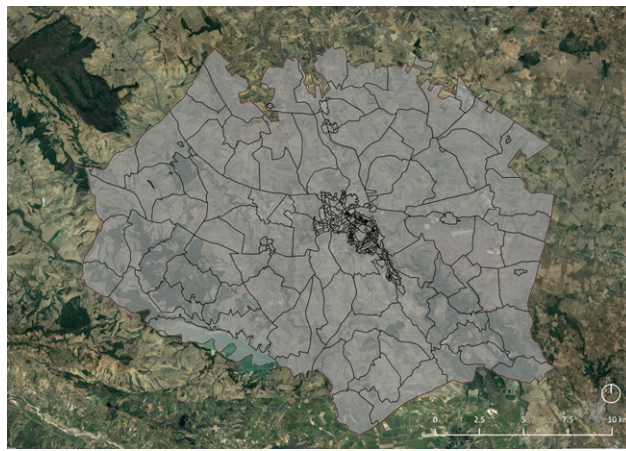


Figure 6.14: Istat Census 2011: Census sections for Matera Municipality.

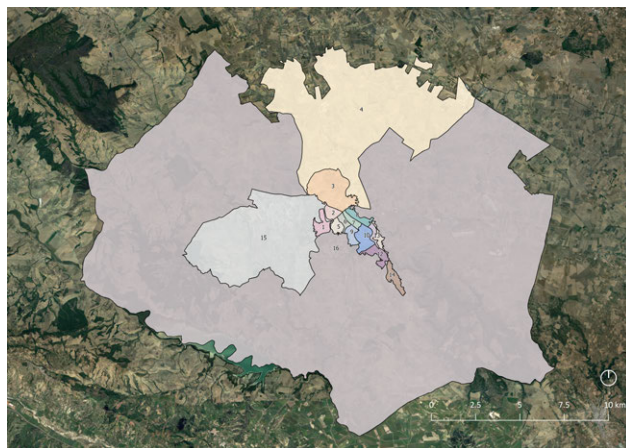


Figure 6.15: Macro areas of the Municipal Structural Plan.

The settlement system of Matera is articulated by the Municipal Structural Plan (*Piano Strutturale Comunale*) in 16 macro-areas: 1 - Zone Artigianali; 2 - Granulari; 3 - Serra Rifusa; 4 - Venusio; 5 -

San Giacomo - Via La Martella; 6 - San Giacomo; 7 - Spine Bianche; 8 - Piccianello; 9 - Serra Venerdi; 10 - Macamarda - Castello; 11 - Centro Storico; 12 - Lanera - Pini; 13 - Sassi; 14 - Agna; 15 - La Martella; 16 - Extraurbano (see Figure 6.15). Each urban areas differs from the others by its functional role, recognizability and spatial identity.

The residents, i.e. the habitually domiciled population in the municipal territory, on 1st January 2020 amounted to 60411, with an average density of about 157 *inhab./km²* (≈ 404 *inhab./sqmi*) (Table 6.1), below the Italian average⁴. The population is concentrated in the urban core of the municipal territory.

SETTLEMENT SYSTEM	CENSUS SECTIONS [n]	DENSITY [inhab./ha]	TERRITORY SURFACE [ha]
ZONE ARTIGIANALI	18	5.71	82.10
GRANULARI	9	107.90	51.15
SERRA RIFUSA	12	13.88	425.57
VENUSIO	18	0.10	4914.18
SAN GIACOMO - VIA LA MARTELLA	9	5.71	45.42
SAN GIACOMO	6	93.84	33.42
SPINE BIANCHE	29	88.62	41.04
PICCIANELLO	64	83.35	58.08
SERRA VENERDÌ	41	87.33	57.05
MACAMARDA - CASTELLO	35	5.71	110.87
CENTRO STORICO	29	99.37	31.79
LANERA PINI	25	59.06	76.42
SASSI	5	49.87	38.02
AGNA	25	5.71	79.35
LA MARTELLA	12	0.80	2928.84
EXTRAURBANO	76	0.07	29858.72
Total	413	1.57	38832.02

Table 6.1: Population and density of the macro areas.

The population analysis delineated the individual's characteristics, e.g. age and ethnicity, that influence the perception of social responsibility which is a driving factor in building com-

⁴ <https://www.indexmundi.com/>

munity flood resilience through individual and collective actions (Soetanto et al. 2017).

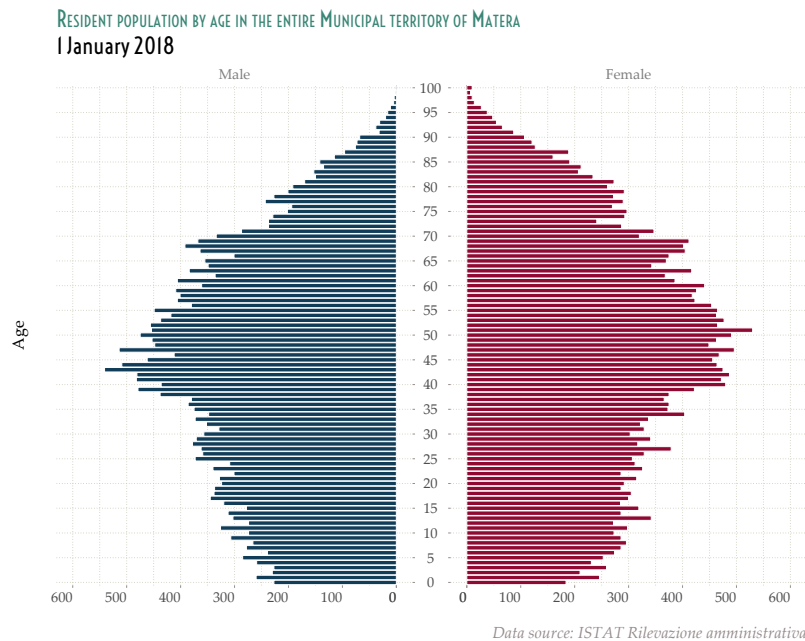


Figure 6.16: Demographic pyramid: Resident population by age and sex.

To graphically illustrate the age and sex composition of the population, a demographic pyramid was traced in Figure 6.16 using a paired bar chart-type graphic.

Population can be described by a Constrictive pyramid: residents have long life expectancy, a low death rate, but also a low birth rate. The percentage of elderly population is extremely high, this can increase flood risk: people aged 65 or over tend to be more vulnerable and experience greater impacts from flood events, such as restriction of access to medicine, personal aids, health treatments or equipment, etc. Aging may also affect the level of preparedness, capacity to cope during events, ability to respond and recover.

The education level is not particularly high and there is a significant rate of illiteracy and low literacy (Figure 6.17).

The gender gap is close to zero: the average level of educational attainment among men presents values that are similar to the average level of educational attainment among women.

Lower education level and low degree of numeracy is associated with higher vulnerability of population: it tends to affect risk perception, awareness and coping capacity at both individual and community level.

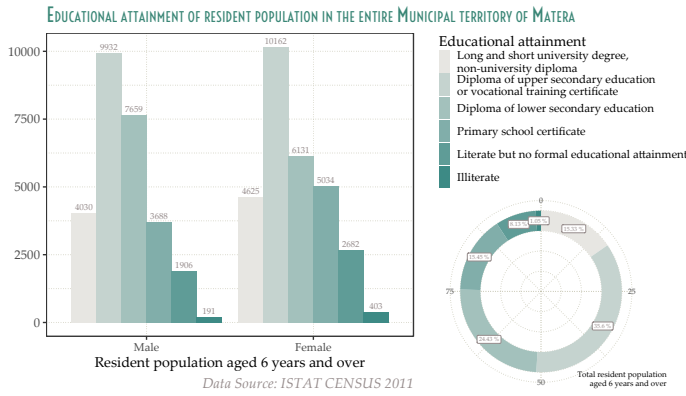


Figure 6.17: Educational attainment of resident population in the entire Municipal territory of Matera by sex

Ethnicity and migration status are additional factors of flood-related social vulnerability since these may impose cultural and language barriers, but resident foreigner presence in Matera municipality is pretty low so it isn't a significant contributory factor to the development of the risk (Figure 6.18).

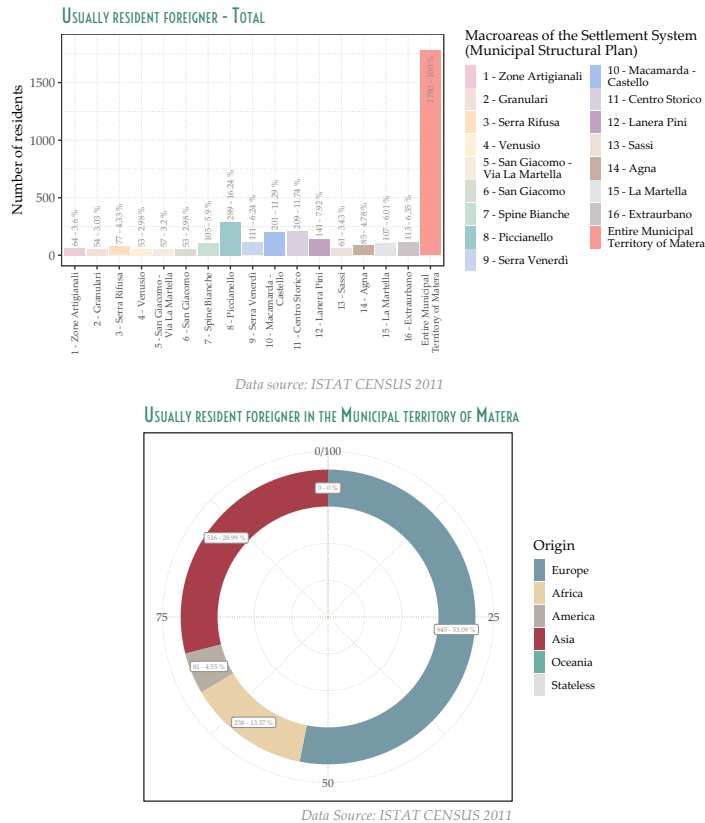
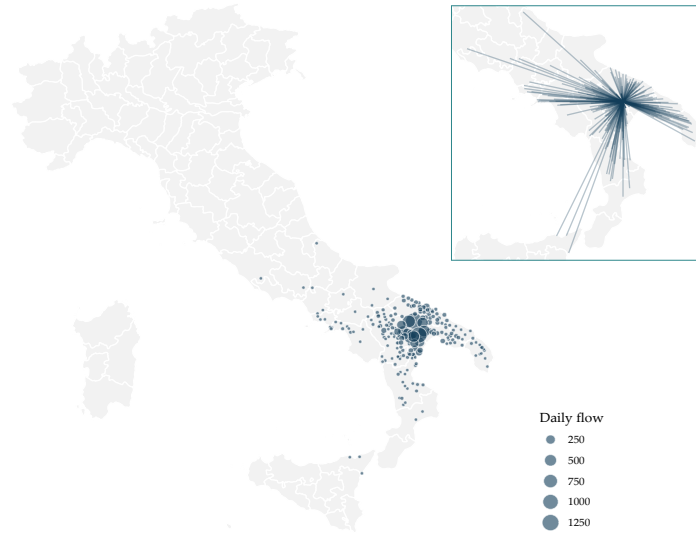


Figure 6.18: Resident foreigner by macro areas and origin

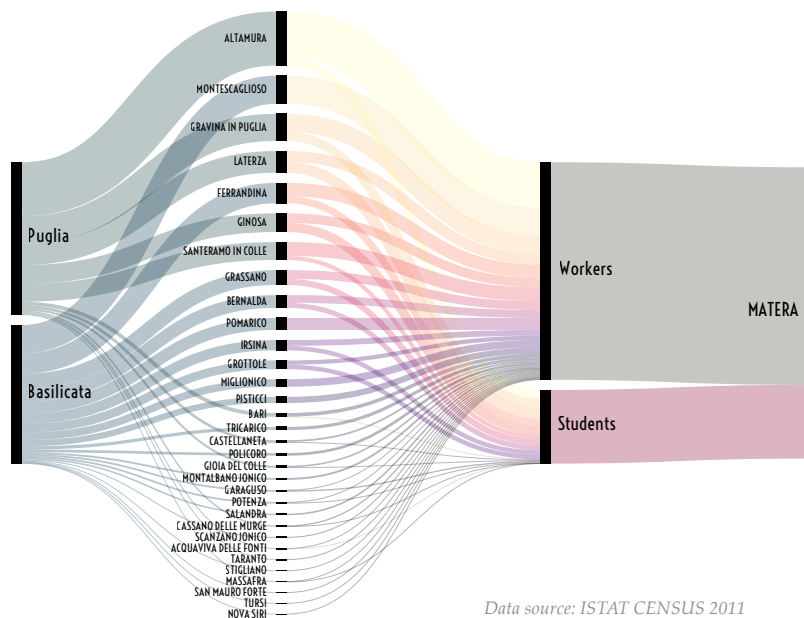
Exposed population must include not only the resident population, but in general the population present temporarily or occasionally, namely the commuters (Figure 6.19) and tourists who enter and leave the municipal territory every day for different reasons.

Flood can affect also transport links and commuter routes through the town.



Data source: ISTAT CENSUS 2011

(a) Mapping of the commuting flows



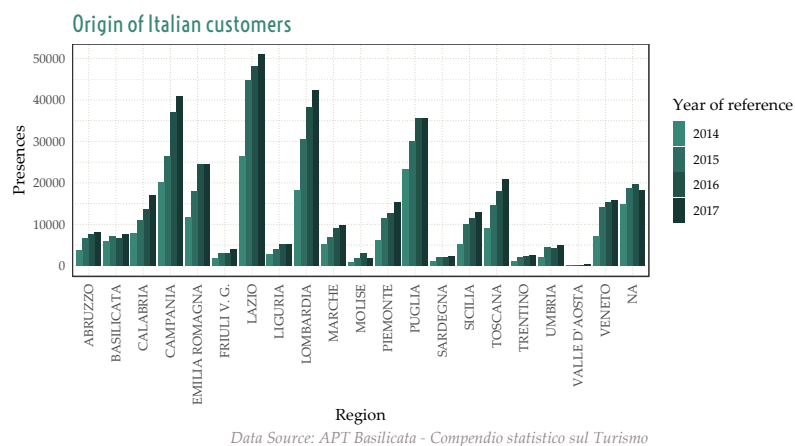
Data source: ISTAT CENSUS 2011

(b) Main flows stratified by origin and reason

Figure 6.19: Commuting flow towards Matera

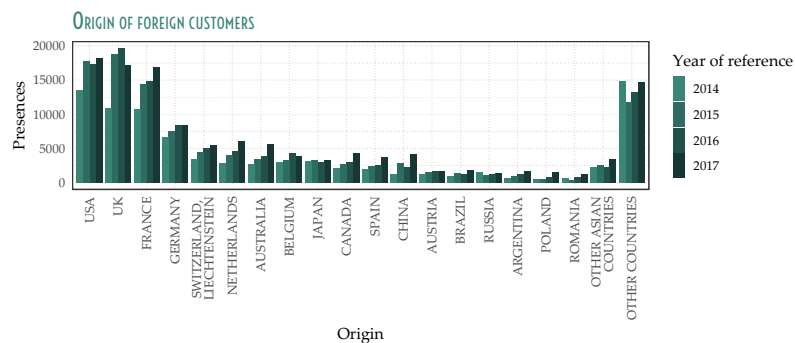
Matera, since its nomination and acquisition of the title of European Capital of Culture in 2019, has experienced a constant rise in both international and domestic tourism (Figure 6.20). The popular viewpoints and main attractiveness points are concentrated in the Sassi area. The significant presence of tourists in the town's territory can lead to the doubling of the population at certain times of the year.

The presence of tourist from different part of the World increases the population exposed at the risk and requires a simple, iconographic and/or multilingual communication targeted at users with little or no knowledge of the territorial and historical context.



Data Source: APT Basilicata - Compendio statistico sul Turismo

(a) Domestic tourism



Data Source: APT Basilicata - Compendio statistico sul Turismo

(b) International tourism

Figure 6.20: Touristic flows towards Matera.

The surveys concerned not only the population but also the state, type of use and of utilization of the building heritage. Buildings and buildings complex definitions include constructions containing spaces permanently destined for use by people as living space and/or for the production of goods and services.

A building or buildings complex (Figure 6.21) is classified as *used* if is used totally or partially for residential and/or goods and services production purposes at the census reference period, but also when it is ready to be used, even if not actually used. Otherwise, is classified as *not used* if is not ready yet (e.g. under construction) or doesn't fit residential and/or production needs because in a state of decay.

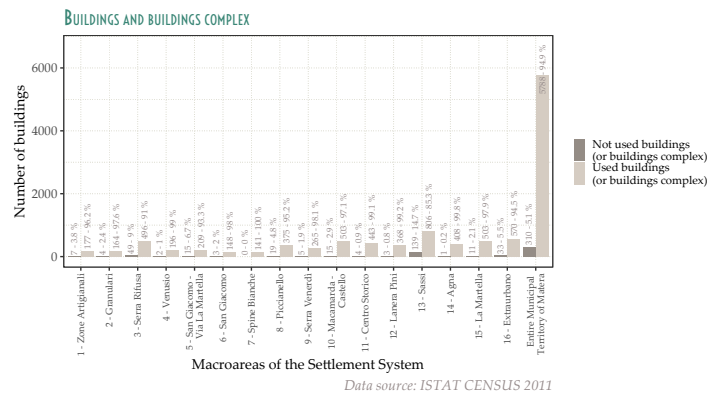


Figure 6.21: Utilized buildings.

The type of use of buildings and buildings complex construction of the building in function of the destination which it was made for; residential buildings may have a consistent part occupied by offices and other economic activities that, during the time, have taken place in a structure built for residential purposes; it is, also, possible to have conventional dwellings in structures designed for non-residential purposes, as institutional households, hotels, etc.

The residential building (Figure 6.22) classification includes: buildings designed, constructed and used exclusively for residential purposes (such as detached houses, villas, cottages, terraced houses, etc.); buildings designed, constructed and used mainly for residential purposes (such as multi-apartment buildings or apartment blocks with shops at street level, etc.); buildings that, though not originally designed and constructed for residential purposes, over time changed use becoming residential; a building which, though originally designed and constructed for residential purposes, over time changed use becoming no longer a residential building (e.g. a very common case in Matera is a residential building which has become a *Bed & Breakfast* activity). Types of use of a building are: *residential* (used mainly for residential purposes), *production* (industry, handicraft, agriculture, general production), *commercial* (retail, wholesale, public

stores), *business district/tertiary* (public and private administrative offices, financial districts, insurance companies and representative offices), *tourist/receptive* (tourist residences, hotels, convention centers, health spa, camping areas), *services* (services to person: cultural, social, health, welfare and hospital services, sport facilities, education, technological systems, public parking lots, fairs/exhibitions, park areas/gardens; services to community: barracks, prisons, etc.), *other* (religious institutions, churches, etc.).

The construction materials and methods of construction (Figure 6.23), the period of construction (Figure 6.24), the state (Figure 6.25), layouts and facade finishing play an important role in determining the potential for exposure to floodwater and resilience against floods.

The number of the floors of a building includes the basement and the ground floor (Figure 6.26).

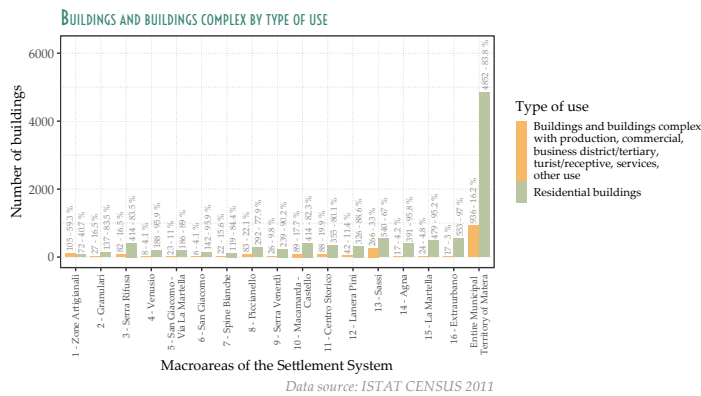


Figure 6.22: Buildings and buildings complex by type of use.

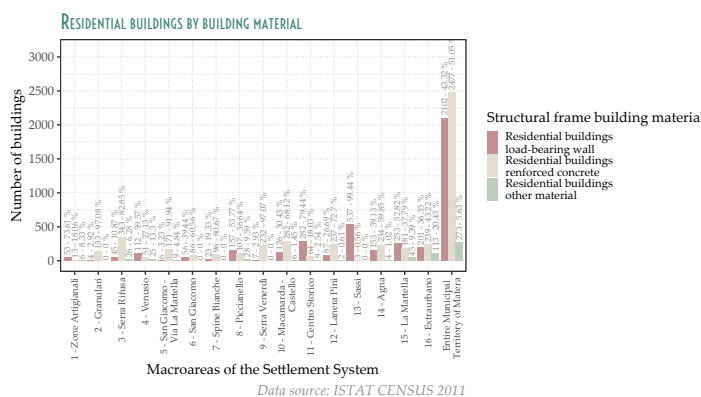


Figure 6.23: Residential buildings by structural frame building material.

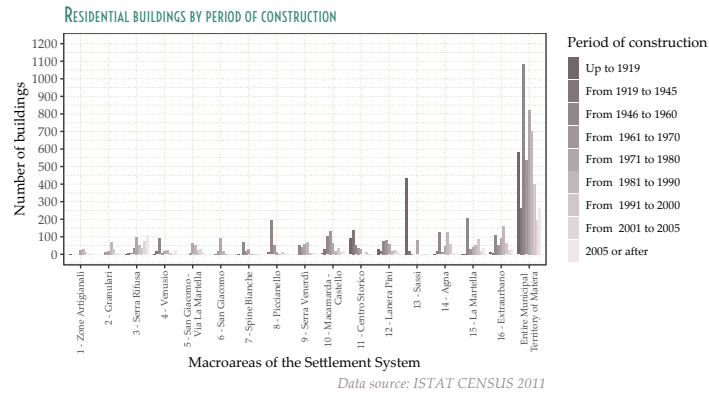


Figure 6.24: Residential buildings by period of construction.

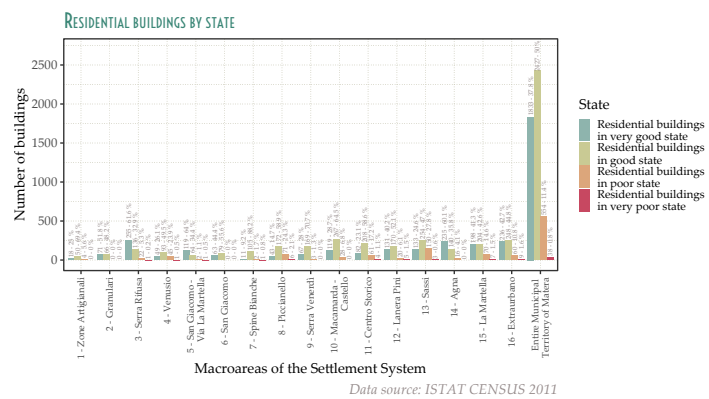


Figure 6.25: Residential buildings by state.

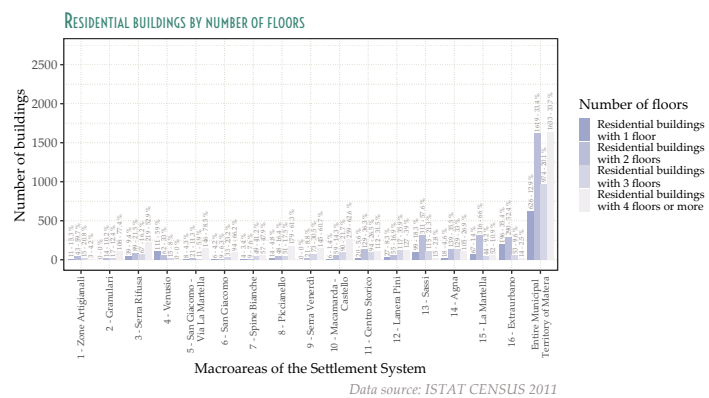


Figure 6.26: Residential buildings by number of floors

6.3 CRITICAL POINTS - PAST FLOOD EVENTS

In the last decade, the city suffered from urban flooding due to the landscape assets that cannot manage rainfall. The urban morphology evolution, the surfaces, and topographic characteristics, as well as the climatic context, increase the proneness and the susceptibility to pluvial floods, caused by heavy precipitation on a local scale and having disastrous impacts (see Figure 1.5).

In the absence of a rigorous systematic catalog of urban flood events, a data collection was carried out to ascertain the past heavy precipitation effects and map the zones most hit by past flooding. Observations (mainly photographs and video), stakeholders testimonials, and disaster reports were collected from several secondary sources: national press, local press, and *social media* searching inherent keywords in Italian and English. Using such information and available pluviometric data obtained from the Decentralized Functional Center of Basilicata (Centro Funzionale Decentrato Basilicata, Protezione Civile Basilicata n.d.), shown in Figure 6.27, it was possible to select a sample of past flood events. There were no available precipitation data for the event of 27 March 2015.

Several zones of Matera urban settlement appeared particularly prone to severe precipitation related risk. The observations were consistent with the simulation of urban pluvial flood conducted with a modified FLORA2D (Cantisani et al. 2014) model by Mancusi et al. (2019) and were used to delineate the historical context for the development of the web prototyping tool for flood risk communication at local scale presented in Section 6.7.

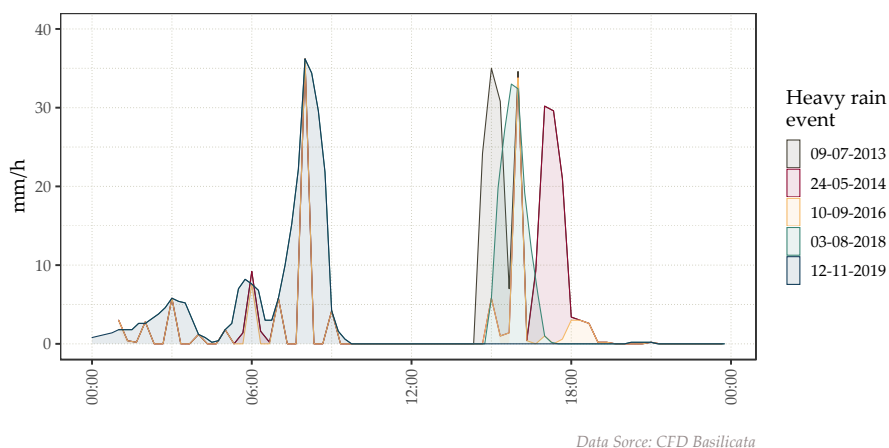
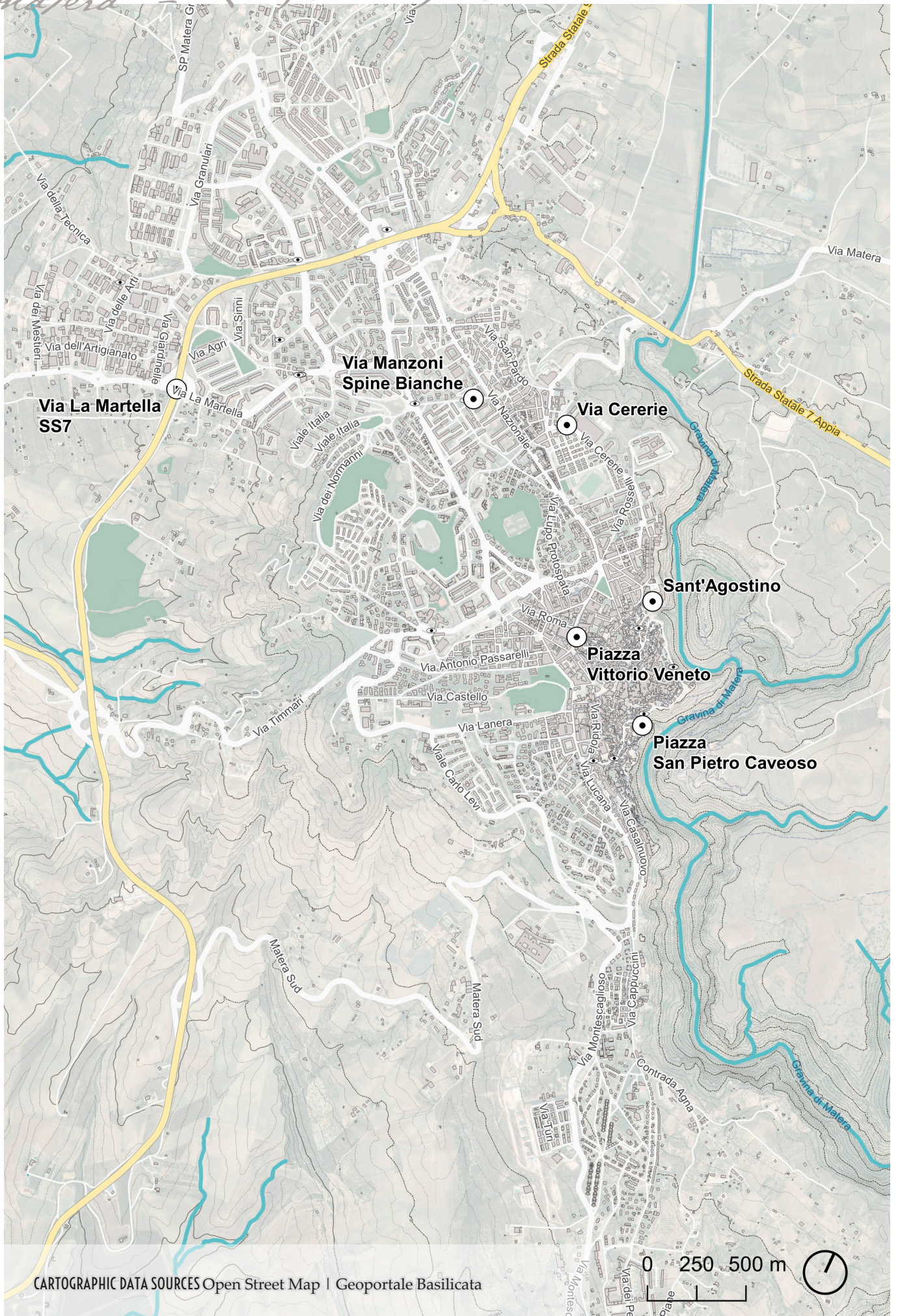


Figure 6.27: Precipitation data for past flood events: 1-hour accumulated rainfall in Matera.



CRITICAL POINT Piazza Vittorio Veneto MACROAREA Sassi VIEW POINT 40°39'58"N 16°36'22"
DATA SOURCE Google Earth | Google street view | muymatera.it | Facebook | <http://www.sassilive.it>



1928



Heavy precipitation event: 12 November 2019

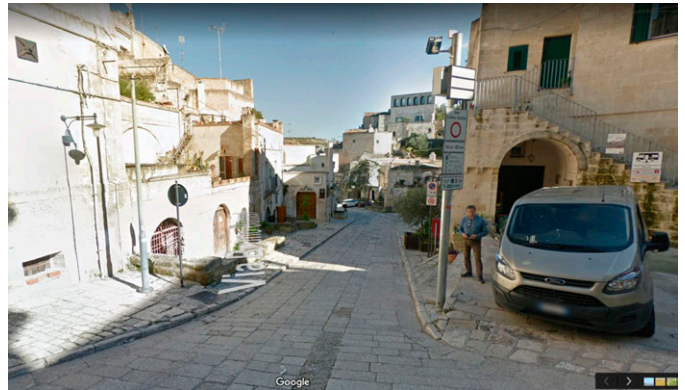


CRITICAL POINT Piazza San Pietro Caveoso MACROAREA Sassi VIEW POINT 40°39'55"N 16°36'46"E
 DATA SOURCE Google Earth | Google street view | Facebook | Twitter | <http://www.sassilive.it> | <https://www.inmeteo.net>



Google Earth
 Imagery Landsat / Copernicus
 Data SRTM30 PLUS, U.S. Navy, NOAA, GEBCO

Heavy precipitation event: 3 August 2018



12 November 2019



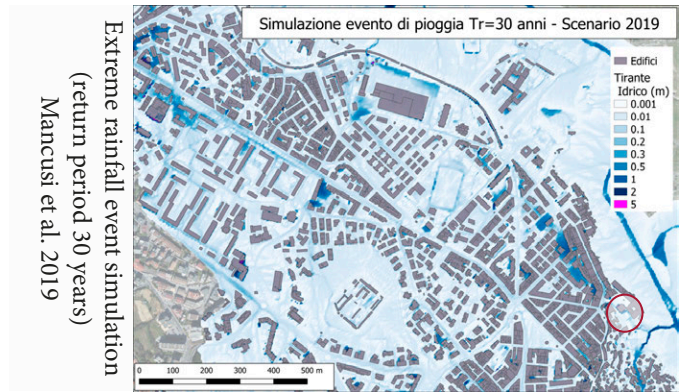
CRITICAL POINT Sant'Agostino - MaCROAREA-Sassi VIEW POINT 40°40'10"N 16°36'41"E
 via Madonna delle Virtù
 DATA SOURCE Google Earth | Google street view | <http://www.meteoweb.eu/> | <http://www.sassilive.it>



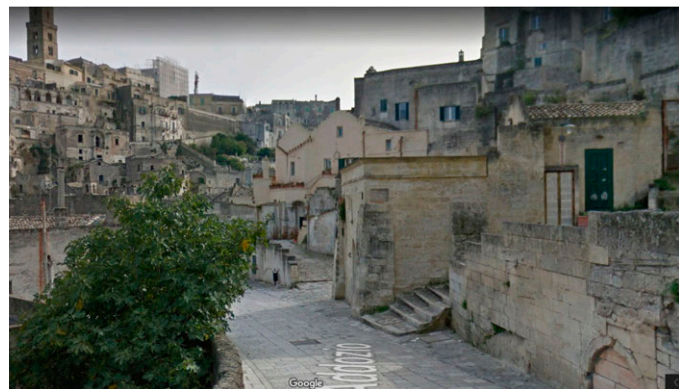
9 July 2013



Heavy precipitation event: 24 May 2014



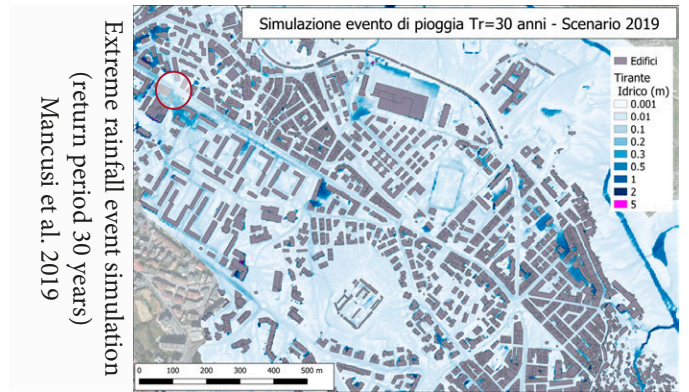
Extreme rainfall event simulation
 (return period 30 years)
 Mancusi et al. 2019



CRITICAL POINT via Manzoni MACROAREA Spine Bianche VIEW POINT 40°40'14"N 16°35'40"E
 DATA SOURCE Google Earth | Google street view | YouTube | <https://www.sassiland.com/>



Heavy precipitation event: 9 July 2013



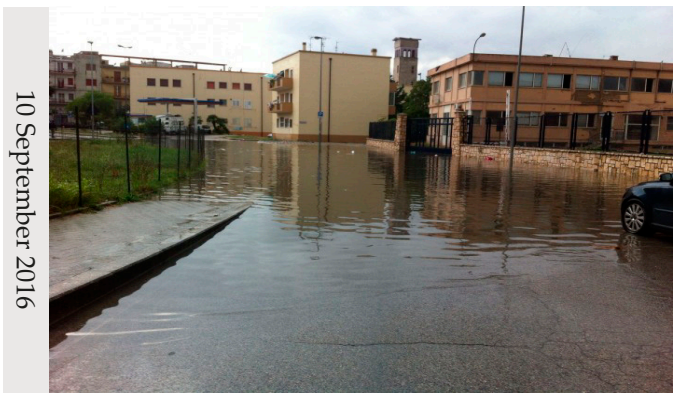
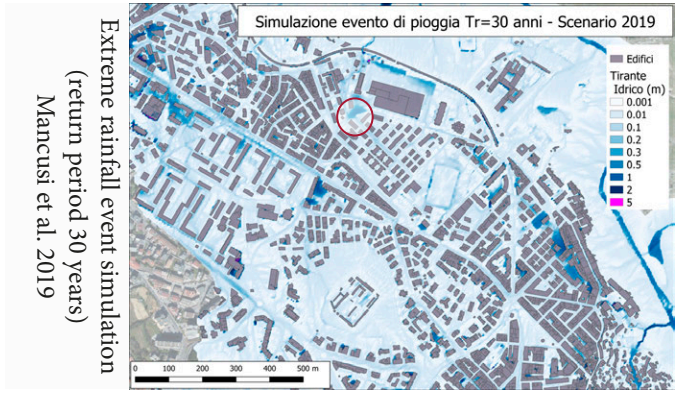
Extreme rainfall event simulation (return period 30 years) Mancusi et al. 2019

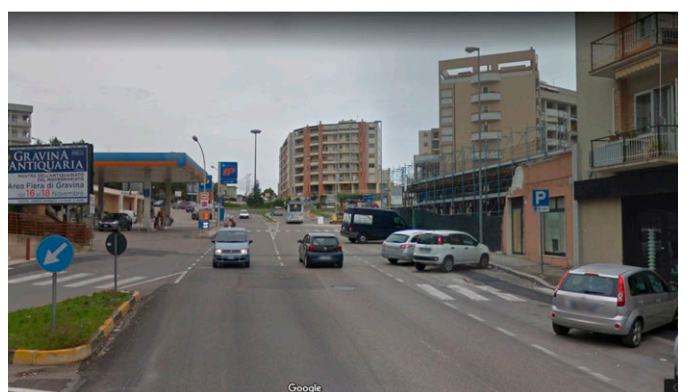
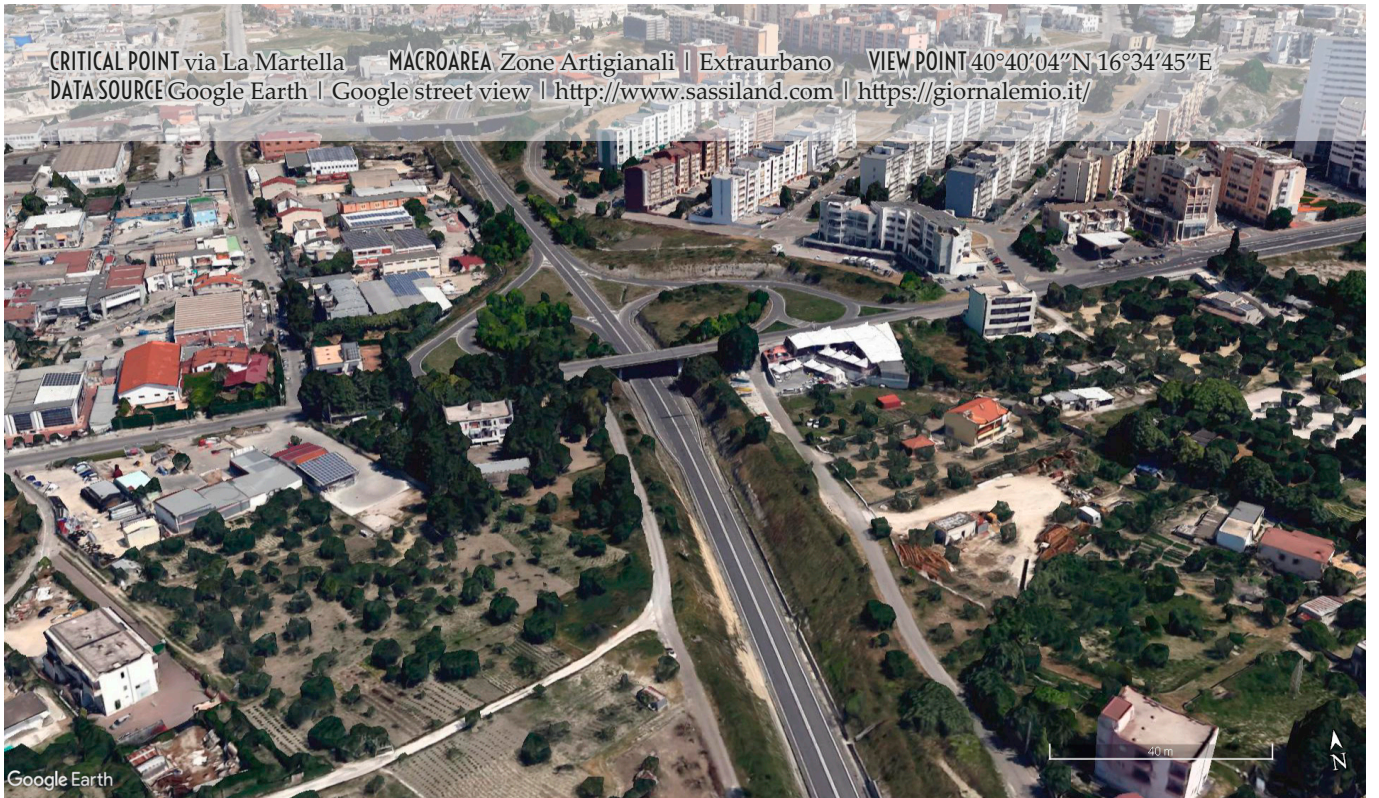


27 March 2015



CRITICAL POINT via Cererie MACROAREA Piccianello VIEW POINT 40°40'31"N 16°36'07"E
 (ex stabilimento Barilla - former Barilla factory)
 DATA SOURCE Google Earth | Google street view | <http://www.sassiland.com> | <https://giornalemio.it/>





6.4 MATERA THERMO-PLUVIOMETRIC DATA

At the present time, the available rainfall and temperature data for the Matera urban area is obtained from measurements of only one weather station located near the boundaries of extra-urban macroarea owned by the Regional Civil Protection (Protezione Civile Basilicata n.d., Table 6.2 and Figure 6.28) .

Address	ISTITUTO PROFESSIONALE
Watershed	BRADANO
Latitude	40° 39' 35" N
Longitude	16° 35' 43" E
Altitude	475 m above sea level



Table 6.2: Matera weather station.



Figure 6.28: Matera weather station location.

Not all observations are continuous: the gaps in the recorded air temperature and hourly precipitation are evident (Figure 6.29).

There is a demand for cost-effective techniques to enhance the availability and size of rainfall data for a proper catchment representation at urban scale.

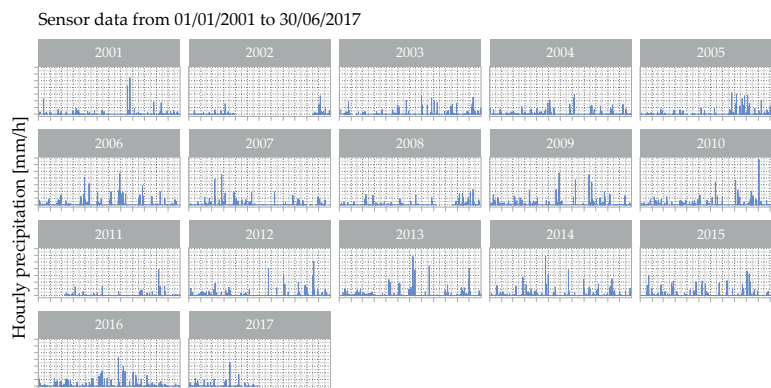
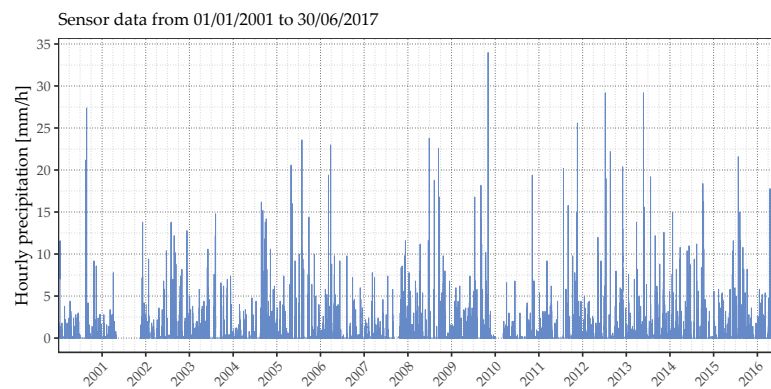
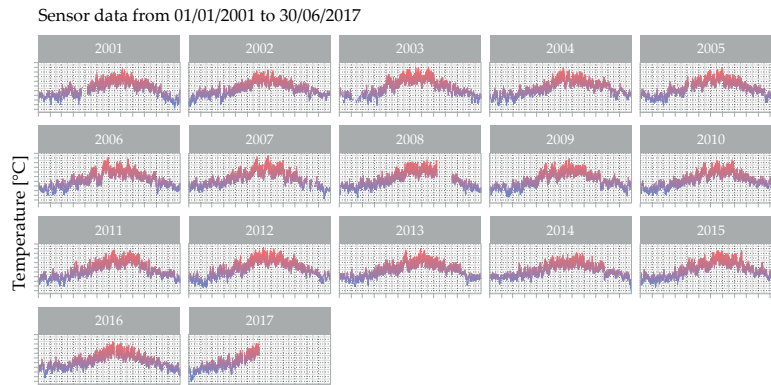
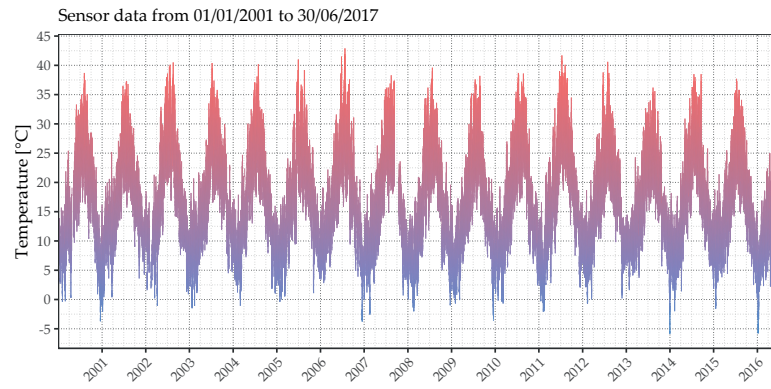


Figure 6.29: Recorded air temperature and hourly precipitation. Data source Protezione Civile Basilicata (n.d.).

6.5 BARI - MATERA 5G PROJECT

The research can benefit from innovative areas in components, systems, networking and web technologies.

The measurement algorithms and data assimilation techniques must be harmonized to improve the rainfall monitoring ability in order to produce a tangible impact on the *smart* management of flood risk.

This can be achieved by increasing the efficiency of operational time in emergency management by reducing latency and enabling real-time.

These goals can be reached by using the latest stage in the evolution of mobile communications: the 5th Generation mobile network (5G) telecommunication standards (Xiang et al. 2017). 5G systems not only provide faster speeds than 4G, but also offer higher capacity, higher density of mobile broadband users, device-to-device communication support, simultaneous connections for wireless sensors, higher spectral and efficiency, lower latency and better coverage. This means that the system suits a wide range of use cases, such as better implementation of the Internet of Things (IoT), as well as broadcast-like (real-time) services and lifeline emergency communication in case of natural disasters.

The *Bari - Matera 5G project: together for the Digital Future*⁵ (Chapter 4) was developed by Telecom Italia S.p.A. (TIM), Fastweb and Huawei, which as a consortium won the call for tenders of the Ministry of Economic Development. The project includes 55 Partners such as Universities and Research Centers, PA and public interest communities, Companies in Puglia and Basilicata, and Industry segment leaders and startups. The project sets the cities of Bari and Matera to become the first “5G cities” in the South testing several innovative services and new technology. The Action Plan (2017-2021) involves network coverage in 10 areas (media - virtual reality, smart port, smart city, smart agriculture, public safety, industry 4.0, health 5.0, mobility - road safety, tourism and culture, environmental monitoring) and service development including 70 examples of use.

⁵ <http://www.barimatera5g.it/>

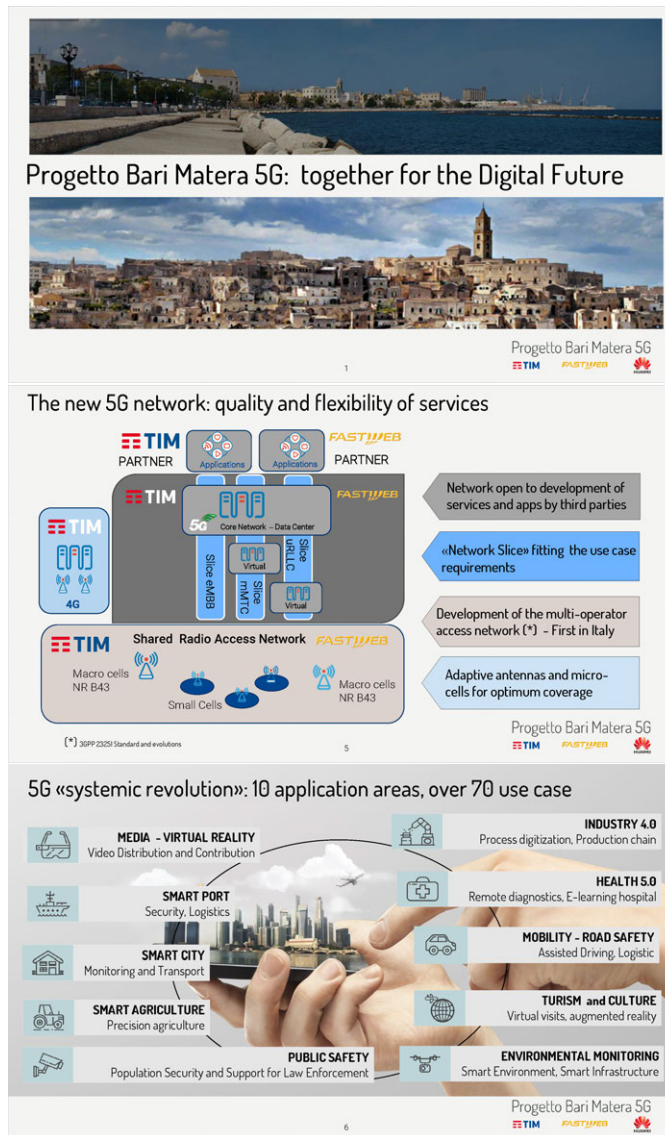


Figure 6.30: Bari - Matera 5G project: together for the Digital Future.

6.6 REAL-WORLD DEPLOYMENT OF THE BINARY MODEL

In order to estimate the skills of the binary classification model proposed in the Chapter 4 in a *real world* unconstrained operational setting, it was built a completely new set of input images. The first test set was obtained from the same sources of the training and validation sets (Table 4.1) so it contained pictures coming from the same sources, representing both natural rain and rain produced in the Large-scale Rainfall Simulator of the NIED.

For the *real world* model deployment, the source of the picture was a Reolink surveillance camera installed by TIM within the

*Bari - Matera 5G project*⁶ without any special setting aimed to enhance the precipitation visibility. In fact the webcam was set for the *Public Safety* case using 5G network connectivity testing (Figure 6.31).

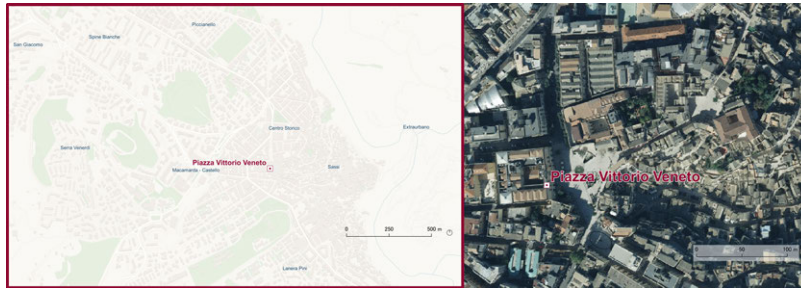


Figure 6.31: TIM Surveillance camera location

The camera frames *piazza Vittorio Veneto* - the main square in the historical center of Matera city - and its hypogeum (Figure 6.32). Being a cultural tourist attraction point, the scene is often populated by moving pedestrians, bicycles, police cars, and service vehicles.



Figure 6.32: Real use case: Surveillance camera framing Vittorio Veneto square and hypogeum.

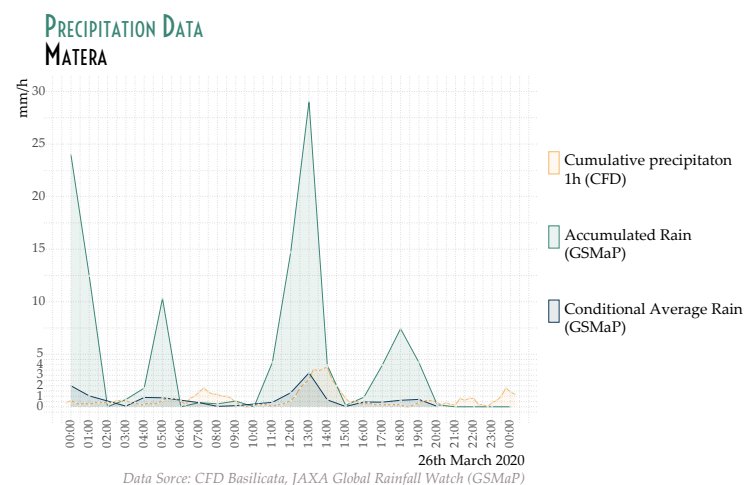
The test set is strongly independent of the training and validation data sets used in Chapter 4, but follows the same balanced probability distribution of the classes. It contains 2360 unseen

⁶ <http://www.barimatera5g.it/>

examples, 1180 instances for the WR class and 1180 for the NR class. The resolution of the color picture was 2560×1920 pixels.

The ground truth was created by labeling manually the pictures that displayed visible precipitation streaks or raindrops and selecting the same number of frames that displayed a clean background, with as many lightning conditions as possible (i.e. with diverse capture time).

The presence of rain was verified with rainfall data collected both from the Japan Aerospace Exploration Agency (JAXA) Global Rainfall Watch - Global Satellite Mapping of Precipitation (GSMaP) Project⁷ (Japan Aerospace Exploration Agency n.d.; K.i. Okamoto et al. 2005; Kubota et al. 2007; Kenichi Okamoto et al. 2008) and the Centro Funzionale Decentrato Basilicata⁸ (Protezione Civile Basilicata n.d.).



(c) Comparison of the precipitation data

Figure 6.33: Data used to verify the manual labeling of images (presence of rain).

⁷ <https://sharaku.eorc.jaxa.jp/GSMaP/>

⁸ <http://www.centrofunzionalebasilicata.it/>

The learned model was used to generate prediction on the test TIM data set (Table 6.3) to validate the preliminary results discussed in the Chapter 4.

	IMAGE	ACTUAL	PREDICTED	ERROR
1	piazza_vittorio_veneto_01_20200313074502.jpg	NR	NR	
2	piazza_vittorio_veneto_01_20200323151537.jpg	NR	NR	
3	piazza_vittorio_veneto_01_20200324101048.jpg	NR	NR	
4	piazza_vittorio_veneto_01_20200314184448.jpg	NR	NR	
5	piazza_vittorio_veneto_01_20200326205100.jpg	WR	WR	
6	piazza_vittorio_veneto_01_20200326222402.jpg	WR	WR	
7	piazza_vittorio_veneto_01_20200324104733.jpg	NR	NR	
8	piazza_vittorio_veneto_01_20200326195802.jpg	WR	NR	<—
9	piazza_vittorio_veneto_01_20200326070617.jpg	WR	WR	
10	piazza_vittorio_veneto_01_20200326095658.jpg	WR	NR	<—
11	piazza_vittorio_veneto_01_20200313052720.jpg	NR	NR	
12	piazza_vittorio_veneto_01_20200323080858.jpg	NR	NR	
13	piazza_vittorio_veneto_01_20200326211701.jpg	WR	WR	
14	piazza_vittorio_veneto_01_20200326014951.jpg	WR	WR	
15	piazza_vittorio_veneto_01_20200326013750.jpg	WR	WR	
16	piazza_vittorio_veneto_01_20200313063735.jpg	NR	NR	
17	piazza_vittorio_veneto_01_20200326024851.jpg	WR	WR	
18	piazza_vittorio_veneto_01_20200326195003.jpg	WR	WR	
19	piazza_vittorio_veneto_01_20200313093527.jpg	NR	NR	
20	piazza_vittorio_veneto_01_20200326123612.jpg	WR	NR	<—

Table 6.3: Predicted classification on a sample of 20 pictures from the test TIM data set.

To assess the quality of the predictions on new pictures, the confusion matrix was constructed over the entire test set.

The confusion matrix, reported in Table 6.4, opposes instances in a predicted class (model response) against instances in an actual class. The correct predictions represented by values in the diagonal of the matrix while the prediction errors are located outside the diagonal.

Given the WR label (presence of rain) as the positive class and NR (absence of rain) as the negative class, it was counted the number of TP, FP, TN and FN to calculate the useful metrics.

		REFERENCE	
		Positive = WR	Negative = NR
PREDICTION	Positive = WR	884 of TP	97 of FP
	Negative = NR	296 of FN	1083 of TN

Table 6.4: Confusion matrix for the binary classification problem - TIM dataset

The accuracy value, with p-value equal to 4×10^{-14} , and the loss of entropy were computed on the TIM image set and compared to the previous binary test set (in brackets) of the Section 4.2.2:

$$\text{Overall accuracy} = \frac{(TP + TN)}{(TP + FP + FN + TN)} = 83.35\% (85.28\%)$$

Reference values: worst=0, best=100.

$$\begin{aligned} \text{Cross Entropy} &= - \sum_{i=1}^{C'=2} t_i \log(s_i) \\ &= -t_1 \log(s_1) - (1 - t_1) \log(1 - s_1) \\ &= 0.3960878 (0.3400635) \end{aligned}$$

Reference values: perfect ≈ 0 , good < 0.69 , bad ≥ 0.69 .

Both TIM image set and binary test set share a significant outcome. The metrics values were similar to that obtained in the Section 4.2.2, exhibiting a rather high reliability of prediction made by the model (Chicco and Jurman 2020; Zheng 2015; Murphy 2012; McHugh 2012).

$$\text{Sensitivity} - \text{Recall} = \frac{TP}{(TP + FN)} = 74.92\% (90.44\%)$$

Reference values: worst=0, best=100.

$$\text{Specificity} = \frac{TN}{(FP + TN)} = 91.7\% (80.13\%)$$

Reference values: worst=0, best=100.

$$\text{Precision} = \frac{TP}{TP + FP} = 90.11\% (81.98\%)$$

Reference values: worst=0, best=100.

$$\begin{aligned}
F1 &= \frac{(1 + \beta^2) \times precision \times recall}{(\beta^2 \times precision) + recall} \\
&= \frac{2 \times precision \times recall}{precision + recall} \\
&= 0.8181 (0.8600)
\end{aligned}$$

Reference values: worst=0, best=1 ($\beta = 1$).

$$\begin{aligned}
Cohen's\ kappa = k &= \frac{p_o - p_e}{1 - p_e} = 1 - \frac{1 - p_o}{1 - p_e} \\
&= 0.6669 (0.7057)
\end{aligned}$$

Reference values:

- $\kappa \leq 0$ indicates no agreement;
- $0.01 < \kappa < 0.20$ indicates no to slight agreement;
- $0.21 < \kappa < 0.40$ indicates fair agreement;
- $0.41 < \kappa < 0.60$ indicates moderate agreement;
- $0.61 < \kappa < 0.80$ indicates substantial agreement;
- $0.81 < \kappa < 1$ indicates almost perfect agreement

$$\begin{aligned}
MCC &= \frac{TP \times TN - FP \times FN}{\sqrt{(TP + FP)(TP + FN)(TN + FP)(TN + FN)}} \\
&= 0.6766 (0.7094)
\end{aligned}$$

Reference values: worst=-1, best=+1.

Compared to the test results, the model deployed on the TIM camera pictures dis-closes lower sensitivity, $\approx 75\%$, but higher specificity, $\approx 92\%$, and precision, $\approx 91\%$. That means that the pictures marked as relevant instances (WR) were actually relevant, so the alerts are likely to be true. On the other hand, the higher false negative rate may underestimate the pluviometric forcing.

Considering an optimal balance of recall and precision, F1 score is close to the ideal value 1 in both the test evaluation and the experiment evaluation. The model withstood the drastic change in the data sets, as the images were completely new.

Figure 6.34 displays a frame in rainy condition (26th March 2020) and a visual explanation of the CNN binary classification:

the Gradient-weighted Class Activation Mapping (Grad-CAM) (Selvaraju et al. 2016), a heatmap visualizing the input regions considered “important” for predictions by the classifier. It’s interesting to note that the parts of the image judged more *rainy-like* (strongly activated in the Grad-CAM) by the binary model are the portions of the scene obstructed by the raindrops accumulated on the lens of the surveillance camera.

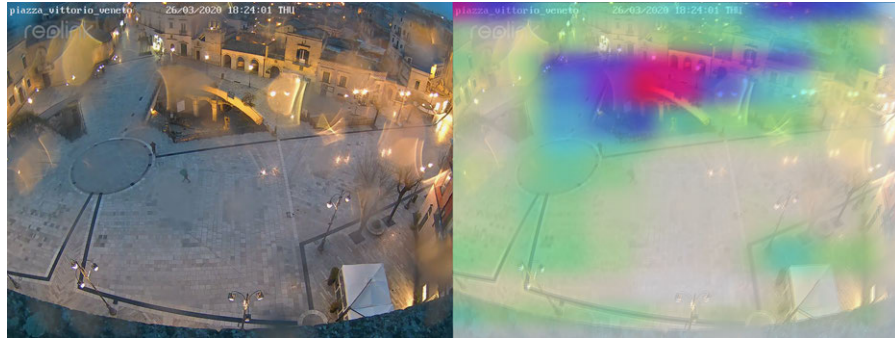


Figure 6.34: Gradient-weighted Class Activation Mapping of a rainy frame of Matera.

To benchmark the code execution performances, the R code was profiled using the Profvis library (Chang and Luraschi 2018). The profiling data were collected on different sample of the data set. The flame graph (Figure 6.35) blocks represent the memory allocated or deallocated in megabytes [Mb] and the time spent in in milliseconds [ms] for a given call stack: libraries loading, model loading and compiling, prediction and evaluation.

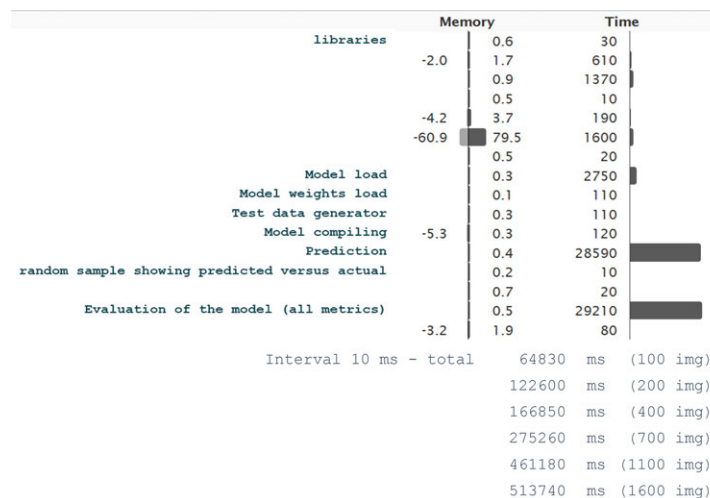


Figure 6.35: Algorithm profiling: the model applied on pictures of a real event in Matera.

The results of the model deployment on the real use case were encouraging for the binary classification problem that detects the presence or the absence of liquid precipitation.

The experimentation on a real world scenario raises the possibility that the use of real rain images can help in setting up a monitoring and warning system of the pluviometric forcing.

6.7 MATEERA: A WEB PROTOTYPING TOOL FOR FLOOD RISK COMMUNICATION AT LOCAL SCALE

MATera Extreme Events Resilience and Awareness (MATEERA) is a web prototyping tool for flood risk communication at local scale developed within the *Environmental Monitoring and Natural Risk Management* use case of *Bari - Matera 5G project* (Framework agreement: *Accordo quadro per la fornitura di progetti di ricerca stipulato tra Università degli studi della Basilicata e Telecom Italia S.p.A. di durata quadriennale nell'ambito della sperimentazione della rete 5G Bari- Matera*), working group: Aurelia Sole, Raffaele Albano, Vincenzo Scuccimarra, Nicla Maria Notarangelo and Nunzia Laguardia.

The MATEERA logo (Figure 6.36) was designed as a combination of visual and verbal elements: the unique Matera skyline, the drop shape (modeled on the aforementioned *Mu 765 G* sculpture by Azuma) and an exclamation mark to create a very simple and easily rememberable image that can leave a comprehensible impression on the observer. The used symbols are commonly understandable: the skyline recalls the specificity of the Matera study case, the water drop symbolizes the heavy rainfall, and the exclamation mark is widely adopted in many contexts to draw attention to warnings of danger, hazards, or precaution.



Figure 6.36: MATera Extreme Events Resilience and Awareness - logo.

The European Floods Directive (Section 1.2) states the crucial role played by non-structural measures based on Early Warning Systems in flood risk management. Starting from the theoretic-

cal framework traced in Section 1.3, the prototype MATEERA was developed to model the significant and competing factors influencing urban flood risk induced by rainfall in the city of Matera and to reduce the residual risk by intervening on its components (hazard, vulnerability and exposure), integrating scientific methodology, innovative technology, and user-friendly communication.

The web portal was designed to be a people-centered Early Warning tool for risk communication at local scale entailing:

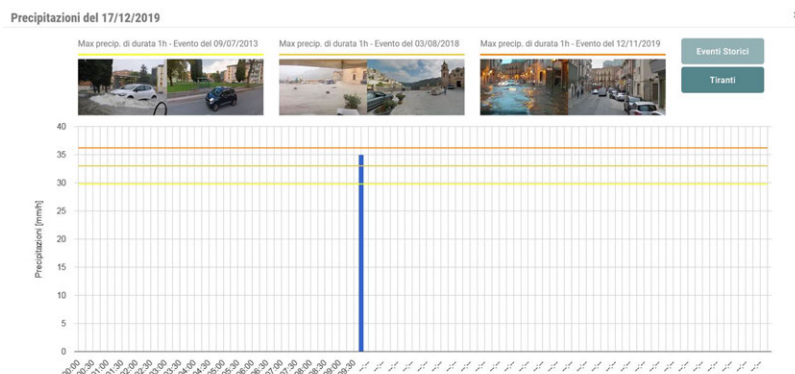
1. Hydro-meteorological forecasting (Protezione Civile Basilicata n.d.);
2. Pluviometric monitoring using cameras (Chapter 4, Chapter 5);
3. Historical events data (Section 6.3), with visual documents to surrogate the “experience of flooding” that increase resilience (Soetanto et al. 2017);
4. Hydrodynamic models to map flood risk at urban scale (Mancusi et al. 2019);
5. Life saving tips - Rules for self-protection in the event of an alarm (Appendix C).

The web-based geographical information system (WebGIS) aims to enhance the flood resilience at a community level, increasing understanding and knowledge, thus enhancing awareness and behavioral response.

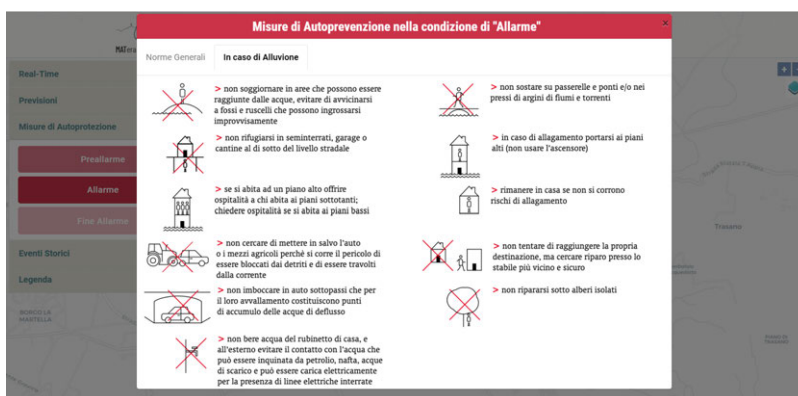
An example of the website functioning is given in Figure 6.37: the past critical observation are indicated with points in different shades of orange, the flood extent and water depth calculated on the basis of the recorded pluviometric level in the sub-catchement recorded by the camera-based gauges and rendered in user-friendly maps (Figure 6.37a); the pluviometric level is compared with past events data (Figure 6.37b); self-protection tips are showed on the basis of the event (Figure 6.37c).



(a) Map of flood extent and water depth calculated on the basis of the recorded pluviometric level in the sub-catchement



(b) Past event data comparison



(c) Self-protection tips in the event of an alarm

Figure 6.37: Screenshots of MATEERA website.

CONCLUSIONS AND FUTURE WORK

In this study, it was proposed a method for near real-time heavy rainfall monitoring at local scale for flood risk mitigation in vulnerable urban and suburban areas.

The general goal was disaster resilience enhancement through a technological evolution of risk prevention.

Benefiting from innovative techniques, the specific aim was to investigate the use of easily available photographing devices as rain detectors-gauges to develop a dense network of low-cost rainfall sensors to support the traditional methods. Using a DL approach based on Transfer Learning with CNN, the rainfall information was gathered from single photographs taken in very generalizable conditions.

The first scenario of interest for supervised learning was a binary classification whose outputs indicated the presence of precipitation: the cameras act as rain detectors. Similarly, the second scenario of interest was a multi-class classification; the multi-class outputs described ranges of quasi-instantaneous rainfall intensity: the cameras act as rain estimators.

The preparation of the classifiers included the preparation of suitable dataset mimicking real-world scenarios: the chosen images were acquired from varying sources both for the binary case (Image2Weather dataset, dashcams in the Tokyo Metropolitan area and experiments in the aforementioned Simulator) and for the multiclass model (dashcams in the Honshu, Shikoku and Kyushu Regions in Japan and experiments in the Simulator).

The presented methods for rainfall detection and rainfall intensity estimation were shown to produce good outcomes encompassing unconstrained verisimilar settings. The results of the tests and the deployment on the real-world scenario were encouraging for both the binary classification and multi-class classification problems. The case study, the city of Matera (Italy), proved the immediate applicability at an operational level of the theoretical variables considered and methodological components chosen. The experimental activities with a pre-existent surveillance camera within the “Bari Matera 5G” project provided a promising perspective on the *smart* environmental monitoring

using 5G connectivity. The binary model reached accuracy and F1 score values of 85.28% and 0.86 for the test, and 83.35% and 0.82 for the deployment. The multi-class model reached test average accuracy and macro-averaged F1 score values of 77.71% and 0.73 for the 6-way classifier, and 78.05% and 0.81 for the 5-class. The best performances were obtained in heavy rainfall and no-rain conditions, whereas the mispredictions are related to less severe precipitation, serving the purpose of monitoring in case of severe rainfall events.

The results achieved surpass the earlier work in this area in terms of flexibility and simplicity of application. As opposed to existing literature, the study focused on maximizing the number of image sources (like smartphones, general-purpose surveillance cameras, dashboard cameras, webcams, digital cameras, etc.), entailing the cases where it is not possible to adjust the camera parameters or obtain shots in timelines or videos.

The proposed approach has limited operational requirements. It used heterogeneous and easily producible input data: the images were acquired from disparate sources in different lighting conditions, without particular requirements in terms of the shooting settings and, since each image is classified independently, the detection doesn't require any sequence or continuous shooting or videos. In comparison with image sequences or video, single images comprise independently the scene information, with a consequent decrease in the amount of data that needs to be processed, stored, and transferred. Once the training phase is over, computational times are extremely reduced. The Convolutional Neural Networks (CNNs) can easily exploit pre-existent devices and be convenient for systems that need to be implemented quickly, yielding a fairly rapid, simple and expeditious solution, easily embeddable in *intelligent devices*.

The system can be managed locally, remotely or *via* cloud by programming electronic devices (such as *smart* cameras or IoT devices) for recording and transmitting the rain data. The model can retrieve rainfall information by processing data collected from different sources located in a fixed place (surveillance cameras) or moving (smartphones, dash-cams, action-cams), contributing to the traditional monitoring networks and forecast systems.

Despite being a prototype, it offers a first operative tool based on artificial vision techniques which can contribute to creating a support sensors network for the characterization of rainfall with

a parsimonious approach in terms of economic and computational resources.

The provided information, whilst being qualitative, can be of practical value for flood early warning systems based on the identification of a meteorological trigger indicator. This approach is especially useful in urban areas where measurement methods such as rain gauges encounter installation difficulties or operational limitations or in contexts where there is no availability of remote sensing data.

This finding can help define novel strategies for meteorological-hydrological studies on a local scale in urban areas: the information can be used in targeted interventions aimed at building-up a hyperlocal information infrastructure integrating low-cost sensor and crowdsourced data that suits the future needs in terms of spatial and temporal resolution, scalability, heterogeneity, and dynamicity.

The major limitation of the proposed approach concerns the approximations inherent in the outputs. Additional data may be gathered to address gaps that are apparent and improve the accuracy of the precipitation intensity prediction. Another limitation can stem from possible ambiguities in the visual appearance of pictures: the system does not suit scenes that are also misleading for human visual perception.

Taken together, the obtained results suggest that using a DL method is an efficient strategy for the CV task of gathering rainfall information using cameras as low-cost sensors and it can be replicated, updated, fine-tuned, and extended in the future.

New technologies and non-conventional data sources offer great potential for engagement and co-production of knowledge to improve the representation of urban precipitation fields to build-up extreme events resilience.

Future directions might be related to the enhancement of the observational capability through an increase in spatial density of rain observations by further experiments and application to crowdsourced pictures of rain acquired with any available device. The results can be incrementally improved through public initiatives such as development of apps, workshops, seminars, hashtag campaigns, etc. Thus, users can become volunteer sensors (Goodchild 2007) and collaborate to generate useful content.

The integration of conventional monitoring networks with *opportunistic sensing* (Dickinson et al. 2010), voluntary geographic information (Goodchild 2007), and crowdsourced data can pro-

mote communication, participation, and dialogue among stakeholders and increase public awareness, emergency response, and civic engagement through the smart city (Riva Sanseverino et al. 2017) and smart community idea.

PART IV

APPENDIX



DIACHRONIC LEGAL FRAMEWORK

An overview of Diachronic Legal Framework in Italy inherent to the field of study is given in the following timeline:

- | | |
|-------------|---|
| 1877 | ROYAL DECREE NO. 3918/1877
<i>Regio Decreto n. 3918/1877</i>
One of the first regulatory interventions regarding specific restrictions for the protection of forests ('forest restriction') |
| 1904 | ROYAL DECREE NO. 523/1904, "CONSOLIDATED ACT OF THE LEGAL PROVISIONS CONCERNING THE HYDRAULIC WORKS OF THE VARIOUS CATEGORIES"
<i>Regio Decreto n. 523/1904 "Testo unico delle disposizioni di legge intorno alle opere idrauliche delle diverse categorie"</i> |
| 1910 | LAW NO. 277/1910
<i>Legge n. 277/1910</i>
Law aimed at purchasing woods and land for the constitution of the State property forest |
| 1911 | Law 13 no. 774/1911
<i>Legge 13 luglio 1911, n. 774</i>
Law containing measures for the hydraulic-forestry arrangement of mountain watersheds, for other hydraulic works and for reclamation |
| 1912 | MINISTERIAL DECREE OF 20 AUGUST 1912 "APPROVAL OF THE RULES FOR THE PREPARATION OF HYDRAULIC-FORESTRY WORKS PROJECTS IN MOUNTAIN BASINS"
<i>Decreto ministeriale 20 agosto 1912 "Approvazione delle norme per la preparazione dei progetti di lavori di sistemazione idraulico-forestale nei bacini montani"</i> |
| 1923 | ROYAL DECREE NO. 3267/1923 "REORGANIZATION AND REFORM OF THE LEGISLATION ON FORESTS AND MOUNTAIN LAND"
<i>Regio Decreto n. 3267/1923 "Riordinamento e riforma della legislazione in materia di boschi e terreni montani"</i>
It limits and regulates the anthropic action in areas subject to hydrogeological restriction |
| 1926 | ROYAL DECREE NO. 1126/1926
<i>Regio Decreto 16 maggio 1926, n. 1126</i>
It identifies the criteria for delimiting the areas subject to restrictions and for issuing authorizations. |
| 1933 | ROYAL DECREE NO. 215/1933
<i>Regio Decreto n.215/1933</i>
It defines the reclamation works to be applied in mountain soils that are damaged from an hydrogeological and forestry point of view. |
| 1933 | CONSOLIDATED ACT NO. 1775/1933 "CONSOLIDATED ACT OF THE PROVISIONS OF LAW ON WATER AND ELECTRICAL SYSTEMS"
<i>Testo Unico n. 1775 /1933"Testo unico delle disposizioni di legge sulle acque e impianti elettrici"</i> |

- 1952 LAW NO. 184/1952 "ORIENTATION PLAN FOR THE PURPOSES OF A SYSTEMATIC REGULATION OF WATER AND ANNUAL REPORT BY THE MINISTRY OF PUBLIC WORKS"
Legge n. 184/1952 "Piano orientativo ai fini di una sistematica regolazione delle acque e relazione annua del Ministero dei lavori pubblici"
- 1962 LAW NO. 11/1962 "IMPLEMENTATION PLAN FOR A SYSTEMATIC REGULATION OF NATURAL WATER COURSES"
Legge n. 11/1962 "Piano di attuazione per una sistematica regolazione dei corsi di acqua naturali"
- 1967 LAW NO. 632/1967 "AUTHORIZATION OF EXPENDITURE FOR THE EXECUTION OF LAND IMPROVEMENT AND DEFENSE WORKS"
Legge n. 632/1967 "Autorizzazione di spesa per l'esecuzione di opere di sistemazione e difesa del suolo"
- 1971 LAW N. 1102/1971
Legge n. 1102/1971
Establishment of the Mountain Communities
- 1972 DECREE OF THE PRESIDENT OF THE REPUBLIC NO. 11/1972
"TRANSFER OF STATE ADMINISTRATIVE FUNCTIONS ON AGRICULTURE AND FORESTS, HUNTING AND FISHING IN INLAND WATERS AND RELATED PERSONNEL AND OFFICES TO THE REGIONS WITH ORDINARY STATUTE"
Decreto del Presidente della Repubblica n.11/1972 "Trasferimento alle Regioni a statuto ordinario delle funzioni amministrative statali in materia di agricoltura e foreste, di caccia e di pesca nelle acque interne e dei relativi personali ed uffici"
- 1977 DECREE OF THE PRESIDENT OF THE REPUBLIC NO. 616/1977
Decreto del Presidente della Repubblica n.616/1977
It transfers to the Regions the competence for activities of hydrogeological accommodation and conservation, forest and woodland maintenance, and the functions related to the determination of the hydrogeological restrictions
- 1989 LAW NO. 183/1989 "RULES FOR THE ORGANIZATIONAL AND FUNCTIONAL REARRANGEMENT OF SOIL DEFENSE"
Legge n. 183/1989, "Norme per il riassetto organizzativo e funzionale della difesa del suolo"
- 1990 DECREE OF THE PRESIDENT OF THE COUNCIL OF MINISTERS OF 23 MARCH 1990 "ACT OF GUIDANCE AND COORDINATION FOR THE PURPOSES OF THE PREPARATION AND ADOPTION OF THE FORECASTING AND PLANNING SCHEMES REFERRED TO IN ART. 31 OF THE LAW 18 MAY 1989, N. 183, CONTAINING RULES FOR THE ORGANIZATIONAL AND FUNCTIONAL REORGANIZATION OF SOIL DEFENSE"
Decreto del Presidente del Consiglio dei ministri 23 marzo 1990 "Atto di indirizzo e coordinamento ai fini della elaborazione e della adozione degli schemi previsionali e programmatici di cui all'art. 31 della legge 18 maggio 1989, n. 183, recante norme per il riassetto organizzativo e funzionale della difesa del suolo"

- 1990 LAW NO. 102/1990 "PROVISIONS FOR THE RECONSTRUCTION AND REBIRTH OF VALTELLINA"
Legge n. 102/1990 "Disposizioni per la ricostruzione e la rinascita della Valtellina"
- 1992 LAW NO. 225/1992 ESTABLISHMENT OF THE NATIONAL CIVIL PROTECTION SERVICE
Legge n. 225/1992 Istituzione del Servizio nazionale della protezione civile"
- 1993 DECREE LAW NO. 398/1993 CONVERTED WITH AMENDMENTS INTO LAW NO. 493/1993 "PROVISIONS FOR THE ACCELERATION OF INVESTMENTS IN SUPPORT OF EMPLOYMENT AND FOR THE SIMPLIFICATION OF BUILDING PROCEDURES" AND, IN PARTICULAR, ART. 12 RELATING TO "PROCEDURES FOR SOIL DEFENSE PLANS"
Decreto Legge n. 398/1993 convertito con modifiche nella legge n. 493/1993 "Disposizioni per l'accelerazione degli investimenti a sostegno dell'occupazione e per la semplificazione dei procedimenti in materia edilizia" ed in particolare, l'art. 12 relativo a "Procedure per i piani di difesa del suolo"
- 1993 DECREE OF THE PRESIDENT OF THE REPUBLIC OF 14 APRIL 1993 "ACT OF GUIDANCE AND COORDINATION FOR THE REGIONS CONTAINING CRITERIA AND PROCEDURES FOR THE PREPARATION OF HYDRAULIC AND FOREST MAINTENANCE PROGRAMS"
Decreto del Presidente della Repubblica del 14 aprile 1993 "Atto di indirizzo e coordinamento alle regioni recante criteri e modalità per la redazione dei programmi di manutenzione idraulica e forestale"
- 1997 LAW NO. 344/1997 "PROVISIONS FOR THE DEVELOPMENT AND QUALIFICATION OF INTERVENTIONS AND EMPLOYMENT IN THE ENVIRONMENTAL FIELD"
Legge n. 344/1997 "Disposizioni per lo sviluppo e la qualificazione degli interventi e dell'occupazione in campo ambientale"
- 1997 LAW NO. 345/1997 "FUNDING FOR WORKS AND INTERVENTIONS OF ROADS, INFRASTRUCTURES, SOIL DEFENSE, AS WELL AS FOR THE SAFEGUARDING OF VENICE"
Legge n. 345/1997 "Finanziamenti per opere e interventi di viabilità, infrastrutture, di difesa del suolo, nonché per la salvaguardia di Venezia"
- 1997 MINISTERIAL DECREE OF FEBRUARY 14, 1997 "TECHNICAL DIRECTIVES FOR THE IDENTIFICATION AND DELIMITATION BY REGIONS AT HYDRAULIC RISK"
Decreto ministeriale del 14 febbraio 1997 "Direttive tecniche per l'individuazione e perimetrazione da parte delle Regioni a rischio idraulico"
- 1998 LEGISLATIVE DECREE NO. 112/1998 "CONFERRAL OF STATE FUNCTIONS AND ADMINISTRATIVE TASKS TO THE REGIONS AND LOCAL AUTHORITIES, IN IMPLEMENTATION OF CHAPTER I OF LAW NO. 59"
Decreto legislativo n. 112/1998 "Conferimento di funzioni e compiti amministrativi dello Stato alle regioni ed agli enti locali, in attuazione del capo I della L. 15 marzo 1997, n. 59"

- 1998 DEGREE LAW NO. 180/1998 (SARNO DECREE)
Decreto Legge n.180/1998 (Decreto Sarno)
 Issued following the hydrogeological event that involved the town of Sarno, in Campania region
- 1998 DEGREE OF THE PRESIDENT OF THE COUNCIL OF MINISTERS OF 29 SEPTEMBER 1998 "GUIDANCE AND COORDINATION ACT FOR THE IDENTIFICATION OF THE CRITERIA RELATING TO THE OBLIGATIONS PURSUANT TO ART. 1, PARAGRAPHS 1 AND 2, OF THE D.L. 11 JUNE 1998, N. 180"
Decreto del Presidente del Consiglio dei ministri del 29 settembre 1998 "Atto di indirizzo e coordinamento per l'individuazione dei criteri relativi agli adempimenti di cui all'art. 1, commi 1 e 2, del D.L. 11 giugno 1998, n. 180"
- 1998 LAW NO. 267/1998 "CONVERSION INTO LAW, WITH AMENDMENTS, OF THE DECREE-LAW 11 JUNE 1998, N. 180, CONTAINING URGENT MEASURES FOR THE PREVENTION OF HYDROGEOLOGICAL RISK AND IN FAVOR OF AREAS AFFECTED BY LANDSLIDES IN THE CAMPANIA REGION"
Legge n. 267/1998 "Conversione in legge, con modificazioni, del decreto-legge 11 giugno 1998, n. 180, recante misure urgenti per la prevenzione del rischio idrogeologico ed a favore delle zone colpite da disastri franosi nella regione Campania"
- 1999 MINISTERIAL DECREE 4 FEBRUARY 1999 "IMPLEMENTATION OF URGENT PROGRAMS FOR THE REDUCTION OF HYDROGEOLOGICAL RISK, REFERRED TO IN ARTICLES 1, PARAGRAPH 2, AND 8, PARAGRAPH 2, OF THE D.L. NO. 180, CONVERTED, WITH AMENDMENTS, BY LAW NO. 267 OF 3 AUGUST 1998
Decreto ministeriale 4 febbraio 1999 "Attuazione dei programmi urgenti per la riduzione del rischio idrogeologico, di cui gli articoli 1, comma 2, e 8, comma 2, del D.L. n°180, convertito, con modificazioni, dalla legge 3 agosto 1998, n°267"
- 1999 DEGREE OF THE PRESIDENT OF THE REPUBLIC NO. 348/1999 "REGULATION CONTAINING TECHNICAL STANDARDS CONCERNING ENVIRONMENTAL IMPACT STUDIES FOR CERTAIN CATEGORIES OF WORKS"
Decreto del Presidente della Repubblica n. 348/1999 "Regolamento recante norme tecniche concernenti gli studi di impatto ambientale per alcune categorie di opere"
- 1999 LEGISLATIVE DECREE NO. 152/1999 "PROVISIONS ON THE PROTECTION OF WATER FROM POLLUTION AND IMPLEMENTATION OF DIRECTIVE 91/271/EEC ON THE TREATMENT OF URBAN WASTE WATER AND DIRECTIVE 91/676/EEC ON THE PROTECTION OF WATER FROM POLLUTION CAUSED BY NITRATES FROM AGRICULTURAL SOURCES"
Decreto legislativo n. 152/1999 "Disposizioni sulla tutela delle acque dall'inquinamento e recepimento della direttiva 91/271/CEE concernente il trattamento delle acque reflue urbane e della direttiva 91/676/CEE relativa alla protezione delle acque dall'inquinamento provocato dai nitrati provenienti da fonti agricole"

- 2000 LAW NO. 365/2000 "CONVERSION INTO LAW, WITH AMENDMENTS, OF THE DECREE LAW 12 OCTOBER 2000, NO. 279, CONTAINING URGENT INTERVENTIONS FOR AREAS AT VERY HIGH HYDROGEOLOGICAL RISK AND IN THE FIELD OF CIVIL PROTECTION, IN FAVOR OF THE AREAS OF THE CALABRIA REGION DAMAGED BY THE HYDROGEOLOGICAL CALAMITIES OF SEPTEMBER AND OCTOBER 2000"
Legge n. 365/2000 "Conversione in legge, con modificazioni, del decreto legge 12 ottobre 2000, n. 279, recante interventi urgenti per le aree a rischio idrogeologico molto elevato ed in materia di protezione civile, nonché a favore delle zone della regione Calabria danneggiate dalle calamità idrogeologiche di settembre ed ottobre 2000"
- 2000 EUROPEAN DIRECTIVE NO. 2000/60
Direttiva europea n. 2000/60
establishing a framework for Community action in the field of water policy
- 2004 DECREE OF THE PRESIDENT OF THE COUNCIL OF MINISTERS OF 27 FEBRUARY 2004 "OPERATIONAL GUIDELINES FOR THE ORGANIZATIONAL AND FUNCTIONAL MANAGEMENT OF THE NATIONAL, STATE AND REGIONAL ALERT SYSTEM FOR HYDROGEOLOGICAL AND HYDRAULIC RISK FOR CIVIL PROTECTION PURPOSES"
Decreto del Presidente del Consiglio dei ministri del 27 febbraio 2004 "Indirizzi operativi per la gestione organizzativa e funzionale del sistema di allertamento nazionale, statale e regionale per il rischio idrogeologico ed idraulico ai fini di protezione civile"
- 2006 LEGISLATIVE DECREE NO. 152/2006 "CONSOLIDATED ACT OF THE ENVIRONMENT"
Decreto legislativo n. 152/2006 "Testo unico dell'ambiente"
establishing the general principles and competences of the State, the Regions, Autonomous Provinces, the District Basin Authorities and defines the objectives and contents of the Basin Plans, the Hydro-geological Stability Plan (PAI) and the three-year programs of intervention
- 2007 EUROPEAN DIRECTIVE NO. 2007/2 ESTABLISHING AN INFRASTRUCTURE FOR SPATIAL INFORMATION IN THE EUROPEAN COMMUNITY (INSPIRE)
Direttiva europea n. 2007/2, che istituisce un'Infrastruttura per l'informazione territoriale nella Comunità europea (Inspire)
- 2007 EUROPEAN DIRECTIVE NO. 2007/60 ON THE ASSESSMENT AND MANAGEMENT OF FLOOD RISKS
Direttiva europea n. 2007/60, relativa alla valutazione e alla gestione dei rischi di alluvioni
- 2008 EUROPEAN REGULATION NO. 1205/2008
Regolamento europeo n. 1205/2008
It establishes the requirements for creation e updating of metadata for spatial data sets

- 2010 | LEGISLATIVE DECREE NO. 32/2010 "IMPLEMENTATION OF THE INSPIRE DIRECTIVE"
Decreto legislativo n. 32/2010 "Recepimento della direttiva Inspire"
- 2010 | LEGISLATIVE DECREE NO. 49/2010 "IMPLEMENTATION OF DIRECTIVE 2007/60/EC ON THE ASSESSMENT AND MANAGEMENT OF FLOOD RISKS"
Decreto legislativo n. 49/2010 "Attuazione della direttiva 2007/60/CE relativa alla valutazione e alla gestione dei rischi alluvioni"
- 2010 | LEGISLATIVE DECREE NO. 219/2010
Decreto legislativo n. 219/2010
Temporary measures for the implementation of the obligations established by Legislative Decree no. 49/2010: National Basin Authorities (ex. Law 183/1989) and Regions competences
- 2011 | DECREE OF THE PRESIDENT OF THE COUNCIL OF MINISTERS OF 10 NOVEMBER 2011 "TECHNICAL RULES FOR DEFINING THE CONTENT OF THE REPERTOIRE NATIONAL TERRITORIAL DATA, AND THE FORMER METHODS ESTABLISHMENT AND UPDATING OF THE SAME"
Decreto del Presidente del Consiglio dei ministri del 10 novembre 2011 "Regole tecniche per la definizione del contenuto del Repertorio nazionale dei dati territoriali, nonché delle modalità di prima costituzione e di aggiornamento dello stesso"

THE NIED LARGE-SCALE RAINFALL SIMULATOR

To be able to develop, train and test the algorithm that gathers rainfall characteristics using camera as low-cost sensor, the construction of a data-base of images with known rainfall conditions was the essential prerequisite. The data-bases found in the literature do not respond to the desired criteria, in terms of completeness, availability, heterogeneity, rainfall representativeness, known rainfall intensity values, and absence of digitally synthesized rain.

Hence, data were integrated with pictures collected during experimental activities carried out in the Large-scale Rainfall Simulator of the NIED¹ located in Tsukuba, Ibaraki prefecture, Japan (Figure B.1, Figure B.2).



Figure B.1: Aerial view of the National Research Institute for Earth Science and Disaster Resilience 防災科学技術研究所. Google earth V 7.3.3.7786. 36°07'35"N 140°05'23"E. Eye alt 367 m. SIO, NOAA, U.S. Navy, NGA, GEBCO.

Rainfall simulators are one of the most common systems for reproducing natural precipitation phenomena accurately and

1 <https://www.bosai.go.jp/>

precisely. The physical rainfall simulation provides a convenient tool for creating arbitrarily rain events of nominated properties in a controlled way, while varying the parameter of interest (Dunkerley 2008).

The use of rainfall simulators has a relatively long tradition within hydrology and geomorphology fields, for the assessment of hydrologic interactions of rainwater with soils (Lora et al. 2016; Xu et al. 2020), i.e. erosion, infiltration, debris flow, soil erosion, etc.

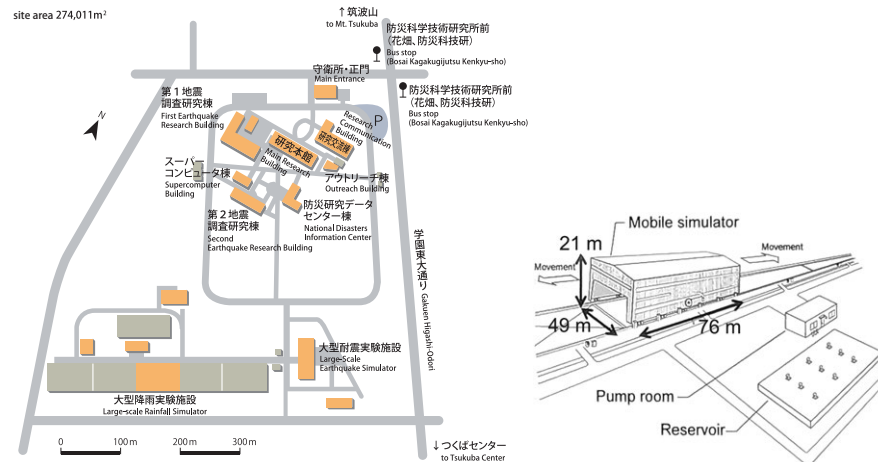


Figure B.2: NIED experimental facilities located in Tsukuba headquarters ©NIED.

The NIED Large-scale Rainfall Simulator was completed in march 1974 and renewed in 2013 (Ishizawa et al. 2014). It is the largest simulator in the world in terms of rainfall area and sprinkling capacity.

The characteristics of this facility, shown in Figure B.3 and Table B.1, offer a systematic tool to develop both small-scale and full-scale physical models to address problems of: hydrogeological processes simulation and measurement, water-related disasters studies (landslides, urban floods, etc.), waterproofing system in construction industry, radars evaluation under heavy rain condition, heavy rain experience educational activities, and so forth.

The leading benefit of using a large scale rain simulator is that it allows experimental tests to be carried out in a relatively short time, reproducing events of different known intensities, including those with a rather remote occurrence frequency, such as rain showers and downpours with time high return period under controlled and repeatable conditions (Figure B.4).

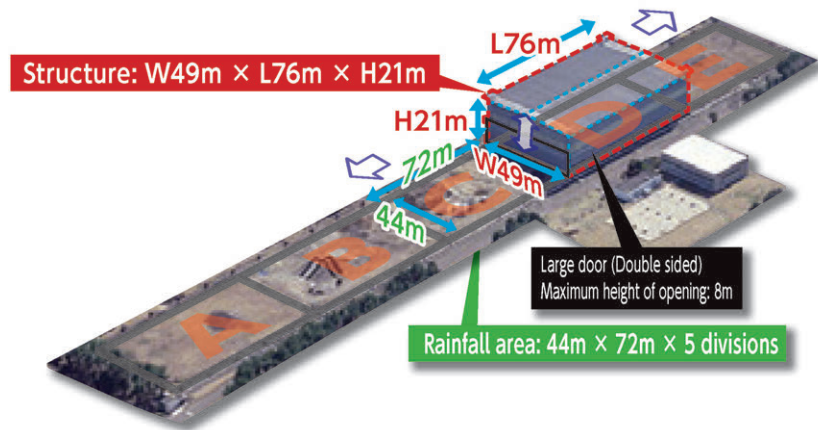


Figure B.3: NIED Large-scale Rainfall Simulator located in Tsukuba (Ibaraki prefecture, Japan) ©NIED.

LARGE-SCALE MOBILE RAINFALL FACILITY	
Structure (area)	Steel-pipe-trussed ferroconcrete (3,492 m ²)
Observation room	Floor 7.5 m above the ground 2 rooms of 65.4 m ² each
Sprinkling area	48×72 m, 5 divisions
SPRINKLING FACILITY	
Raindrop size	0.1 - 2.2 mm diameter [→ improved to 6 mm]
Rainfall intensity	15 - 200 mm/hr [→ improved to 300 mm/hr]
Rainfall area	44×72 m (dividable into quarters)
Nozzles (0.7 - 5.0 kg/cm ²)	System 1 : 15 - 40 mm/hr 544 pcs. System 2 : 30 - 75 mm/hr 544 pcs. System 3 : 60 - 130 mm/hr 544 pcs. System 4 : 100 - 200 mm/hr 544 pcs.
Nozzle height	16 m above the ground
Control	Remote control: flow rate/stress control
Circulating pump	160 kW, 11 kg/cm ² , 5.5 kl/min, 2 pumps
RESERVOIR	
Water storage capacity	2,250 m ³
Pump	Supply well 250 mm diameter, 150 m depth

Table B.1: NIED Large-scale Rainfall Simulator main technical specifications.



Figure B.4: Experiments in the NIED rainfall simulator.

LANDSLIDES AND FLOODS: LIFE SAVING TIPS - RULES FOR SELF-PROTECTION IN THE EVENT OF AN ALARM

Translated and adapted from the brochure created by the PROIDRO Project (*PROfessionisti del monitoraggio ambientale e la sicurezza IDROgeologica* - Environmental monitoring and hydrogeological safety professionals).

Curated by Aurelia Sole, Francesco Sdao

In collaboration with Santina Scarpino

Graphic Design project - art director: Aldo Presta

Icon development: Roberto Gentili, Alessandra Dodaro



Frane e alluvioni. Azioni Norme per l'autoprotezione in caso di allarme salvavita



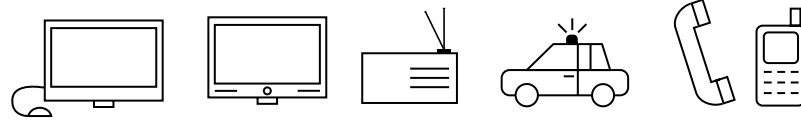
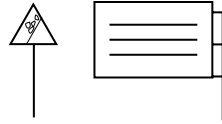
www2.unibas.it/proidro

The brochure was created to promote the culture of prevention, raise awareness among citizens and stimulate their active participation in times of crisis in order to reduce risk.

The tool represents an aid to communicate correct behaviors to be held in the forecast phase and during extreme events of landslides and floods.

The graphic symbol system used is the result of a specific design process within the context of a research of a wider scope which aims to address the implementation of a general and collaborative system of symbols for risk communication, carried out by the University of Basilicata's School of Engineering and the *lacosa studio grafico*.

The underlying assumption is that learning to prevent and reduce the consequences of calamitous events is a task that concerns all: spreading risk information is a collective responsibility to which all the citizens should contribute.



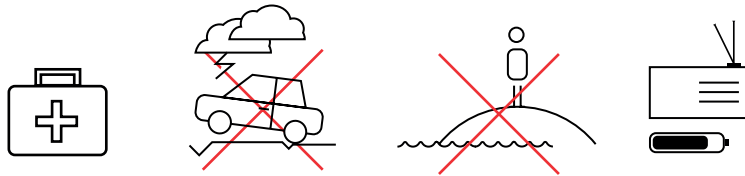
Hydro-geological risk: the importance of being well-informed

Information is one of our most essential tools when dealing with hydro-geological calamitous events. Relevant information is generated at the national and local levels by agencies responsible for systems of alert and response: Functional Centres - Civil Protection Authorities.

In addition to this, the Basin Authority information system outlines in the Hydro-geological Stability Plan (*PAI Piano di Assetto idrogeologico*) the areas at risk of floods and landslides. This plan is available online and, in some cases, complemented by warning signage placed at the affected areas.

The management of the national alert system is ensured by the Department of Civil Protection, the Regions and Autonomous Provinces; the alert system is managed through the network of monitoring centres, as well as the regional organizations and centres of expertise that are frequently called upon to contribute functionally and operationally to this network.

The municipalities are provided with the specific Municipal Emergency Plans, where the risk characteristics are specifically defined, the assembly areas in case of alert, and the response procedure which the administration will implement in the case of a calamitous event.



Reducing the risk: active citizens.

As well as the mechanisms created by relevant authorities, an efficient prevention system also depends on the role performed by individual citizens, who must be sure to behave appropriately in order to avoid, or at least reduce, the impact of extreme events.

It is necessary, therefore, that each citizen assumes an *active* attitude towards this problem, and has the essential information required to activate the main systems of self- protection.

First of all, it is necessary to be familiar with the characteristics of the risks, the locations of the zones at risk of landslides or flooding, and to be aware – where defined – of the arrangements contained within the Municipal Emergency Plan.

Civil Protection drills take place periodically in order to check the status and the efficiency of response and rescue systems. It's possible, and indeed important, for citizens to attend these.

It is also essential to build upon educational activities at school by teaching our own children how to behave in case of emergency, such as staying safe, turning off the gas or calling emergency numbers.



To increase your ability to protect yourself from natural disasters it is necessary to follow these simple rules and implement a few key behaviours



1

Be informed about the Municipal Emergency Plan



2

Own a survival kit containing



3

Keep in reach useful phone numbers



4

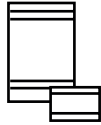
Be informed about the Municipal Emergency Plan

SURVIVAL KIT

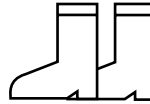
It is always useful to have certain essential items in your house, and to ensure every member of your family knows where they are kept



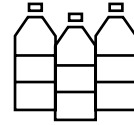
FIRST AID KIT
AND MEDICINES



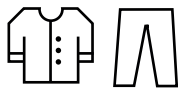
NON-
PERISHABLE
FOOD ITEMS



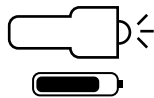
WATER-PROOF
SHOES



STOCKPILE
OF DRINKING
WATER



SPARE SET OF
WARM CLOTHES



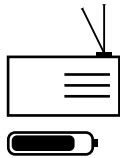
TORCH AND
SPARE BATTERIES



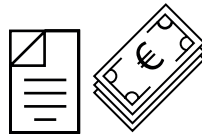
HOUSE KEYS



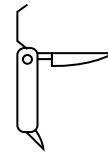
LIGHT
WATERPROOFS
OR OILSKINS



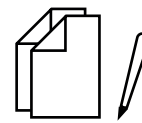
RADIO AND
SPARE BATTERIES



PHOTOCOPIES OF
IDENTITY DOCUMENTS
AND OTHER VALUABLE
DOCUMENTS



UTILITY KNIFE



PEN AND PAPER

USEFUL PHONE NUMBERS

You should always keep at hand up-to-date emergency numbers

Fire Brigade: 115

State Police (Polizia di Stato): 113

European emergency phone number: 112

Medical emergency: 118

Carabinieri's forestry and environment unit: 1515

Civil Protection

(write down the useful numbers for your specific District, Province or Region)

.....

Landslides and floods: What are they?

A landslide is defined as the movement, fast or slow, of a mass of rock, earth or debris down a slope. The main kinds of landslide are as follows: falls, topples, slides (translational or rotational), flows (debris or earth), and lateral spreads.

Landslides are very common in our country due to the area's orographic conditions, geological structure and geomorphology, climate conditions and seismicity.

From a Civil Protection point of view, landslides often lead to significantly dangerous conditions and cause damage to people and to property.

The hazard level is closely linked to the type of movement, its speed, the type and frequency of occurrence of the trigger factors (rain, earthquakes, human activity, etc.) and the volume of landslide material.

Floods are among the most common events of hydro-geological disruption.

An excess of water due to heavy rainfall causes an increase of flow rate in waterways, which overflow or break the embankments and invade the surrounding areas causing damage to buildings, manufacturing activities, traffic networks, agricultural areas, etc.

During and after floods, the water of the river is heavily polluted, carrying floating debris that can injure or stun.

Many Italian hydrographical basins can flood very quickly, even within the space of a few hours; and for this reason it's crucial that the warning is transmitted early enough to allow relevant authorities and agencies operating in the area enough time to implement a response aimed at reducing the exposure of people at risk and limiting damage.

Detection and alert

The Regional and/or National Functional Centre identifies the conditions of a potential risk identifies the conditions of potential risk and notifies the relevant bodies for Critical Regional Warnings (*DPCM February 27th, 2004, G.U 11. 03.2004 n. 59*). The territorial organizations, in accordance with their respective regional laws, then emit communications according to the level of criticality: before the event (pre-alert) or during the event (warning or event in progress) according to the directives of the respective regional laws.

At the municipal level, the Mayor manages the emergency by activating the procedures provided by the Municipal Emergency Plan.

In the pre-alert phase, it is necessary to also implement the procedures for the warning or ongoing event phase, as the difference in danger between the phase of pre-alert and warning or ongoing event, can be minimal and hard to quantify. In fact, all it takes is for the rain to be concentrated in a restricted area for flood phenomena to suddenly occur. The streets can become flooded rivers in their own right, where cars and materials can temporarily obstruct alleys or passages, and can suddenly fail, thereby creating further danger .

Rules for self-protection

> pre-alert phase



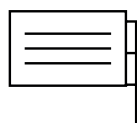
> Consult the website of the Regional Functional Centre or of the Civil Protection. Here, you can find real-time information on the alert levels and the Weather situation.



> Pay attention to information provided by the authorities via radio or TV.



> Pay attention to the loudspeaker announcement broadcast by municipal or Civil Protection vehicles.

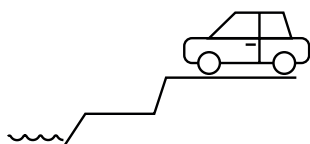


> Check for updates on the light panels, if available.

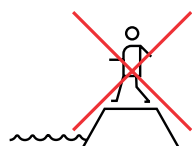
In case of flood



> Prepare flood barriers to protect buildings located on street level. Close and lock the doors of cellars and basements. Secure the movable items located in premises potentially affected by flood (only if you are in conditions of maximum safety).



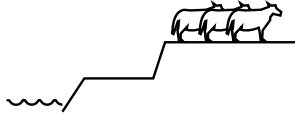
> Secure your own vehicle in an area beyond the reach of floods



> Avoid walking along river banks, even if there are levees.

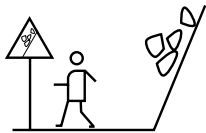


> Do not travel unless absolutely necessary.

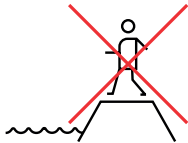


> If you have a farm, bring the flocks and the animals to a high, safe area, close up premises that could be flooded (only if you are in conditions of maximum safety).

In case of landslide



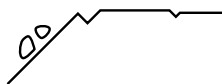
> Move away from areas at risk of landslide, as identified by the Basin Authority in the PAI, or indicated in warning posters.



> Move away from waterways or torrential incisions where rapid mud-flows could occur.



> Avoid passing through or near areas that are at risk of ground movement, especially during storms or heavy rainfall.



> Pay attention to small cracks, fractures and variations in the morphology of the terrain, as they could be precursors for a landslide event.

Rules for self-protection

> warning or event in progress phase



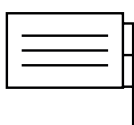
> Consult the website of the Regional Functional Centre or of the Civil Protection. Here, you can find real-time information on the alert levels and the Weather situation.



> Pay attention to information provided by the authorities via radio or TV.



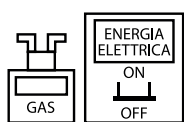
> Pay attention to the loudspeaker announcement broadcast by municipal or Civil Protection vehicles.



> Check for updates on the light panels, if available.



> Do not attempt to secure any property or material goods, and move immediately to a secure location.



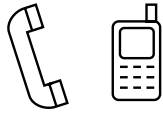
> Prepare flood barriers to protect buildings located on street level. Close and lock the doors of cellars and basements. Secure the movable items located in premises potentially affected by flood (only if you are in conditions of maximum safety).



> Do not travel unless absolutely necessary.



> Help people with disabilities and elderly people to get to a safe location.



> Use your telephone and/or mobile only in cases of actual necessity to avoid overloading the lines.

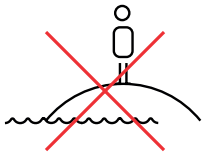


> Stay calm. Avoid to create panic state.

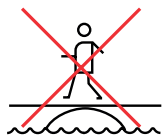


> Make sure that all potentially at risk people are aware of the alarm.

In case of flood



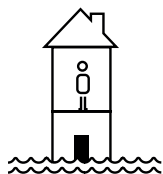
> Do not stay in areas that can be reached by the water, avoid approaching ditches and streams that can suddenly swell.



> Do not stand on walkways or bridges and/or near the banks of rivers or streams.



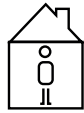
> Do not seek refuge in basements, garages or cellars below street level.



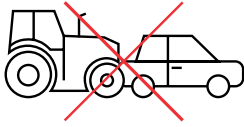
> In case of flooding, find safe shelter moving to the upper floors of your building (do not use the lift).



> If you live on a high floor, offer accommodation to those who live on the lower floors; ask for accommodation if you live on the lower floors.



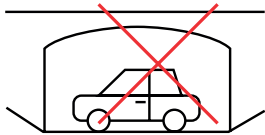
> Stay at home if your house is not at risk of flooding.



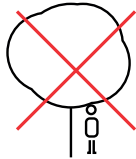
> Do not try to save your car or other vehicle. Rapidly flowing water can knock you off your feet and the debris can block you.



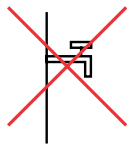
> Do not attempt to get to a certain destination; instead, take shelter in the nearest safe building.



> If travelling by car, do not enter underpasses which can be prone to flooding due to their depressed situation.

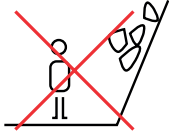


> Do not take shelter under isolated trees.

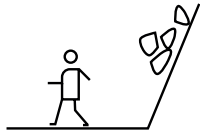


> Do not drink tap water at home, and if outside avoid contact with the water: it could be contaminated with oil, naphtha and sewage or it could have an electric charge due to underground power lines.

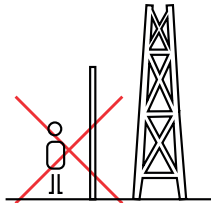
In case of landslide



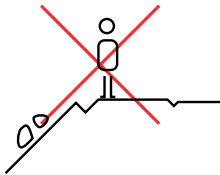
> Do not stand near slopes classified at risk of landslide, as reported by the warning signs.



> Quickly move away from the landslide area paying attention to rolling boulders or bouncing trees that can cause harm.



> Do not stop under poles or pylons: they could collapse or fall



> Do not approach the edge of the landslides as it is unstable.



> If you come across a recently fallen landslide, try to warn any other cars, and alert Civil Protection or the Fire Brigade.

After the emergency

Before leaving safe areas, make sure that it has been officially declared:

The state of emergency is over.

In case of flood

> Avoid contact with water, which can be contaminated with oil, naphtha or sewage. Underground or downed power lines can also electrically charge the water.

> Avoid areas affected by water runoff.

> Do not drive in areas where the water may have receded. Areas where the water has receded can be fragile and susceptible to collapsing under the weight of your vehicle.

> Throw away food that has come in contact with floodwaters.

> Be careful with bathrooms, septic tanks, wells and damaged sewage systems, as these can cause serious risks.

In case of landslide

> Check for injured and trapped persons near the slide, without entering the direct slide area. Direct rescuers to their locations.

> Help people who may need assistance, in particular children, elderly people and people with disabilities.

> Report broken utility - electric, gas and water- lines and damaged roadways and railways to appropriate authorities.

> In case of gas leakage from a building, do not enter the building; check if there is a general gas valve outside the house and if so, turn it off. Report immediately to the Fire Brigade or other specialists.

BIBLIOGRAPHY

- Aerts, J. C. J. H., W. J. Botzen, K. C. Clarke, S. L. Cutter, J. W. Hall, B. Merz, E. Michel-Kerjan, J. Mysiak, S. Surminski, and H. Kunreuther (Mar. 2018). "Integrating human behaviour dynamics into flood disaster risk assessment." en. In: *Nature Climate Change* 8.3, pp. 193–199. ISSN: 1758-678X, 1758-6798. DOI: 10.1038/s41558-018-0085-1.
- Albano, Raffaele and Aurelia Sole (Dec. 2, 2018). "Geospatial Methods and Tools for Natural Risk Management and Communications." In: *IJGI* 7.12, p. 470. ISSN: 2220-9964. DOI: 10.3390/ijgi7120470.
- Allamano, P., A. Croci, and F. Laio (2015). "Toward the camera rain gauge." In: *Water Resources Research* 51.3, pp. 1744–1757. DOI: 10.1002/2014WR016298.
- Autorità di Bacino della Basilicata (2010). *Piano di Gestione del Rischio di Alluvioni (Direttiva 2007/60/CE, D.Lgs. 49/2010, D.Lgs. 219/2010)*. <http://www.adb.basilicata.it/adb/pStralcio/pianoacque.asp>.
- Bell, H and G Tobin (2007). "Efficient and effective? The 100-year flood in the communication and perception of flood risk." en. In: *Environmental Hazards* 7.4, pp. 302–311. ISSN: 17477891. DOI: 10.1016/j.envhaz.2007.08.004.
- Bengio, Yoshua (2012). "Practical Recommendations for Gradient-Based Training of Deep Architectures." en. In: *Neural Networks: Tricks of the Trade*. Ed. by Grégoire Montavon, Geneviève B. Orr, and Klaus-Robert Müller. Vol. 7700. Series Title: Lecture Notes in Computer Science. Berlin, Heidelberg: Springer Berlin Heidelberg, pp. 437–478. ISBN: 978-3-642-35288-1 978-3-642-35289-8. DOI: 10.1007/978-3-642-35289-8_26.
- Bossu, Jérémie, Nicolas Hautière, and Jean-Philippe Tarel (July 2011). "Rain or Snow Detection in Image Sequences Through Use of a Histogram of Orientation of Streaks." In: *International Journal of Computer Vision* 93.3, pp. 348–367. ISSN: 1573-1405. DOI: 10.1007/s11263-011-0421-7.
- Cantisani, Andrea, Luciana Giosa, Leonardo Mancusi, and Aurelia Sole (2014). "FLORA-2D: a new model to simulate the inundation in areas covered by flexible and rigid vegetation." In: *Int. J. Eng. Innov. Technol* 3, pp. 179–186.
- Chang, Winston and Javier Luraschi (2018). *Profvis: Interactive Visualizations for Profiling R Code*. <https://rstudio.github.io/profvis/>.
- Charrière, MKM, SJ Junier, E Mostert, and TA Bogaard (2012). "Flood risk communication: Visualization tools and evaluations of effectiveness." In: "FLOODrisk 2012: The 2nd European Conference on FLOOD-risk Management" *Science, Policy and Practice: Closing the Gap*, Rotterdam, The Netherlands, 20-22 November 2012; Authors version.

- Chicco, Davide and Giuseppe Jurman (Dec. 2020). "The advantages of the Matthews correlation coefficient (MCC) over F1 score and accuracy in binary classification evaluation." en. In: *BMC Genomics* 21.1, p. 6. ISSN: 1471-2164. DOI: 10.1186/s12864-019-6413-7.
- Chollet, Francois and J. J. Allaire (2018). *Deep Learning with R*. 1st. Greenwich, CT, USA: Manning Publications Co. ISBN: 1-61729-554-X 978-1-61729-554-6.
- Chu, Wei-Ta, Xiang-You Zheng, and Ding-Shiuan Ding (2017). "Camera as weather sensor: Estimating weather information from single images." In: *Journal of Visual Communication and Image Representation* 46, pp. 233–249. ISSN: 1047-3203. DOI: 10.1016/j.jvcir.2017.04.002.
- Cohen, Jacob (1960). "A Coefficient of Agreement for Nominal Scales." In: *Educational and Psychological Measurement* 20.1, pp. 37–46. DOI: 10.1177/001316446002000104.
- Covello, Vincent T. (1991). "Risk comparisons and risk communication: Issues and problems in comparing health and environmental risks." In: *Communicating Risks to the Public: International Perspectives*. Ed. by Roger E. Kasperson and Pieter Jan M. Stallen. Dordrecht: Springer Netherlands, pp. 79–124. ISBN: 978-94-009-1952-5. DOI: 10.1007/978-94-009-1952-5_6.
- EM-DAT (2019). *EM-DAT | OFDA/CRED International Disaster Database*. <https://www.emdat.be/>. <https://www.emdat.be/>.
- De Luca, Davide L. and Pasquale Versace (June 2017). "Diversity of Rainfall Thresholds for early warning of hydro-geological disasters." en. In: *Advances in Geosciences* 44, pp. 53–60. ISSN: 1680-7359. DOI: 10.5194/adgeo-44-53-2017.
- de Moel, H., J. van Alphen, and J. C. J. H. Aerts (2009). "Flood maps in Europe - methods, availability and use." In: *Natural Hazards and Earth System Sciences* 9.2, pp. 289–301. DOI: 10.5194/nhess-9-289-2009.
- Di Baldassarre, G., A. Viglione, G. Carr, L. Kuil, J. L. Salinas, and G. Blöschl (2013). "Socio-hydrology: conceptualising human-flood interactions." In: *Hydrology and Earth System Sciences* 17.8, pp. 3295–3303. DOI: 10.5194/hess-17-3295-2013.
- Dickinson, Janis L., Benjamin Zuckerberg, and David N. Bonter (2010). "Citizen Science as an Ecological Research Tool: Challenges and Benefits." In: *Annual Review of Ecology, Evolution, and Systematics* 41.1, pp. 149–172. DOI: 10.1146/annurev-ecolsys-102209-144636.
- Dong, Rong, Juan Liao, Bo Li, Huiyu Zhou, and Danny Crookes (Oct. 2017). "Measurements of rainfall rates from videos." English. In: *2017 10th International Congress on Image and Signal Processing, BioMedical Engineering and Informatics (CISP-BMEI)*. International Congress on Image and Signal Processing, BioMedical Engineering and Informatics, CISP-BMEI 2017 ; Conference date: 14-10-2017 Through 16-10-2017. IEEE, pp. 1–9. DOI: 10.1109/CISP-BMEI.2017.8302066.
- Drdácký, Miloš F. (Oct. 2010). "Flood Damage to Historic Buildings and Structures." en. In: *Journal of Performance of Constructed Facilities*

- 24.5, pp. 439–445. ISSN: 0887-3828, 1943-5509. DOI: 10.1061/(ASCE)CF.1943-5509.0000065.
- Dunkerley, David (2008). "Rain event properties in nature and in rainfall simulation experiments: a comparative review with recommendations for increasingly systematic study and reporting." In: *Hydrological Processes* 22.22, pp. 4415–4435. DOI: 10.1002/hyp.7045.
- Duthon, Pierre, Frédéric Bernardin, Frédéric Chausse, and Michèle Colomb (2016). "Methodology Used to Evaluate Computer Vision Algorithms in Adverse Weather Conditions." In: *Transportation Research Procedia* 14. Transport Research Arena TRA2016, pp. 2178–2187. ISSN: 2352-1465. DOI: 10.1016/j.trpro.2016.05.233.
- Eco, Umberto (1986). *Semiotics and the philosophy of language*. Advances in semiotics. Bloomington: Indiana University Press. ISBN: 978-0-253-20398-4 978-0-253-35168-5.
- Eco, Umberto (2011). *Trattato di semiotica generale*. Italian. Milano: Bompiani. ISBN: 978-88-587-0357-1.
- Einfalt, T., K. Arnbjerg-Nielsen, and S. Spies (Jan. 2002). "An enquiry into rainfall data measurement and processing for model use in urban hydrology." en. In: *Water Science and Technology* 45.2, pp. 147–152. ISSN: 0273-1223, 1996-9732. DOI: 10.2166/wst.2002.0040.
- Einfalt, T., V. Krejci, and W. Schilling (1998). "Rainfall Data in Urban Hydrology." In: *Hydroinformatics Tools for Planning, Design, Operation and Rehabilitation of Sewer Systems*. Ed. by Jiri Marsalek, Cedo Maksimovic, Evzen Zeman, and Roland Price. Dordrecht: Springer Netherlands, pp. 129–168. ISBN: 978-94-017-1818-9. DOI: 10.1007/978-94-017-1818-9_7.
- Elboshy, Bahaa, Shinjiro Kanae, Mona Gamaleldin, Hany Ayad, Toshihiro Osaragi, and Waleed Elbarki (2018). "A framework for pluvial flood risk assessment in Alexandria considering the coping capacity." In: *Environment Systems and Decisions*, pp. 1–18. DOI: 10.1007/s10669-018-9684-7.
- Elhoseiny, M., S. Huang, and A. Elgammal (Sept. 2015). "Weather classification with deep convolutional neural networks." In: *2015 IEEE International Conference on Image Processing (ICIP)*, pp. 3349–3353. DOI: 10.1109/ICIP.2015.7351424.
- Ermini, Ruggero, L. Didio, S. Pascale, and Francesco Sdao (2010). "Infrastrutture idrauliche storiche nella città di Matera." In: *VI RUN 2010*. Matera: Rassegna Urbanistica Nazionale.
- FISRWG (1998). *Stream corridor restoration: principles, processes, and practices*. English. Washington, D.C.: Federal Interagency Stream Restoration Working Group (FISRWG). ISBN: 978-0-934213-59-2.
- Fletcher, T.D., H. Andrieu, and P. Hamel (2013). "Understanding, management and modelling of urban hydrology and its consequences for receiving waters: A state of the art." In: *Advances in Water Resources* 51. 35th Year Anniversary Issue, pp. 261–279. ISSN: 0309-1708. DOI: 10.1016/j.advwatres.2012.09.001.

- Fu, Xueyang, Jiabin Huang, Xinghao Ding, Yinghao Liao, and John Paisley (2016). "Clearing the Skies: A deep network architecture for single-image rain removal." In: *CoRR* abs/1609.02087.
- Fukuzono, Teruki, Teruko Sato, Yukiko Takeuchi, Kenji Takao, Shinya Shimokawa, Isamu Suzuki, Guofang Zhai, G Terumoto, Toshinari Nagasaga, Kami Seo, et al. (2006). "Participatory flood risk communication support system (Pafrics)." In: *A better integrated management of disaster risks: Toward resilient society to emerging disaster risks in megacities*, Eds., S. Ikeda, T. Fukuzono, and T. Sato. TERRAPUB and NIED, pp. 199–211.
- Garg, Kshitiz and Shree K. Nayar (Oct. 2007). "Vision and Rain." In: *International Journal of Computer Vision* 75.1, pp. 3–27. ISSN: 1573-1405. DOI: 10.1007/s11263-006-0028-6.
- Georgakakos, Konstantine P (1995). "Real time prediction for flood warning and management." In: *US-Italy Research Workshop on the Hydrometeorology, Impacts, and Management of Extreme Floods Perugia (Italy)*.
- Goodchild, Michael F. (Nov. 2007). "Citizens as sensors: the world of volunteered geography." en. In: *GeoJournal* 69.4, pp. 211–221. ISSN: 0343-2521, 1572-9893. DOI: 10.1007/s10708-007-9111-y.
- Goodfellow, Ian, Yoshua Bengio, and Aaron Courville (2016). *Deep Learning*. <http://www.deeplearningbook.org>. MIT Press.
- Google Developers (n.d.). *Machine Learning Crash Course | Google Developers*. <https://developers.google.com/machine-learning/crash-course>.
- Grainger, Sam, Feng Mao, and Wouter Buytaert (Nov. 2016). "Environmental data visualisation for non-scientific contexts: Literature review and design framework." en. In: *Environmental Modelling & Software* 85, pp. 299–318. ISSN: 13648152. DOI: 10.1016/j.envsoft.2016.09.004.
- Griffiths, James A. and Shailesh Kumar Singh (2019). "Urban Hydrology in a Changing World." In: *Hydrology in a Changing World: Challenges in Modeling*. Ed. by Shailesh Kumar Singh and C.T. Dhanya. Cham: Springer International Publishing, pp. 73–88. ISBN: 978-3-030-02197-9. DOI: 10.1007/978-3-030-02197-9_3.
- Hagemeier-Klose, M. and K. Wagner (2009). "Evaluation of flood hazard maps in print and web mapping services as information tools in flood risk communication." In: *Natural Hazards and Earth System Sciences* 9.2, pp. 563–574. DOI: 10.5194/nhess-9-563-2009.
- Hassim, Raima and Abdullah Bade (2015). "Taxonomy of rain detection and rain removal techniques." In: *Transactions on Science and Technology* 2.2, pp. 28–35.
- Haurum, Joakim Bruslund, Chris H. Bahnsen, and Thomas B. Moeslund (Aug. 2019). "Is it Raining Outside? Detection of Rainfall using General-Purpose Surveillance Cameras." In: *arXiv:1908.04034 [cs]*. arXiv: 1908.04034.

- Henstra, Daniel, Andrea Minano, and Jason Thistlethwaite (Oct. 2018). *Communicating Disaster Risk? An Evaluation of the Availability and Quality of Flood Maps*. preprint. Dissemination, Education, Outreach and Teaching. DOI: 10.5194/nhess-2018-264.
- Hirano, Kohin and Masayuki Maki (2018). "Imminent Nowcasting for Severe Rainfall Using Vertically Integrated Liquid Water Content Derived from X-Band Polarimetric Radar." In: *Journal of the Meteorological Society of Japan* 96A.0, pp. 201–220. ISSN: 0026-1165, 2186-9057. DOI: 10.2151/jmsj.2018-028.
- Hirano, Kohin, Masayuki Maki, Takeshi Maesaka, Ryohei Misumi, Koyuru Iwanami, and Shuichi Tsuchiya (2014). "Composite rainfall map from C-band conventional and X-band dual-polarimetric radars for the whole of Japan." In.
- IPCC (2012). *Managing the Risks of Extreme Events and Disasters to Advance Climate Change Adaptation. Special Report of Working Groups I and II of the Intergovernmental Panel on Climate Change*. Ed. by Christopher B. Field, Vicente Barros, Thomas F. Stocker, Qin Dahe, David Jon Dokken, Gian-Kasper Plattner, Kristie L. Ebi, Simon K. Allen, Michael D. Mastrandrea, Melinda Tignor, Katharine J. Mach, and Pauline M. Midgley. Cambridge, UK, and New York, NY, USA: Cambridge University Press.
- Ishizawa, Tomohiro, Toru Danjo, and Naoki Sakai (2014). "Performance improvement of sprinkler system by renovation of large rainfall simulator." In: *Proceedings. GeoKanto2014*. (in Japanese). Japanese Geotechnical Society, pp. 2251–2252.
- Istat Istituto Nazionale di Statistica (2011). *Italian National Institute of Statistics*. <https://www.istat.it/en/>.
- Japan Aerospace Exploration Agency (n.d.). *JAXA Global Rainfall Watch (GSMaP)*. <https://sharaku.eorc.jaxa.jp/GSMaP/>.
- Japan Meteorological Agency | *Climate of Japan* (n.d.). <https://www.data.jma.go.jp/stats/data/en/index.html>. (Accessed on 11/17/2020).
- Japan Meteorological Agency (2017). *JMA - Forecast Glossary Rain intensity (in Japanese)*. https://www.jma.go.jp/jma/kishou/known/yougo_hp/amehyo.html.
- Jiang, Shijie, Vladan Babovic, Yi Zheng, and Jianzhi Xiong (2019). "Advancing Opportunistic Sensing in Hydrology: A Novel Approach to Measuring Rainfall With Ordinary Surveillance Cameras." In: *Water Resources Research* 55. DOI: 10.1029/2018WR024480.
- Jones, Douglas and Lawrence A Dean (1953). *A raindrop camera*. text. <http://hdl.handle.net/2142/55366>. Illinois State Water Survey.
- Katre, Ruchi and Nitesh Dodkey (Apr. 2017). "Rain Streaks Detection and Removal in Image based on Entropy Maximization and Background Estimation." In: *International Journal of Computer Applications* 164.11. Place: New York, USA, pp. 17–20. ISSN: 0975-8887. DOI: 10.5120/ijca2017913754.

- Kerrich, John Edmund (Sept. 1946). "An Experimental Introduction to the Theory of probability." en. In: *Nature* 158.4011, pp. 360–360. ISSN: 0028-0836, 1476-4687. DOI: 10.1038/158360c0.
- Khan, Asifullah, Anabia Sohail, Umme Zahoor, and Aqsa Saeed Qureshi (Dec. 2020). "A survey of the recent architectures of deep convolutional neural networks." en. In: *Artificial Intelligence Review* 53.8, pp. 5455–5516. ISSN: 0269-2821, 1573-7462. DOI: 10.1007/s10462-020-09825-6.
- Kidd, Chris, Andreas Becker, George J. Huffman, Catherine L. Muller, Paul Joe, Gail Skofronick-Jackson, and Dalia B. Kirschbaum (Jan. 2017). "So, How Much of the Earth's Surface Is Covered by Rain Gauges?" In: *Bulletin of the American Meteorological Society* 98.1. Publisher: American Meteorological Society, pp. 69–78. DOI: 10.1175/bams-d-14-00283.1.
- Kolte, Ganesh, Ghonge, and P. A. (Jan. 2016). "An Image Processing based Raindrop Parameter Estimation." In: *International Journal of Engineering Trends and Technology* 31.2. Publisher: Seventh Sense Research Group Journals, pp. 73–77. DOI: 10.14445/22315381/ijett-v31p214.
- Kompil, Mert, Jean-Philippe Aurambout, Ricardo Ribeiro Barranco, Ana Barbosa, Cris Jacobs-Crisioni, Enrico Pisoni, Grazia Zulian, Ine Vandecasteele, Marco Trombetti, Pilar Vizcaino, Sara Vallecillo, Filipe Batista e Silva, Claudia Baranzelli, Ines Mari Rivero, Carolina Perpiña Castillo, Chiara Polce, Joachim Maes, Carlo Lavallo, European Commission, and Joint Research Centre (2015). *European cities, territorial analysis of characteristics and trends: an application of the LUISA Modelling Platform (EU Reference Scenario 2013 - Updated Configuration 2014)*. English. Luxembourg: Publications Office. ISBN: 978-92-79-54594-8.
- Kubota, Takuji, Shoichi Shige, Hiroshi Hashizume, Kazumasa Aonashi, Nobuhiro Takahashi, Shinta Seto, Masafumi Hirose, Yukari Takayabu, Tomoo Ushio, Katsuhiro Nakagawa, Koyuru Iwanami, Misako Kachi, and Ken'ichi Okamoto (July 2007). "Global Precipitation Map Using Satellite-Borne Microwave Radiometers by the GSMaP Project: Production and Validation." In: *IEEE Transactions on Geoscience and Remote Sensing* 45.7, pp. 2259–2275. ISSN: 0196-2892. DOI: 10.1109/TGRS.2007.895337.
- Lang, Sue, Lorna Fewtrell, and Jamie Bartram (2001). "Water quality: guidelines, standards, and health: assessment of risk and risk management for water-related infectious disease." In: ed. by Lorna Fewtrell and Jamie Bartram. World Health Organization water series. Geneva: World Health Organization. Chap. Risk communication. ISBN: 978-1-900222-28-0.
- Laureano, Pietro (2009). "Traditional Knowledge and the World Data-bank for Safeguarding Ecosystems." en. In: *The Future of Drylands*. Ed. by Cathy Lee and Thomas Schaaf. Dordrecht: Springer Nether-

- lands, pp. 123–143. ISBN: 978-1-4020-6969-7 978-1-4020-6970-3. DOI: 10.1007/978-1-4020-6970-3_19.
- Laureano, Pietro (2012). *Giardini di pietra: i Sassi di Matera e la civiltà mediterranea*. Italian. 3rd ed. First edition 1993. Torino: Bollati Boringhieri. ISBN: 978-88-339-2293-5.
- LeCun, Yann, Yoshua Bengio, and Geoffrey Hinton (May 2015). “Deep learning.” en. In: *Nature* 521.7553, pp. 436–444. ISSN: 0028-0836, 1476-4687. DOI: 10.1038/nature14539.
- Lichtenberg, Judith and Douglas MacLean (1991). “The role of the media in risk communication.” In: *Communicating Risks to the Public: International Perspectives*. Ed. by Roger E. Kasperson and Pieter Jan M. Stallen. Dordrecht: Springer Netherlands, pp. 157–173. ISBN: 978-94-009-1952-5. DOI: 10.1007/978-94-009-1952-5_9.
- Llasat, Maria-Carmen (2001). “An objective classification of rainfall events on the basis of their convective features: application to rainfall intensity in the northeast of Spain.” In: *International Journal of Climatology* 21.11, pp. 1385–1400. DOI: 10.1002/joc.692.
- Lora, Marco, Matteo Camporese, and Paolo Salandin (May 2016). “Design and performance of a nozzle-type rainfall simulator for landslide triggering experiments.” en. In: *CATENA* 140, pp. 77–89. ISSN: 03418162. DOI: 10.1016/j.catena.2016.01.018.
- Lu, C., D. Lin, J. Jia, and C. Tang (June 2014). “Two-Class Weather Classification.” In: *2014 IEEE Conference on Computer Vision and Pattern Recognition*, pp. 3718–3725. DOI: 10.1109/CVPR.2014.475.
- Macaione, Ina, Antonio Ippolito, Anello Enrico, and Roberto La Gioia (May 2018). “From national disgrace to cultural heritage and international film set. The case of Matera (Italy).” In: *Cities’ Identity Through Architecture and Arts*. Ed. by Anna Catalani, Zeinab Nour, Antonella Versaci, Dean Hawkes, Hocine Bougdah, Adolf Sotoca, Mahmoud Ghoneem, and Ferdinando Trapani. Cham: Routledge, pp. 343–348. ISBN: 978-1-315-16655-1. DOI: 10.1201/9781315166551.
- Macaione, Ina and Armando Sichenze (2013). *Scrivere architettura: multiscale e progetto - Writing architecture: multiscale and design*. Texts in Italian, Chinese, and English. Milano, Italy: FrancoAngeli. ISBN: 978-88-204-3128-0.
- Macherera, Margaret and Moses Chimbari (2016). “A review of studies on community based early warning systems.” In: *Jàmbá: Journal of Disaster Risk Studies* 8.1, p. 11. ISSN: 1996-1421. DOI: 10.4102/jamba.v8i1.206.
- Mahony, Niall O’, Sean Campbell, Anderson Carvalho, Suman Harapanahalli, Gustavo Velasco-Hernandez, Lenka Krpalkova, Daniel Riordan, and Joseph Walsh (2020). “Deep Learning vs. Traditional Computer Vision.” In: *arXiv:1910.13796 [cs]* 943. arXiv: 1910.13796. DOI: 10.1007/978-3-030-17795-9.
- Mancusi, Leonardo, Andrea Abbate, and Raffaele Albano (2019). *State of the art of the hydrogeological hazard mapping regarding the presence*

- of infrastructure of the energy system and a study of urban pluvial flood hazard on a sample basin.* text. Ricerca sul Sistema Energetico – RSE S.p.A.
- Manfreda, Salvatore, Leonardo Mita, Silvano Fortunato Dal Sasso, Francesco Dibernardi, Ruggero Ermini, Maria Mininni, Antonio Bixio, Antonio Conte, and Mauro Fiorentino (June 2016). “La Gestione delle Risorse Idriche nella Città dei Sassi (Matera) - Water Resources Management in the City of Sassi (Matera).” In: *L’Acqua* 3, pp. 39–46.
- Masters, Dominic and Carlo Luschi (Apr. 2018). “Revisiting Small Batch Training for Deep Neural Networks.” In: *arXiv:1804.07612 [cs, stat]*. arXiv: 1804.07612.
- Mays, L. W. (2010). “Lessons from the Ancients on Water Resources Sustainability.” en. In: *Ancient Water Technologies*. Ed. by L. Mays. Dordrecht: Springer Netherlands. ISBN: 978-90-481-8631-0 978-90-481-8632-7. DOI: 10.1007/978-90-481-8632-7.
- McCallum, Ian, Wei Liu, Linda See, Reinhard Mechler, Adriana Keating, Stefan Hochrainer-Stigler, Junko Mochizuki, Steffen Fritz, Sumit Dugar, Miguel Arestegui, Michael Szoenyi, Juan-Carlos Laso Bayas, Peter Burek, Adam French, and Inian Moorthy (June 2016). “Technologies to Support Community Flood Disaster Risk Reduction.” en. In: *International Journal of Disaster Risk Science* 7.2, pp. 198–204. ISSN: 2095-0055, 2192-6395. DOI: 10.1007/s13753-016-0086-5.
- McHugh, Marry L. (2012). “Interrater reliability: the kappa statistic.” In: *Biochemia Medica*, pp. 276–282. ISSN: 18467482. DOI: 10.11613/BM.2012.031.
- Met Office, National Meteorological Library and Archive (2005). *Fact sheet 3: Water in the Atmosphere*. Tech. rep. 3. https://www.metoffice.gov.uk/binaries/content/assets/metofficegovuk/pdf/research/library-and-archive/library/publications/factsheets/factsheet_3-water-in-the-atmosphere.pdf. Exeter: United Kingdom Meteorological Office.
- Miao, Yu, Yang Shi, and Su-Yang Wang (Dec. 2018). “Temporal change of near-surface shear wave velocity associated with rainfall in North-east Honshu, Japan.” In: *Earth, Planets and Space* 70.1. DOI: 10.1186/s40623-018-0969-3.
- Monjo, R (Feb. 2016). “Measure of rainfall time structure using the dimensionless n-index.” en. In: *Climate Research* 67.1, pp. 71–86. ISSN: 0936-577X, 1616-1572. DOI: 10.3354/cr01359.
- Montesarchio, V., F. Lombardo, and F. Napolitano (Feb. 2009). “Rainfall thresholds and flood warning: an operative case study.” en. In: *Natural Hazards and Earth System Sciences* 9.1, pp. 135–144. ISSN: 1684-9981. DOI: 10.5194/nhess-9-135-2009.
- Murphy, Kevin P. (2012). *Machine learning: a probabilistic perspective*. Adaptive computation and machine learning series. Cambridge, MA: MIT Press. 1067 pp. ISBN: 978-0-262-01802-9.

- Nashashibi, Fawzi, Raoul De Charette De La Contrie, and Alexandre Lia (Dec. 2010). "Detection of Unfocused Raindrops on a Windscreen using Low Level Image Processing." In: *International Conference on Control, Automation, Robotics and Vision: ICARV'2010*. Singapour, Singapour, P0655.
- Nayar, Shree K. and Kshitiz Garg (Oct. 2005). "When Does a Camera See Rain?" In: *Computer Vision, IEEE International Conference on (ICCV)*. Vol. 02, pp. 1067–1074. DOI: 10.1109/ICCV.2005.253.
- Notarangelo, Nicla M., Kohin Hirano, Aurelia Sole, and Raffaele Albano (June 2019a). "Enhancing flood risk management, through near real-time methods and technologies, for risk communication at local scale." NIED (National Research Institute for Earth Science and Disaster Resilience). Tuskuba, Japan.
- Notarangelo, Nicla M., Kohin Hirano, Aurelia Sole, and Raffaele Albano (May 2019b). "Rainfall detection in single images with Convolutional Neural Networks." 6th Weather Disaster Mitigation Innovation Forum "Disaster Prevention × AI" -Toward Meteorological Disaster Mitigation with AI. Innovation Center for Meteorological Disaster Mitigation. Tokyo, Japan.
- Notarangelo, Nicla M., Kohin Hirano, Aurelia Sole, and Raffaele Albano (2020). "Rilevamento delle precipitazioni piovose in immagini singole con reti neurali convoluzionali- Rainfall detection in single images through Convolutional Neural Networks." In: *Italian Conference on Integrated River Basin Management (ICIRBM-Guardia 2020)*. Vol. 41. Cosenza, Italy: EdiBios, pp. 69–82. ISBN: 978-88-97181-75-0.
- Notarangelo, Nicla Maria, Kohin Hirano, Raffaele Albano, and Aurelia Sole (Feb. 2021). *Transfer Learning with Convolutional Neural Networks for Rainfall Detection in Single Images*. DOI: 10.3390/w13050588.
- O'Sullivan, J. J., R. A. Bradford, M. Bonaiuto, S. De Dominicis, P. Rotko, J. Aaltonen, K. Waylen, and S. J. Langan (July 2012). "Enhancing flood resilience through improved risk communications." en. In: *Natural Hazards and Earth System Sciences* 12.7, pp. 2271–2282. ISSN: 1684-9981. DOI: 10.5194/nhess-12-2271-2012.
- Okamoto, K.i., T. Ushio, T. Iguchi, N. Takahashi, and K. Iwanami (2005). "The global satellite mapping of precipitation (GSMaP) project." In: *Proceedings. 2005 IEEE International Geoscience and Remote Sensing Symposium, 2005. IGARSS '05*. Vol. 5. Seoul, Korea: IEEE, pp. 3414–3416. ISBN: 978-0-7803-9050-8. DOI: 10.1109/IGARSS.2005.1526575.
- Okamoto, Kenichi, Nobuhiro Takahashi, Koyuru Iwanami, Shoichi Shige, and Takuji Kubota (Mar. 2008). "High precision and high resolution global precipitation map from satellite data." In: *2008 Microwave Radiometry and Remote Sensing of the Environment*. Florence, Italy: IEEE, pp. 1–4. ISBN: 978-1-4244-1986-9. DOI: 10.1109/MICRAD.2008.4579485.

- Orr, Paula, Steven Forrest, Katya Brooks, and Clare Twigger-Ross (2015). *Public dialogues on flood risk communication: Literature review: Literature review*. English. Environment Agency. ISBN: 978-1-84911-370-0.
- Palka, Gaëtan, Kamal Serrhini, Sven Fuchs, Serge Thibault, and Emmanuel Neron (Aug. 2013). "Improving Evacuation Maps by Integrating Needs and Preferences of End-Users in GIS." In: *26th International Cartographic Conference*. Dresden, Germany.
- Pan, S. J. and Q. Yang (Oct. 2010). "A Survey on Transfer Learning." In: *IEEE Transactions on Knowledge and Data Engineering* 22.10, pp. 1345–1359. ISSN: 1558-2191. DOI: 10.1109/TKDE.2009.191.
- Parajka, Juraj, Peter Haas, Robert Kirnbauer, Josef Jansa, and Günter Blöschl (Nov. 10, 2011). "Potential of time-lapse photography of snow for hydrological purposes at the small catchment scale." In: *Hydrological Processes* 26.22, pp. 3327–3337. DOI: 10.1002/hyp.8389.
- Parker, Dennis J., ed. (2000). *Floods*. eng. Routledge hazards and disasters series. London: Routledge. ISBN: 978-0-415-17238-7.
- Peel, M. C., B. L. Finlayson, and T. A. McMahon (2007). "Updated world map of the Köppen-Geiger climate classification." In: *Hydrology and Earth System Sciences* 11.5, pp. 1633–1644. DOI: 10.5194/hess-11-1633-2007.
- Pesaresi, Martino, Daniele Ehrlich, Thomas Kemper, Alice Siragusa, Aneta J Florczyk, Sérgio Freire, Christina Corbane, European Commission, and Joint Research Centre (2017). *Atlas of the human planet 2017: global exposure to natural hazards*.
- Peters, Richard G., Vincent T. Covello, and David B. McCallum (1997). "The Determinants of Trust and Credibility in Environmental Risk Communication: An Empirical Study." In: *Risk Analysis* 17.1, pp. 43–54. DOI: 10.1111/j.1539-6924.1997.tb00842.x.
- Piccardi, M. (2004). "Background subtraction techniques: a review." In: *2004 IEEE International Conference on Systems, Man and Cybernetics (IEEE Cat. No.04CH37583)*. The Hague, Netherlands: IEEE, pp. 3099–3104. ISBN: 978-0-7803-8567-2. DOI: 10.1109/ICSMC.2004.1400815.
- Pietroni, E. (2012). "An augmented experiences in cultural heritage through mobile devices: "Matera tales of a city" project." In: *2012 18th International Conference on Virtual Systems and Multimedia*, pp. 117–124. DOI: 10.1109/VSMM.2012.6365915.
- Pietroni, Eva, Stefano Borghini, Raffaele Carlani, and Claudio Rufa (2011). "Matera città narrata project: an integrated guide for mobile systems." In: *International Archives of the Photogrammetry, Remote Sensing and Spatial Information Sciences* 38.5/W16.
- Plate, Erich J (2002). "Flood risk and flood management." In: *Journal of Hydrology* 267.1-2, pp. 2–11.
- Poussin, Jennifer K., W.J. Wouter Botzen, and Jeroen C.J.H. Aerts (2014). "Factors of influence on flood damage mitigation behaviour by households." In: *Environmental Science & Policy* 40, pp. 69–77. ISSN: 1462-9011. DOI: 10.1016/j.envsci.2014.01.013.

- Protezione Civile Basilicata (n.d.). *Centro Funzionale Decentrato - CFD Basilicata*. <http://www.centrofunzionalebasilicata.it/it/>.
- Ratna Reddy, V. and Geoffrey J. Syme (2014). "Social sciences and hydrology: An introduction." In: *Journal of Hydrology* 518. Creating Partnerships Between Hydrology and Social Science: A Priority for Progress, pp. 1–4. ISSN: 0022-1694. DOI: 10.1016/j.jhydrol.2014.06.022.
- Razavian, Ali Sharif, Hossein Azizpour, Josephine Sullivan, and Stefan Carlsson (2014). *CNN Features off-the-shelf: an Astounding Baseline for Recognition*.
- Renn, Ortwin (1991). "Risk communication and the social amplification of risk." In: *Communicating Risks to the Public: International Perspectives*. Ed. by Roger E. Kasperson and Pieter Jan M. Stallen. Dordrecht: Springer Netherlands, pp. 287–324. ISBN: 978-94-009-1952-5. DOI: 10.1007/978-94-009-1952-5_14.
- Renn, Ortwin and Debra Levine (1991). "Credibility and trust in risk communication." In: *Communicating Risks to the Public: International Perspectives*. Ed. by Roger E. Kasperson and Pieter Jan M. Stallen. Dordrecht: Springer Netherlands, pp. 175–217. ISBN: 978-94-009-1952-5. DOI: 10.1007/978-94-009-1952-5_10.
- Ritchie, Hannah (2014). "Natural Disasters." In: *Our World in Data*. <https://ourworldindata.org/natural-disasters>.
- Riva Sanseverino, Eleonora, Raffaella Riva Sanseverino, Valentina Vaccaro, Ina Macaione, and Enrico Anello (2017). "Smart Cities: Case Studies." In: *Smart Cities Atlas: Western and Eastern Intelligent Communities*. Ed. by Eleonora Riva Sanseverino, Raffaella Riva Sanseverino, and Valentina Vaccaro. Cham: Springer International Publishing, pp. 47–140. ISBN: 978-3-319-47361-1. DOI: 10.1007/978-3-319-47361-1_3.
- Rollason, E, LJ Bracken, RJ Hardy, and ARG Large (2018). "Rethinking flood risk communication." In: *Natural Hazards*, pp. 1–22. DOI: 10.1007/s11069-018-3273-4.
- Roser, M. and A. Geiger (Sept. 2009). "Video-based raindrop detection for improved image registration." In: *2009 IEEE 12th International Conference on Computer Vision Workshops, ICCV Workshops*, pp. 570–577. DOI: 10.1109/ICCVW.2009.5457650.
- Rota, Lorenzo (2016). *Matera: the history of a town*. English. Matera: Giannatelli. ISBN: 978-88-97906-34-6.
- Russell, Stuart J., Peter Norvig, and Ernest Davis (2010). *Artificial intelligence: a modern approach*. 3rd ed. Prentice Hall series in artificial intelligence. Upper Saddle River: Prentice Hall. ISBN: 978-0-13-604259-4.
- Samuel, A. L. (July 1959). "Some Studies in Machine Learning Using the Game of Checkers." In: *IBM J. Res. Dev.* 3.3. Place: Riverton, NJ, USA, pp. 210–229. ISSN: 0018-8646. DOI: 10.1147/rd.33.0210.
- Scarpino, Santina, Raffaele Albano, Andrea Cantisani, Leonardo Mancusi, Aurelia Sole, and Giovanni Milillo (Mar. 2018). "Multitemporal

- SAR Data and 2D Hydrodynamic Model Flood Scenario Dynamics Assessment." en. In: *ISPRS International Journal of Geo-Information* 7.3, p. 105. ISSN: 2220-9964. DOI: 10.3390/ijgi7030105.
- Schaefer, Gerald and Michal Stich (2003). "UCID: an uncompressed color image database." In: *Storage and Retrieval Methods and Applications for Multimedia 2004*. Ed. by Minerva M. Yeung, Rainer W. Lienhart, and Chung-Sheng Li. Vol. 5307. International Society for Optics and Photonics. SPIE, pp. 472–480. DOI: 10.1117/12.525375.
- Schilling, Wolfgang (1991). "Rainfall data for urban hydrology: what do we need?" In: *Atmospheric Research* 27.1, pp. 5–21. ISSN: 0169-8095. DOI: 10.1016/0169-8095(91)90003-F.
- Selvaraju, Ramprasaath R., Abhishek Das, Ramakrishna Vedantam, Michael Cogswell, Devi Parikh, and Dhruv Batra (2016). "Grad-CAM: Why did you say that? Visual Explanations from Deep Networks via Gradient-based Localization." In: *CoRR* abs/1610.02391.
- Severtson, Dolores J. (2013). "The influence of environmental hazard maps on risk beliefs, emotion, and health-related behavioral intentions." In: *Research in Nursing & Health* 36.4, pp. 330–348. DOI: 10.1002/nur.21544.
- Shabman, Leonard, Paul Scodari, Douglas Woolley, and Carolyn Kousky (2014). "Vocabulary of Flood Risk Management Terms. Appendix A." In: *From Flood Damage Reduction to Flood Risk Management: Implications for USACE Policy and Programs*. USACE Institute for Water Resources.
- Shimazaki, Kan, Hiroko Nakajima, Naoki Sakai, and Akiko Miyajima (2018). "Gaps Between the Transmission and Reception of Information on Rainfall Amounts." In: *Journal of Disaster Research* 13.5, pp. 879–885. DOI: 10.20965/jdr.2018.p0879.
- Shorman, Samer and Sakinah Ali Pitchay (May 2016). "A Review of Rain Streaks Detection and Removal Techniques For Outdoor Single Image." In: *Journal of Engineering and Applied Sciences* 11.
- Shorten, Connor and Taghi M. Khoshgoftaar (Dec. 2019). "A survey on Image Data Augmentation for Deep Learning." en. In: *Journal of Big Data* 6.1, p. 60. ISSN: 2196-1115. DOI: 10.1186/s40537-019-0197-0.
- Sichenze, Armando (2014). *Dentro Matera - Into Matera*. Italian - English. Matera: Giannatelli. ISBN: 978-88-97906-28-5.
- Sichenze, Armando, ed. (2017). *Secret architecture - Architetture clandestine ; viaggi nelle 131 città-natura della Basilicata*. ita eng. Matera: Edizioni Giannatelli. ISBN: 978-88-97906-42-1.
- Simonyan, Karen and Andrew Zisserman (Sept. 4, 2014). "Very Deep Convolutional Networks for Large-Scale Image Recognition." In.
- Slovic, Paul (1999). "Trust, Emotion, Sex, Politics, and Science: Surveying the Risk-Assessment Battlefield." In: *Risk Analysis* 19.4, pp. 689–701. DOI: 10.1111/j.1539-6924.1999.tb00439.x.
- Soetanto, Robby, Aaron Mullins, and Nebil Achour (Apr. 2017). "The perceptions of social responsibility for community resilience to flood-

- ing: the impact of past experience, age, gender and ethnicity." en. In: *Natural Hazards* 86.3, pp. 1105–1126. ISSN: 0921-030X, 1573-0840. DOI: 10.1007/s11069-016-2732-z.
- Sole, A., L. Giosa, R. Albano, and A. Cantisani (May 2013). "The Laser Scan Data as a Key Element in the Hydraulic Flood Modelling in Urban Areas." en. In: *ISPRS - International Archives of the Photogrammetry, Remote Sensing and Spatial Information Sciences* XL-4/W1, pp. 65–70. ISSN: 1682-1777. DOI: 10.5194/isprsarchives-XL-4-W1-65-2013.
- Spilotro, Giuseppe, Ruggero Ermini, Ilenia Argentiero, Maria Fidelibus, Roberta Pellicani, and Alessandro Parisi (July 2019). "Le antiche culture dell'acqua." In: *Acqua e garden city*. Valenzano: CIHEAM Bari, pp. 132–152.
- Srinivas, Suraj, Ravi Kiran Sarvadevabhatla, Konda Reddy Mopuri, Nikita Prabhu, Srinivas S. S. Kruthiventi, and R. Venkatesh Babu (Jan. 2016). "A Taxonomy of Deep Convolutional Neural Nets for Computer Vision." In: *Frontiers in Robotics and AI* 2. Publisher: Frontiers Media SA. DOI: 10.3389/frobt.2015.00036.
- Srivastava, Nitish, Geoffrey Hinton, Alex Krizhevsky, Ilya Sutskever, and Ruslan Salakhutdinov (2014). "Dropout: a simple way to prevent neural networks from overfitting." In: *The journal of machine learning research* 15.1. Publisher: JMLR. org, pp. 1929–1958.
- Strangeways, Ian (2010). "A history of rain gauges." In: *Weather* 65.5, pp. 133–138. DOI: 10.1002/wea.548.
- Suzuki, Akihiro and Tomohito J. Yamada (2015). "Rainfall re-estimation associated with differences in the detection time of rainfall between X-band mp radar and raingauge." In: *Journal of Japan Society of Civil Engineers, Ser. G (Environmental Research)* 71.5. in Japanese, pp. I257–I262. DOI: 10.2208/jscej.71.1.257.
- Tauro, Flavia et al. (2018). "Measurements and Observations in the XXI century (MOXXI): innovation and multi-disciplinarity to sense the hydrological cycle." In: *Hydrological Sciences Journal* 63.2. Publisher: Taylor & Francis, pp. 169–196. DOI: 10.1080/02626667.2017.1420191.
- Thistlethwaite, Jason, Daniel Henstra, Craig Brown, and Daniel Scott (Feb. 2018). "How Flood Experience and Risk Perception Influences Protective Actions and Behaviours among Canadian Homeowners." en. In: *Environmental Management* 61.2, pp. 197–208. ISSN: 0364-152X, 1432-1009. DOI: 10.1007/s00267-017-0969-2.
- Tieleman, Tijmen and Geoffrey Hinton (2012). "Lecture 6.5 rmsprop: Divide the gradient by a running average of its recent magnitude." In: *COURSERA: Neural networks for machine learning* 4.2, pp. 26–31.
- Toxey, Anne Parmly (2009). "Recasting Materan Identity: The waring and melding of political ideologies carved in stone." In: *The Mediterranean Medina*. Ed. by Ludovico Micara, Attilio Petruccioli, and Ettore Vadini. Roma: Gangemi Editore, pp. 541–550. ISBN: 978-88-492-1605-9.

- Tripathi, Abhishek Kumar and Sudipta Mukhopadhyay (Nov. 2014). "Removal of rain from videos: a review." en. In: *Signal, Image and Video Processing* 8.8, pp. 1421–1430. ISSN: 1863-1703, 1863-1711. DOI: 10.1007/s11760-012-0373-6.
- Tucker, W Troy, Scott Ferson, ADAM M FINKEL, and DAVID SLAVIN (2008). "Strategies for risk communication." In: *Annals of the New York Academy of Sciences* 1128.1, p. ix.
- UNISDR, ed. (2015). *Making development sustainable: the future of disaster risk management*. eng. Global assessment report on disaster risk reduction 4.2015. Geneva: United Nations Office for Disaster Risk Reduction (UNISDR). ISBN: 978-92-1-132042-8.
- United Nations General Assembly (Dec. 2016). "Report of the Open-ended Intergovernmental Expert Working Group on Indicators and Terminology relating to Disaster Risk Reduction." In: 41 p.
- United Nations Office for Disaster Risk Reduction (UNDRR) (2006). *ISDR: Platform for the Promotion of Early Warning*. <https://www.unisdr.org/2006/ppew/>.
- Versace, Pasquale (Mar. 2017). "Scenari di evento e di rischio idraulico e idrogeologico." Unesco Chair Geo-hydrological hazards Florence University. Florence, Italy.
- Viglione, Alberto, Giuliano Di Baldassarre, Luigia Brandimarte, Linda Kuil, Gemma Carr, José Luis Salinas, Anna Scolobig, and Günter Blöschl (2014). "Insights from socio-hydrology modelling on dealing with flood risk – Roles of collective memory, risk-taking attitude and trust." In: *Journal of Hydrology* 518. Creating Partnerships Between Hydrology and Social Science: A Priority for Progress, pp. 71–82. ISSN: 0022-1694. DOI: 10.1016/j.jhydro.2014.01.018.
- Visschers, Vivianne H. M., Ree M. Meertens, Wim W. F. Passchier, and Nanne N. K. de Vries (Feb. 2009). "Probability Information in Risk Communication: A Review of the Research Literature." en. In: *Risk Analysis* 29.2, pp. 267–287. ISSN: 02724332, 15396924. DOI: 10.1111/j.1539-6924.2008.01137.x.
- Weiss, Karl, Taghi M. Khoshgoftaar, and DingDing Wang (Dec. 2016). "A survey of transfer learning." en. In: *Journal of Big Data* 3.1, p. 9. ISSN: 2196-1115. DOI: 10.1186/s40537-016-0043-6.
- World Meteorological Organization (2014). "Observation of present and past weather; state of the ground." In: *Guide to meteorological instruments and methods of observation*. Geneva, Switzerland: World Meteorological Organization. ISBN: 978-92-63-10008-5.
- Xiang, Wei, Kan Zheng, and Xuemin Shen, eds. (2017). *5G Mobile Communications*. en. Cham: Springer International Publishing. ISBN: 978-3-319-34206-1 978-3-319-34208-5. DOI: 10.1007/978-3-319-34208-5.
- Xu, Xiangzhou, Tongxin Zhu, Hongwu Zhang, and Lu Gao (2020). "A Conventional Experimental Technique: Rainfall Simulation." In: *Experimental Erosion: Theory and Practice of Soil Conservation Experiments*.

- Singapore: Springer Singapore, pp. 29–43. ISBN: 978-981-15-3801-8. DOI: 10.1007/978-981-15-3801-8_3.
- Yamada, Fumihiko, Ryuji Kakimoto, Miyuki Yamamoto, Toshio Fujimi, and Naoto Tanaka (2011). “Implementation of community flood risk communication in Kumamoto, Japan.” In: *Journal of Advanced Transportation* 45.2, pp. 117–128. DOI: 10.1002/atr.119.
- Yan, Xunshi, Yupin Luo, and Xiaoming Zheng (2009). “Weather Recognition Based on Images Captured by Vision System in Vehicle.” In: *Advances in Neural Networks – ISNN 2009*. Ed. by Wen Yu, Haibo He, and Nian Zhang. Berlin, Heidelberg: Springer Berlin Heidelberg, pp. 390–398. ISBN: 978-3-642-01513-7.
- Yang, Wenhan, Robby T. Tan, Jiashi Feng, Jiaying Liu, Zongming Guo, and Shuicheng Yan (2016). “Joint Rain Detection and Removal via Iterative Region Dependent Multi-Task Learning.” In: *CoRR* abs/1609.07769.
- Yosinski, Jason, Jeff Clune, Yoshua Bengio, and Hod Lipson (2014). “How transferable are features in deep neural networks?” In: *CoRR* abs/1411.1792.
- Zhang, Zheng, Huadong Ma, Huiyuan Fu, and Cheng Zhang (Sept. 2016). “Scene-free multi-class weather classification on single images.” In: *Neurocomputing* 207. Publisher: Elsevier BV, pp. 365–373. DOI: 10.1016/j.neucom.2016.05.015.
- Zheng, Alice (2015). *Evaluating Machine Learning Models*. O’Reilly Media, Inc. ISBN: 978-1-4920-4875-6.